

A dissertation entitled

Observation of W^+W^- Production
in $\bar{p}p$ Collisions at $\sqrt{s} = 1.8$ TeV

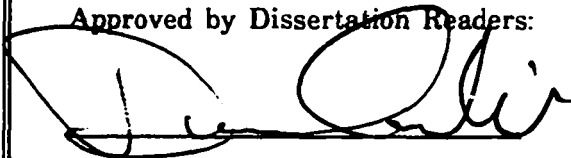
submitted to the Graduate School of the
University of Wisconsin-Madison
in partial fulfillment of the requirements for the
degree of Doctor of Philosophy

by

Liqun Zhang

Degree to be awarded: December 1997 May 19 August 19

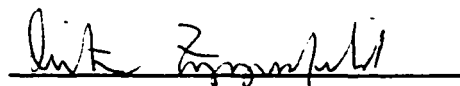
Approved by Dissertation Readers:



Major Professor

May 1, 1996

Date of Examination



Dean, Graduate School

Observation of W^+W^- Production
in $\bar{p}p$ Collisions at $\sqrt{s} = 1.8$ TeV

by

Liqun Zhang

A dissertation submitted in partial fulfillment of the
requirements for the degree of

Doctor of Philosophy

(Physics)

at the

UNIVERSITY OF WISCONSIN - MADISON

1997

Abstract

A search for W^+W^- production in $\bar{p}p$ collisions at $\sqrt{s} = 1.8$ TeV is presented. In a data sample of 108 pb^{-1} recorded with the Collider Detector at Fermilab (CDF), five W^+W^- candidates are observed in the dilepton channel $W^+W^- \rightarrow l^+l^-\nu\bar{\nu}$. We expect 3.53 ± 1.24 events from the electroweak W^+W^- production and 1.21 ± 0.30 events from various backgrounds. The W^+W^- production cross section is found to be $\sigma(\bar{p}p \rightarrow W^+W^-) = 10.2_{-5.1}^{+6.3}(\text{stat}) \pm 1.6(\text{syst}) \text{ pb}$. Then limits on boson anomalous couplings are set at 95% confidence level.

Acknowledgements

I am indebted to my advisor, Professor Duncan Carlsmith, who foresaw the feasibility of diboson search years ago, and constantly gave me technical help and moral encouragement.

I am grateful to the people in the FMU group: Lee Pondrom and Chris Wendt, for their valuable help and advice. I also thank Jim Bellinger, Robert Handler, Sergei Lusin, and George Ott, for their technical assistance.

In addition, I thank members of the CDF collaboration, especially Doug Benjaming, Milciades Contreras, Young-kee Kim, Jaco Konigsberg, Jodi Lamoureux, Larry Nudolman, Andra Parri, and G.P. Yeh for their collective support and vital contributions to this analysis.

Finally, my deepest thanks go to my parents for their support and love over the years.

This work was supported by the United States Department of Energy Contract DE-AC02-76ER00881.

Contents

Abstract	i
Acknowledgements	ii
List of Tables	vii
List of Figures	x
1 Theory of W^+W^- Production	1
1.1 Introduction	1
1.2 Standard Model Results	3
1.2.1 Formalism	3
1.2.2 LO Calculations	5
1.2.3 NLO Calculations	7
1.2.4 Spin Correlation	9
1.3 Phenomenology of Anomalous Couplings	10
1.3.1 Formalism	10

1.3.2	Scenarios	12
1.3.3	Limits from Precision Measurements	12
2	Apparatus	15
2.1	Tevatron	15
2.2	CDF Detector	17
2.2.1	Luminosity	19
2.2.2	Tracking	20
2.2.3	Calorimeters	21
2.2.4	Central Muon Chambers	23
2.2.5	Forward Muon Detector	24
2.2.5.1	Toroids	24
2.2.5.2	Chambers	26
2.2.5.3	Scintillator Counters	28
2.2.5.4	Triggers	31
2.2.5.5	Momentum Resolution	32
2.3	CDF Upgrade	34
3	Data Selection	39
3.1	Central Electrons	40
3.1.1	Triggers	40
3.1.2	Selection Cuts	41
3.2	Plug Electrons	45

3.2.1	Triggers	45
3.2.2	Selection Cuts	46
3.3	Central Muons	49
3.3.1	Triggers	49
3.3.2	Selection Cuts	49
3.4	Forward Muons	54
3.4.1	Triggers	54
3.4.2	Selection Cuts	54
3.5	Jets	57
3.5.1	Triggers	57
3.5.2	Selection Cuts	58
3.5.3	Energy Uncertainty	62
3.6	Missing Transverse Energy	63
4	Acceptance and Background	66
4.1	Acceptance	66
4.1.1	Dilepton Classification	67
4.1.2	Detection Efficiency	67
4.1.3	Uncertainties	81
4.2	Background	86
4.2.1	$t\bar{t}$	86
4.2.2	$Z \rightarrow \tau\tau$	87

4.2.3	Drell-Yan	89
4.2.4	Fake Leptons	92
4.2.5	WZ	96
4.2.6	$b\bar{b}$	97
4.2.7	Summary	98
5	Results	99
5.1	Data Overview	99
5.2	W^+W^- Cross Section	100
5.2.1	Measurement	100
5.2.2	Upper Limit	122
5.3	WWV Anomalous Couplings	125
5.3.1	Parameters	125
5.3.2	Upper Limits	125
5.3.3	Limits from other experiments	129
5.4	Summary	132
A	Anomalous Couplings	136
B	Measurement of Magnetic Field	139
	Bibliography	147

List of Tables

1.1	Asymptotic forms of $\sigma_{ij}(e^+e^- \rightarrow W^+W^-)$. The subscripts indicate exchange particles.	6
3.1	Central electron selection cuts.	43
3.2	Plug electron selection cuts.	48
3.3	Central muon selection cuts.	51
3.4	Forward muon selection cuts.	57
4.1	Dilepton Classification. CEM and PEM denote the electromagnetic calorimeters in the central and plug regions, respectively. CMU, CMP and CMX are labeled with CMUO, while CMIO refers to a minimum ionizing track. FMU stands for the forward muon chambers.	68
4.2	Single-lepton identification efficiencies.	71
4.3	Jet multiplicity of W^+W^- production from various W^+W^- Monte Carlo simulations.	79

4.4	Jet multiplicity of W^+W^- and Z ($M_Z = 240 \text{ GeV}/c^2$) productions from ISAJET Monte Carlo simulations. Note that QTW = 0 (default) is used for ISAJET generator. Here α_n is obtained by taking the ratio of $\epsilon_{n-jet}(WW)$ to $\epsilon_{n-jet}(2.7M_Z)$	81
4.5	Jet multiplicity of Z production from ISAJET and VECBOS Monte Carlo simulations. Here β_n is obtained by taking the ratio of $\epsilon_{n-jet}(2.7M_Z)$ to $\epsilon_{n-jet}(M_Z)$. Note that QTW = 0 (default) is used in ISAJET simulations for β_n , while β_n^* is obtained with QTW \neq 0. See text for these options.	82
4.6	Jet multiplicity of W^+W^- production. See text for detail.	82
4.7	Dilepton detection efficiency.	85
4.8	Total dilepton detection efficiency.	85
4.9	Lepton selection variables that are used to separate leptons from jets. Their definitions are given in Chapter 3.	95
4.10	Fake rates derived from jet data samples.	97
4.11	Backgrounds to W^+W^- in the 108 pb^{-1} data sample.	98
5.1	Summary of dilepton events in the 108 pb^{-1} data.	100
5.2	W^+W^- candidates in the 108 pb^{-1} data.	117
5.3	Upper limits on anomalous couplings at 95 % CL for two different energy scales. The vertices $WW\gamma$ and WWZ are assumed to have the same couplings constants.	129

5.4	Projected 95 % CL upper limits on anomalous WWV ($V = \gamma$, Z) couplings in the HISZ scenario. Only one of the independent couplings is assumed to deviate from the SM at a time.	134
-----	--	-----

List of Figures

1.1	The tree-level Feynman diagrams for W^+W^- production in $\bar{p}p$ collisions.	4
1.2	$WW\gamma$ and WWZ vertices. The coupling constants g_{WWV} ($V = \gamma, Z$) are given in the text.	4
1.3	Feynman diagrams for W^+W^- production in e^+e^- collisions. (a) and (b) are the s channel, u and t channels, respectively.	7
1.4	The W polarization vector e^μ is replaced by the decay current j^μ for a full matrix element calculation.	8
1.5	Feynman diagram for $b \rightarrow s\gamma$ decay. The decay rate depends on $WW\gamma$ couplings.	13
2.1	Overview of the Fermilab accelerator complex.	16
2.2	A quarter of the CDF detector. The detector is symmetric about the z axis and x-y plane.	18
2.3	A side-view cross section of the FMU detector.	25
2.4	Schematic of the FMU chamber.	27

2.5	Scintillator counter noise rate. Wedges are divided into the west front (WF), west rear (WR), east front (EF), and east rear (ER) planes. Each plane has 72 wedges.	29
2.6	Scintillator noise rate evolution with time.	30
2.7	FMU events detected by the SINPAD trigger board. The dotted histogram indicates the number of events that should be triggered, while the solid histogram shows the actual triggered events.	33
2.8	Proposed CDF detector for Run II.	36
3.1	Pseudorapidity distribution and quality variables of central electrons. (a) pseudorapidity, (b) lateral shower profile variable, (c) ratio of hadronic and electromagnetic energy, and (d) calorimeter isolation variable. Arrows denote the values of the selection cuts.	44
3.2	Pseudorapidity distribution and quality variables of plug electrons. (a) pseudorapidity, (b) χ^2 for the electron hypothesis from the shape of the shower in the transverse direction, (c) χ^2 for the electron hypothesis from the shape of the shower in the longitudinal direction, and (d) calorimeter isolation variable. Arrows denote the cutoffs used in the plug electron selection.	47

3.3	Pseudorapidity distribution and quality variables of central muons. (a) pseudorapidity, (b) energy deposited in the electromagnetic calorimeter, (c) energy deposited in the hadronic calorimeter, and (d) distance between the muon track and beam line. Also shown are cutoffs used in the central muon selection.	52
3.4	Pseudorapidity distribution and quality variables of forward muons. (a) pseudorapidity, (b) energy deposited in the electromagnetic calorimeter, (c) energy deposited in the hadronic calorimeter, and (d) interaction vertex. Also shown are cutoffs used in the forward muon selection.	56
3.5	The central calorimeter response (E/p) to pions with momentum p .	59
3.6	Total uncertainty (T) in the jet energy scale as a function of corrected jet E_T . The sources of uncertainty are the calorimeter response (C), fragmentation (F), and underlying event (U).	60
3.7	Unbalanced E_T in photon+jet events: data and PAPAGENO+QFL simulations.	61
3.8	\cancel{E}_T distribution in $W^+W^- \rightarrow l^+l^-\nu\bar{\nu}$ from ISAJET simulations. .	65
4.1	Pseudorapidity η and transverse energy E_T (momentum P_T) distributions from $W^+W^- \rightarrow e\mu$ simulations: (a) and (b) for electrons; (c) and (d) for muons.	70

4.2	Electron isolation distributions from W^+W^- simulations: calorimeter isolation (a) and track isolation (b) for central electrons; calorimeter isolation (c) and track isolation (d) for plug electrons.	73
4.3	Muon isolation distributions from W^+W^- simulations: calorimeter isolation (a) and track isolation (b) for central muons; calorimeter isolation (c) and track isolation (d) for minimum ionizing tracks.	74
4.4	W^+W^- invariant mass from $\bar{p}p \rightarrow W^+W^-$ simulations (ISAJET).	83
4.5	W^+W^- invariant mass from $\bar{p}p \rightarrow W^+W^-$ simulations (PYTHIA).	84
4.6	Jet multiplicity in $t\bar{t} \rightarrow W^+W^-b\bar{b}$ from ISAJET and PYTHIA simulations. The top quark mass is taken as $170 \text{ GeV}/c^2$. See text for W^+W^- jet multiplicity.	88
4.7	Distribution of the azimuthal angle between \cancel{E}_T and the closest lepton vs \cancel{E}_T , from $Z \rightarrow \tau\tau$ simulations. Leptons from $Z \rightarrow ee(\mu\mu)$ data samples are replaced with τ 's which are then forced to decay into electrons or muons.	90
4.8	Distribution of the azimuthal angle between \cancel{E}_T and the closest lepton vs \cancel{E}_T , from ISAJET $Z \rightarrow \tau\tau$ simulations.	91
4.9	Distributions of the invariant mass and azimuthal angle between \cancel{E}_T and the closest lepton in $Z \rightarrow e^+e^-$. (a) and (b) are distributions before the jet veto, while (c) and (d) are after the cut.	93

4.10	Distributions of the invariant mass and azimuthal angle between \cancel{E}_T and the closest lepton in $Z \rightarrow \mu^+ \mu^-$. (a) and (b) are distributions before the jet veto, while (c) and (d) are after the cut. . . .	94
5.1	Distributions of the azimuthal angle between \cancel{E}_T and the closest lepton vs \cancel{E}_T in the ee channel. (a) Events without jets, (b) events with one jet, (c) events with two or more jets, and (d) all events. 1A data only.	101
5.2	Distributions of the azimuthal angle between \cancel{E}_T and the closest lepton vs \cancel{E}_T in the ee channel. (a) Events without jets, (b) events with one jet, (c) events with two or more jets, and (d) all events. 1B data only.	102
5.3	Distributions of the azimuthal angle between \cancel{E}_T and the closest lepton vs \cancel{E}_T in the $e\mu$ channel. (a) Events without jets, (b) events with one jet, (c) events with two or more jets, and (d) all events. 1A data only.	103
5.4	Distributions of the azimuthal angle between \cancel{E}_T and the closest lepton vs \cancel{E}_T in the $e\mu$ channel. (a) Events without jets, (b) events with one jet, (c) events with two or more jets, and (d) all events. 1B data only.	104

5.5	Distributions of the azimuthal angle between \cancel{E}_T and the closest lepton vs \cancel{E}_T in the $\mu\mu$ channel. (a) Events without jets, (b) events with one jet, (c) events with two or more jets, and (d) all events. 1A data only.	105
5.6	Distributions of the azimuthal angle between \cancel{E}_T and the closest lepton vs \cancel{E}_T in the $\mu\mu$ channel. (a) Events without jets, (b) events with one jet, (c) events with two or more jets, and (d) all events. 1B data only.	106
5.7	Distribution of the ee invariant mass, just after the lepton selection and isolation cuts. 1A data only.	107
5.8	Distribution of the ee invariant mass, just after the lepton selection and isolation cuts. 1B data only.	108
5.9	Distribution of the $\mu\mu$ invariant mass, just after the lepton selection and isolation cuts. 1A data only.	109
5.10	Distribution of the $\mu\mu$ invariant mass, just after the lepton selection and isolation cuts. 1B data only.	110
5.11	Event display for one of the W^+W^- candidates: calorimeter E_T in the η - ϕ plane (top); reconstructed CTC tracks and muon hits in the r - ϕ plane (bottom). Note that the muon only leaves a minimum ionizing energy in the calorimeters.	112

5.12	Event display for one of the W^+W^- candidates: calorimeter E_T in the η - ϕ plane (top); reconstructed CTC tracks and muon hits in the r - ϕ plane (bottom).	113
5.13	Event display for one of the W^+W^- candidates: calorimeter E_T in the η - ϕ plane (top); reconstructed CTC tracks and muon hits in the r - ϕ plane (bottom).	114
5.14	Event display for one of the W^+W^- candidates: calorimeter E_T in the η - ϕ plane (top); reconstructed CTC tracks and muon hits in the r - ϕ plane (bottom).	115
5.15	Event display for one of the W^+W^- candidates: calorimeter E_T in the η - ϕ plane (top); reconstructed CTC tracks and muon hits in the r - ϕ plane (bottom).	116
5.16	Azimuthal angle between the \cancel{E}_T direction and the closest lepton, versus \cancel{E}_T , from W^+W^- simulations.	119
5.17	Azimuthal angle between the \cancel{E}_T direction and the closest lepton, versus \cancel{E}_T , for W^+W^- candidates.	120
5.18	The \cancel{E}_T distribution for W^+W^- candidates. The dotted histogram is the background to W^+W^- . The total number of events (solid histogram) is normalized to the observed number of events.	121

5.19	The W^+W^- production cross section $\sigma(\bar{p}p \rightarrow W^+W^-)$ measured at the CDF, compared to theoretical calculations. The theoretical results are based on the next-to-leading order (NLO) calculation, and the leading order (LO) calculation (solid line). See text for detail.	123
5.20	Upper limits on anomalous couplings $\Delta\kappa$ and λ , assuming $\kappa_\gamma=\kappa_Z=\kappa$ and $\lambda_\gamma=\lambda_Z=\lambda$. Here $\Delta\kappa=\kappa - 1$. The SM value is located at the center. The outer (inner) contour is 95 % CL upper limits with the energy scale $\Lambda = 1$ TeV (2 TeV).	127
5.21	Upper limits on anomalous couplings $\Delta\kappa_\gamma$ and λ_γ in the HISZ scenario. The SM value is located at the center. The outer (inner) contour is 95 % CL upper limits with the energy scale $\Lambda = 1$ TeV (2 TeV).	128
5.22	Present upper limits on anomalous couplings from $W\gamma$ and $WW/WZ \rightarrow l\nu jj$ productions.	133
B.1	Loop and integrator circuit. The loop is constructed from steel wires. Electric charges eventually reach the capacitor where they accumulate.	141

- B.2 Hall probe and feedback amplifier circuit. The output of the Hall element is determined by the control current I_C and the strength of magnetic field. The gain of the circuit is determined by the ratio of resistors. 142
- B.3 Magnetic field integral for the east rear toroid with a current of 1,000 Amps. R is the distance from the beampipe in $r-\phi$. The two dips are caused by the non-uniform field near seams. 143
- B.4 Magnetic field integral for the east and west rear toroids with a current of 600 Amps. 144
- B.5 West rear field profile along the z direction at a fixed distance (214 cm) from the beampipe, with a current of 600 Amps. The toroid starts at $z = 0.0$ cm and ends at $z = 100.0$ cm. 145

Chapter 1

Theory of W^+W^- Production

1.1 Introduction

The standard model (SM) has been remarkably successful in describing strong and electroweak interactions in particle physics. Analyses of high energy physics experimental results around the world have been indicating that they agree well with the SM predictions. However, one sector of the SM—trilinear vector boson couplings—remains essentially untested. The gauge structure of the $SU(2) \times SU(1)$ theory of electroweak interactions governs vector boson couplings and leads to a cancellation of helicity amplitudes, thus preserving the unitarity of the theory. One way to probe boson couplings is to search for diboson production, which directly results from these couplings. In the last two decades, some theoretical calculations and very preliminary experimental measurements have

been published in this field. As a whole, however, vector boson couplings are still poorly understood. The reason is quite simple: Diboson production cross sections are very small. Therefore, even at the Tevatron, the most powerful accelerator in the world, we only expect to observe very few diboson events.

Besides testing the gauge structure of the SM, diboson searches also provide an opportunity to probe new physics. Some unorthodox theoretical models propose new mechanisms that may result in an enhanced diboson production cross section. If, for instance, vector bosons W and Z are composite particles, vector boson self-interactions will exhibit anomalous couplings[1]. New particles, such as Higgs bosons, heavy quarks and leptons, and technihadrons[2, 3], tend to decay into boson pairs. So a discrepancy between the SM prediction and experimental observations in the diboson production might be an indication of new physics beyond the SM.

In this analysis, I concentrate on search for W^+W^- production through the dilepton channel $W^+W^- \rightarrow l^+l^-\nu\bar{\nu}$ ($l = e, \mu$), largely because it has never been done before and its background is small. The contribution from $W^+W^- \rightarrow l\tau$ or $\tau\tau$, followed by $\tau \rightarrow e$ or μ , is also included. The W^+W^- production cross section, in the framework of the SM, is about 10 pb[4, 5], while other non-standard models usually predict a larger one[1, 2, 3]. So far the Collider Detector at Fermilab (CDF) has recorded over 100 pb^{-1} of $\bar{p}p$ collisions since 1992. This makes a W^+W^- search possible for the first time in history. The following section describes various calculations of the W^+W^- production cross section. The final

section is devoted to $WW\gamma$ and WWZ anomalous couplings, which give a different picture of W^+W^- production.

1.2 Standard Model Results

1.2.1 Formalism

The Feynman diagrams for W^+W^- production in $\bar{p}p$ collisions are shown in Figure 1.1. One can easily find the relevant Feynman rules in the literature. The interesting part of the interaction vertices is WWV ($V = \gamma, Z$) couplings since $Wf\bar{f}$ vertices are well understood.

The SM prescription of WWV couplings is based on the $SU(2) \times SU(1)$ gauge theory of electroweak interactions. The relevant interaction Lagrangian has the form

$$\mathcal{L}_{WWV} = g_{WWV}(W_{\mu\nu}^+W^\mu V^\nu - W_\mu^+V_\nu W^{\mu\nu} + W_\mu^+W_\nu V^{\mu\nu}), \quad (1.1)$$

with $g_{WW\gamma} = e$ for the $WW\gamma$ vertex and $g_{WWZ} = e\cot\theta_W$ for the WWZ vertex, where e is the proton electric charge and θ_W is the mixing angle. Here W^μ is the W^- field, V^ν denotes the Z boson or photon field, with $W_{\mu\nu} = \partial_\mu W_\nu - \partial_\nu W_\mu$ and $V_{\mu\nu} = \partial_\mu V_\nu - \partial_\nu V_\mu$. The Feynman rules for this Lagrangian are given in Figure 1.2.

Starting with these Feynman rules, one can easily calculate the differential cross section $\hat{\sigma}(q\bar{q} \rightarrow W^+W^-)$ in terms of the Mandelstam variables \hat{s} , \hat{u} and

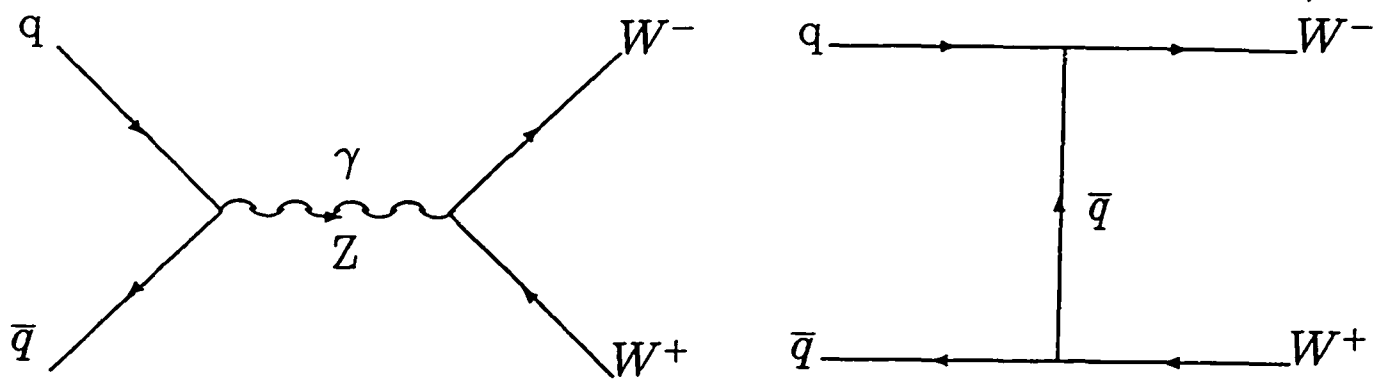
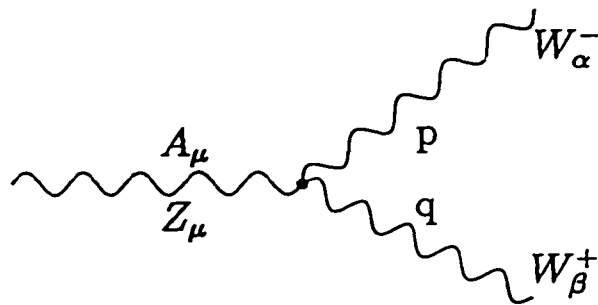


Figure 1.1: The tree-level Feynman diagrams for W^+W^- production in $\bar{p}p$ collisions.



$$\Gamma_{WWV} = g_{WWV} [g_{\beta\alpha}(p - q)_\mu + q_\alpha g_{\mu\beta} - p_\beta g_{\mu\alpha} + g_{\beta\mu}(p + q)_\alpha - g_{\alpha\mu}(p + q)_\beta]$$

Figure 1.2: $WW\gamma$ and WWZ vertices. The coupling constants g_{WWV} ($V = \gamma, Z$) are given in the text.

\hat{t} . Then the W^+W^- production cross section $\sigma(\bar{p}p \rightarrow W^+W^-)$ is obtained by convoluting $\hat{\sigma}(q\bar{q} \rightarrow W^+W^-)$ with the parton distribution functions $f(x)$

$$\sigma(\bar{p}p \rightarrow W^+W^-) = \sum_{q\bar{q}} \int \int dx_1 dx_2 f_q(x_1) f_{\bar{q}}(x_2) \hat{\sigma}(q\bar{q} \rightarrow W^+W^-), \quad (1.2)$$

where x is the fraction of proton or antiproton momentum carried by a quark. The sum is over all quark flavors.

1.2.2 LO Calculations

With the method described above, the leading order (LO) calculation of the W^+W^- production cross section is straightforward but tedious. The amplitude expression is too long to be cited here. The final result is[5]

$$\sigma(\bar{p}p \rightarrow W^+W^-) = 7.4 \text{ pb.}$$

Here the HMRS set B parton distribution function is used[6]. By comparison, the EHLQ set I distribution function with $Q^2 = \hat{s}$ [3] yields[4]

$$\sigma(\bar{p}p \rightarrow W^+W^-) = 6.7 \text{ pb.}$$

QCD corrections are omitted in these calculations.

As indicated earlier, W^+W^- production amplitudes cancel each other. As a result, the unitarity of the theory is preserved. To illustrate this unique feature of the gauge theory, let's take a look at a simple example: $e^+e^- \rightarrow W^+W^-$ [7]. There are three channels in this case: s channel with virtual photon and Z boson

$\sigma_{ZZ} \sim \frac{S}{M_W^4}$	$\sigma_{\gamma\gamma} \sim \frac{S}{M_W^4}$	$\sigma_{\nu\nu} \sim \frac{S}{M_W^4}$
$\sigma_{Z\gamma} \sim \frac{S}{M_W^4}$	$\sigma_{Z\nu} \sim -\frac{S}{M_W^4}$	$\sigma_{\gamma\nu} \sim -\frac{S}{M_W^4}$

Table 1.1: Asymptotic forms of $\sigma_{ij}(e^+e^- \rightarrow W^+W^-)$. The subscripts indicate exchange particles.

production, and u and t channel with neutrino exchange (see Figure 1.3). The total cross section can be decomposed as

$$\sigma(e^+e^- \rightarrow W^+W^-) = \sum_{ij} \sigma_{ij}, \quad (1.3)$$

where $i, j = \nu, \gamma, \text{ and } Z$. The notation is as follows: σ_{ZZ} is the Z exchange contribution; $\sigma_{\gamma\gamma}$ is from the γ exchange; $\sigma_{\nu\nu}$ is from the ν exchange; $\sigma_{Z\gamma}$, $\sigma_{Z\nu}$, and $\sigma_{\gamma\nu}$ are the interference terms. They can be expanded in terms of the e^+e^- center-of-mass energy \sqrt{S} . The leading order terms are listed in Table 1.1. The next-to-leading order terms are of the form of

$$\frac{1}{S} \ln \frac{S}{M_w^2}.$$

One notices that they are all divergent at high energy. Since the unitarity of field theories requires that any production cross section be finite, one concludes that there must be a cancellation between these terms in order to preserve the unitarity. That is exactly what would happen if all the terms are combined for high S

$$\sigma(e^+e^- \rightarrow W^+W^-) \sim \frac{1}{S} \ln \frac{S}{M_w^2} \rightarrow 0. \quad (1.4)$$

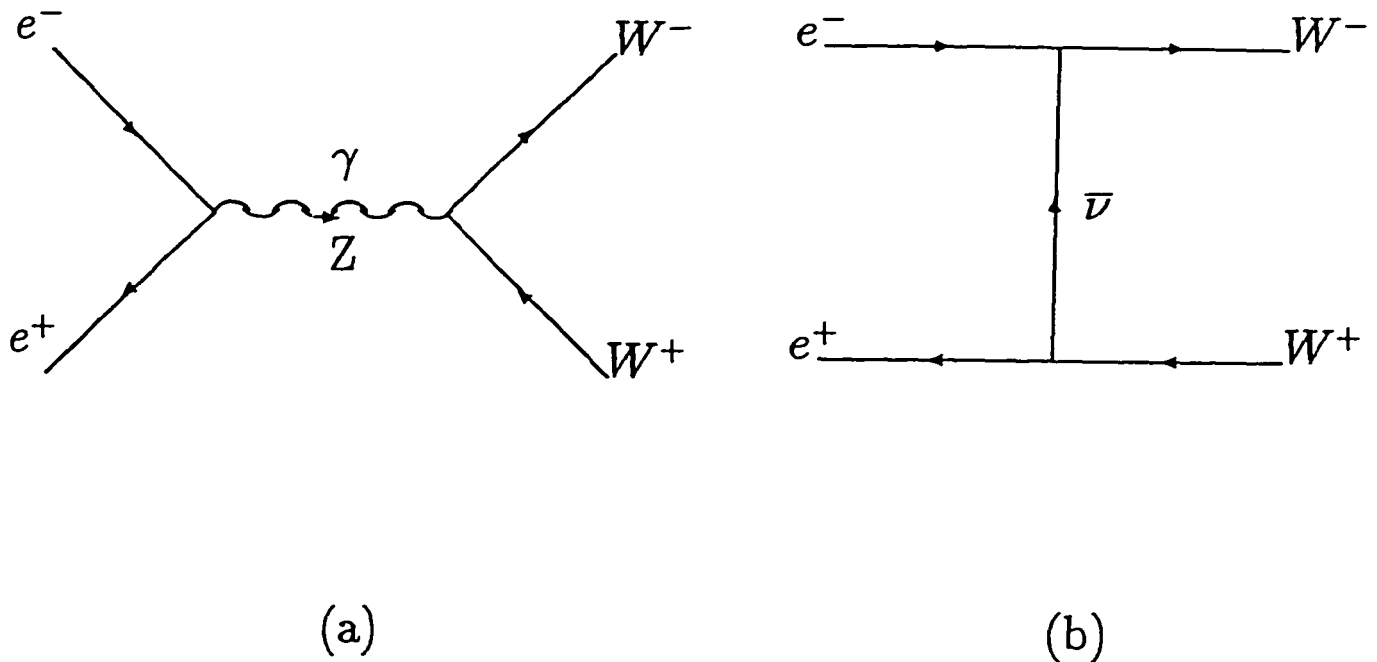


Figure 1.3: Feynman diagrams for W^+W^- production in e^+e^- collisions. (a) and (b) are the s channel, u and t channels, respectively.

The leading order terms cancel each other and only the next-to-leading order terms survive. This example perfectly illustrates the delicate gauge structure of the SM.

1.2.3 NLO Calculations

All the calculations mentioned so far are up to the LO of QCD—jets from gluons and quarks are ignored. Ohnemus recently published a next-to-leading order (NLO) calculation of $\sigma(\bar{p}p \rightarrow W^+W^-)$. He found[5]

$$\sigma(\bar{p}p \rightarrow W^+W^-) = 9.5 \text{ pb},$$

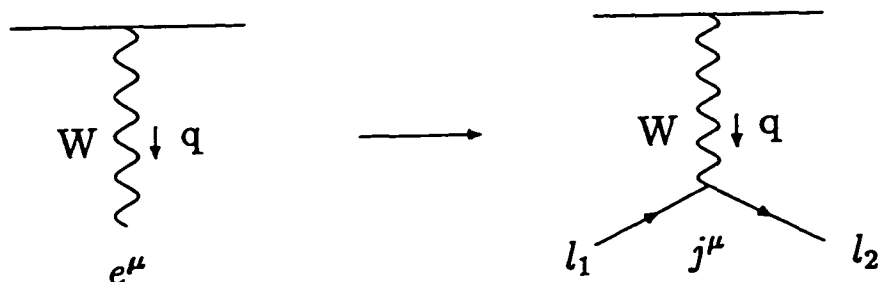


Figure 1.4: The W polarization vector e^μ is replaced by the decay current j^μ for a full matrix element calculation.

which includes contributions from the square of the Born diagrams, the interference between the Born diagrams and the virtual one-loop diagrams, and the square of the real gluon emission diagrams. Essentially this is the cross section up to one QCD jet. Again the HMRS set B parton distribution function is used. The change of $\sigma(\bar{p}p \rightarrow W^+W^-)$ is less than 5 % for different distribution functions.

Barger et al. also calculated the W^+W^- production cross section up to two jets at tree level[4], with the choice of the EHLQ distribution function. The cross section is given by

$$\sum_{jets=0}^2 \sigma(\bar{p}p \rightarrow W^+W^- + jets) = 9.6 \text{ pb.} \quad (1.5)$$

Jets are required to have a transverse momentum $P_T > 15 \text{ GeV}/c$, which is close to the definition of jets in this analysis. However, the contribution from loop diagrams is not included in this calculation.

1.2.4 Spin Correlation

All the calculations of $\sigma(\bar{p}p \rightarrow W^+W^-)$ discussed so far are done for real W^+W^- production. For off-shell W^+W^- in the channel $W^+W^- \rightarrow l^+l^-\nu\bar{\nu}$, it is trivial to calculate the full matrix element by a simple replacement in the amplitude expression. Figure 1.4 illustrates how this replacement is implemented for one of the two W bosons in W^+W^- production. The matrix element for on-shell W^+W^- is expressed in terms of the W polarization vector e^μ . The full matrix element for $W^+W^- \rightarrow l^+l^-\nu\bar{\nu}$ is obtained by replacing e^μ with the decay current j^μ

$$e^\mu \rightarrow j^\mu = g \langle l_2 | \frac{\sigma^\mu}{q^2 - M_W^2 + iM_W\Gamma_W} | l_1 \rangle, \quad (1.6)$$

where g is the coupling constant, and σ^μ is the Pauli matrix. M_W and Γ_W are the mass and decay width of W bosons, respectively.

Although this technique greatly simplifies the calculation of $\sigma(\bar{p}p \rightarrow W^+W^-)$, it cannot be used in the amplitudes which involve the virtual contribution from loop diagrams. The virtual correction for on-shell W^+W^- production, unlike other NLO contributions, is not proportional to the LO Born cross section, so the simple replacement does not hold in this case. To include the spin correlation in

loop diagrams, one has to calculate the whole matrix element, absorb the singular part, and combine the finite part with other amplitudes. Because the algebra involved is tremendously complicated, all publications so far have neglected the spin correlation for the virtual correction. The total cross section is changed by typically 10 % when the spin correlation is neglected. Fortunately, since the virtual correction is small (~ 10 % the size of the Born cross section), the change of $\sigma(\bar{p}p \rightarrow W^+W^-)$ is negligible when the spin correlation in loop diagrams is ignored.

1.3 Phenomenology of Anomalous Couplings

1.3.1 Formalism

The most general Lagrangian describing trilinear vector boson couplings, invariant under Lorentz, C, and P transformations, has the form

$$\begin{aligned} \mathcal{L}_{WWV} = & g_{WWV} [g_1^V (W_{\mu\nu}^+ W^\mu V^\nu - W_\mu^+ V_\nu W^{\mu\nu}) + \\ & \kappa_V W_\mu^+ W_\nu V^{\mu\nu} + \frac{\lambda_V}{M_W^2} W_{\lambda\mu}^+ W_\nu^\mu V^{\nu\lambda}], \end{aligned} \quad (1.7)$$

where g_{WWV} , W , and V are defined in the last section[1]. Terms with higher derivatives are equivalent to adding momentum-dependent couplings and thus merely lead to an introduction of form factors. These terms will be redundant if form factors are introduced separately. In the SM, all these coupling constants are fixed at tree level, with $g_1^V = 1$, $\kappa_V = 1$, and $\lambda_V = 0$.

In the low energy limit, the $WW\gamma$ terms in the effective Lagrangian correspond to the lowest order terms in a multipole expansion of W - γ interactions: charge Q , magnetic dipole μ_1 and electric quadrupole moment q_2

$$\begin{aligned} Q &= eg_1^\gamma, \\ \mu_1 &= \frac{e}{2M_W}(g_1^\gamma + \kappa_\gamma + \lambda_\gamma), \\ q_2 &= -\frac{e}{M_W^2}(\kappa_\gamma - \lambda_\gamma). \end{aligned} \quad (1.8)$$

Similar expansions can be obtained for the WWZ vertex. If W and Z have some internal structure, μ_1 and q_2 might have anomalous values.

Helicity amplitudes associated with anomalous couplings grow like \hat{s}/M_W^2 . This clearly violates the unitarity at high energy. To restore the unitarity, a generalized dipole form factor is introduced

$$\Delta\kappa_V(\hat{s}) = \frac{\Delta\kappa_V}{(1 + \hat{s}/\Lambda^2)^2}, \quad (1.9)$$

and similarly for other couplings, with the energy scale Λ beyond which new resonance particles, multiple boson production, and other new phenomena are expected. This form factor is designed to suppress helicity amplitudes at very high energy, but in the mean time remain essentially constant in the energy range we are interested. Nevertheless, limits on anomalous couplings extracted from experimental data explicitly depend on the choice of Λ . In this analysis, limits on anomalous couplings are obtained for $\Lambda = 1, 2$ TeV, and they are found not very sensitive to Λ .

1.3.2 Scenarios

So far there is no experimental evidence suggesting that the electroweak $SU(2) \times SU(1)$ gauge symmetry is violated, so it is a natural requirement that a phenomenological theory possess this symmetry. There are several scenarios in which the $SU(2) \times SU(1)$ gauge symmetry is realized. After boson interactions based on this symmetry are introduced, all anomalous couplings are related to each other by a set of loose constraints (Appendix A). One scenario assumes $\kappa_\gamma = \kappa_Z = \kappa$ and $\lambda_\gamma = \lambda_Z = \lambda$, with other parameters set at their SM values. If, on the other hand, λ_γ and κ_γ are chosen as independent parameters, the WWZ couplings are given by

$$\begin{aligned}\Delta g_1^Z &= \frac{1}{2\cos^2\theta_W}\Delta\kappa_\gamma, \\ \Delta\kappa_Z &= \frac{1}{2}(1 - \tan^2\theta_W)\Delta\kappa_\gamma, \\ \lambda_Z &= \lambda_\gamma.\end{aligned}\tag{1.10}$$

These equations define the HISZ scenario[8]. Later these two scenarios will be used to set limits on anomalous couplings.

1.3.3 Limits from Precision Measurements

Alternatively, taking account of loop contributions which involve $WW\gamma$ and WWZ vertices, one can indirectly set limits on anomalous couplings from precisely measured quantities. They include the g factor of muons, $b \rightarrow s\gamma$ and

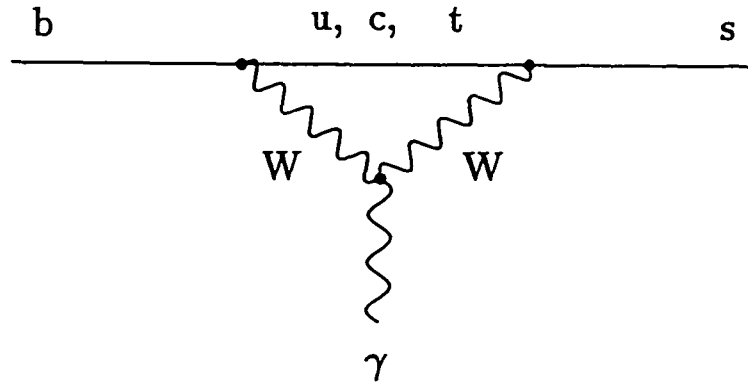


Figure 1.5: Feynman diagram for $b \rightarrow s\gamma$ decay. The decay rate depends on $WW\gamma$ couplings.

$Z \rightarrow b\bar{b}$ rates. As an example, Figure 1.5 illustrates how the decay rate of $b \rightarrow s\gamma$ is related to $WW\gamma$ couplings through loop corrections. Clearly, anomalous couplings will lead to a different decay rate.

It should be pointed out that precision measurements are barely sufficient to constrain all these parameters, and one often has to make stringent assumptions. Limits obtained from these measurements also strongly depend on other parameters such as the normalization scale, the Higgs and top quark masses, and the CKM matrix elements, which themselves present additional ambiguities[9]. For instance, if the top mass is varied from $150 \text{ GeV}/c^2$ to $200 \text{ GeV}/c^2$, the range allowed for anomalous couplings increases up to 50 %.

By contrast, direct measurements of W^+W^- production in $\bar{p}p$ collisions pro-

vide a straightforward test of these couplings, and no other theoretical assumptions or high order calculations are needed. Of course, higher order QCD corrections still pose a problem, but in terms of vector boson couplings, the interpretation of experimental results is unambiguous.

Chapter 2

Apparatus

This analysis uses the proton-antiproton collision data collected at the Collider Detector at Fermilab (CDF). A good understanding of apparatus is essential for any experimental analysis. In this chapter, I will describe the design and function of the Tevatron collider and CDF detector. The ongoing CDF upgrade is briefly discussed at the end.

2.1 Tevatron

The Tevatron collider, the world's largest proton-antiproton accelerator, is located at the Fermi National Accelerator Laboratory at Batavia, Illinois. It is operating at a center-of-mass energy $\sqrt{s} = 1.8$ TeV. The primary goal of the Tevatron is to study high transverse momentum phenomena in $\bar{p}p$ collisions. Figure 2.1 shows the general layout of the accelerator.

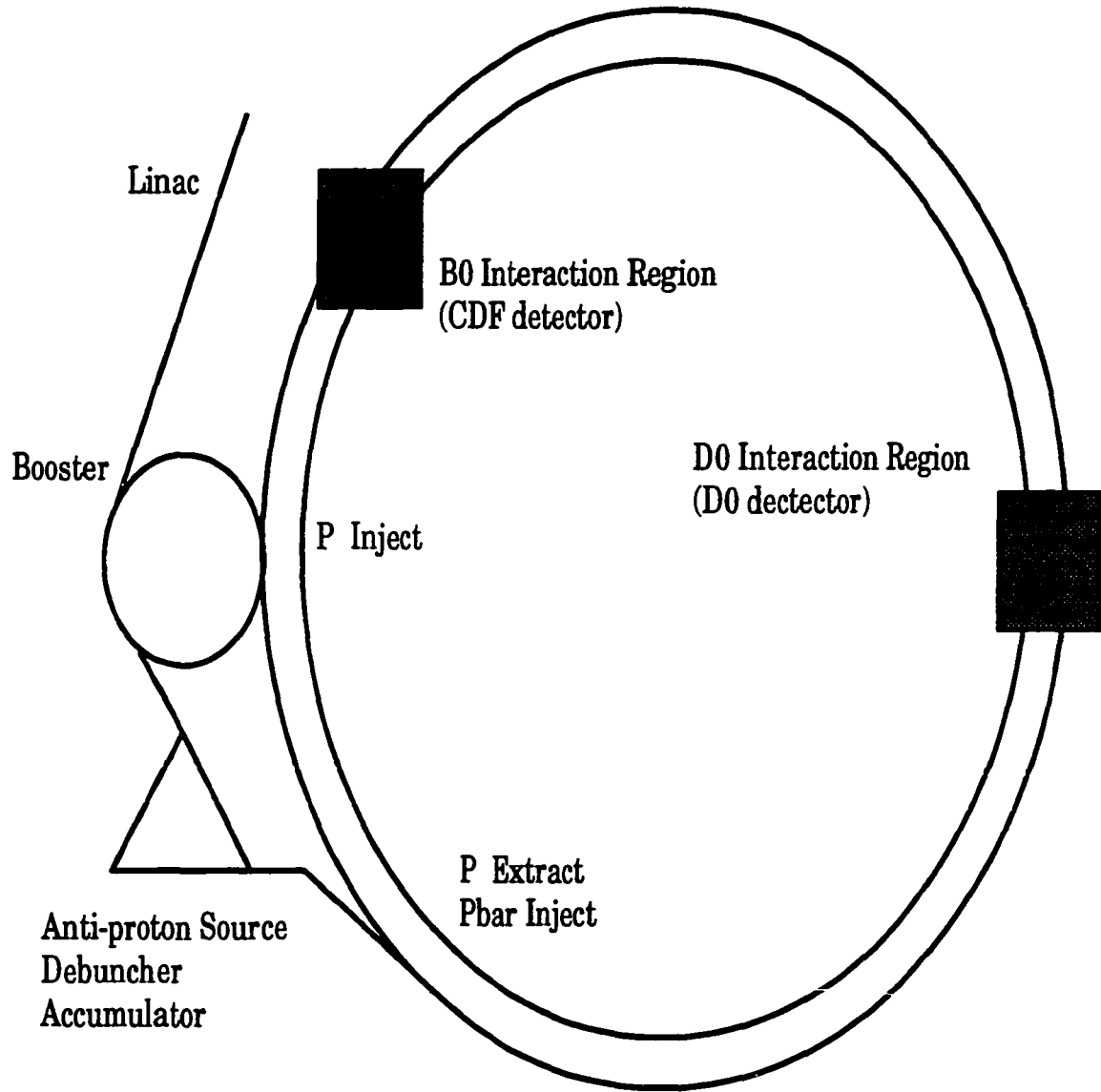


Figure 2.1: Overview of the Fermilab accelerator complex.

In the first step of particle acceleration in which 900 GeV proton and anti-proton beams are eventually generated, H^- ions produced in a Cockroft-Walton Generator are injected into a linear accelerator where they reach an energy of 0.5 GeV. Next in a booster ring the electrons attached to the ions are peeled off and the resulting protons are then accelerated to 8 GeV. Then proton beams are injected into the Fermilab Main Ring which is a proton synchrotron with a radius of 1 km. Proton beams from the Main Ring are focused on a tungsten target in order to produce antiproton beams. The antiprotons generated are stored and stochastically cooled in the storage ring, and then injected into an accumulator ring for further cooling. Then six bunches of protons and another six bunches of antiprotons are injected into the Tevatron and accelerated to 900 GeV at the final stage. In the Tevatron proton and antiproton beams are bent by a succession of dipole magnets, and focused by quadrupole magnets to increase their density. As they travel once around the Tevatron the bunches meet each at the CDF and other detectors.

2.2 CDF Detector

The Collider Detector at Fermilab is a general-purpose, multi-component detector. It has both azimuthal and forward-backward symmetry, and covers most of 4π solid angle[10]. A side-view of the detector is shown in Figure 2.2.

The CDF coordinate system defines the positive z axis along the direction

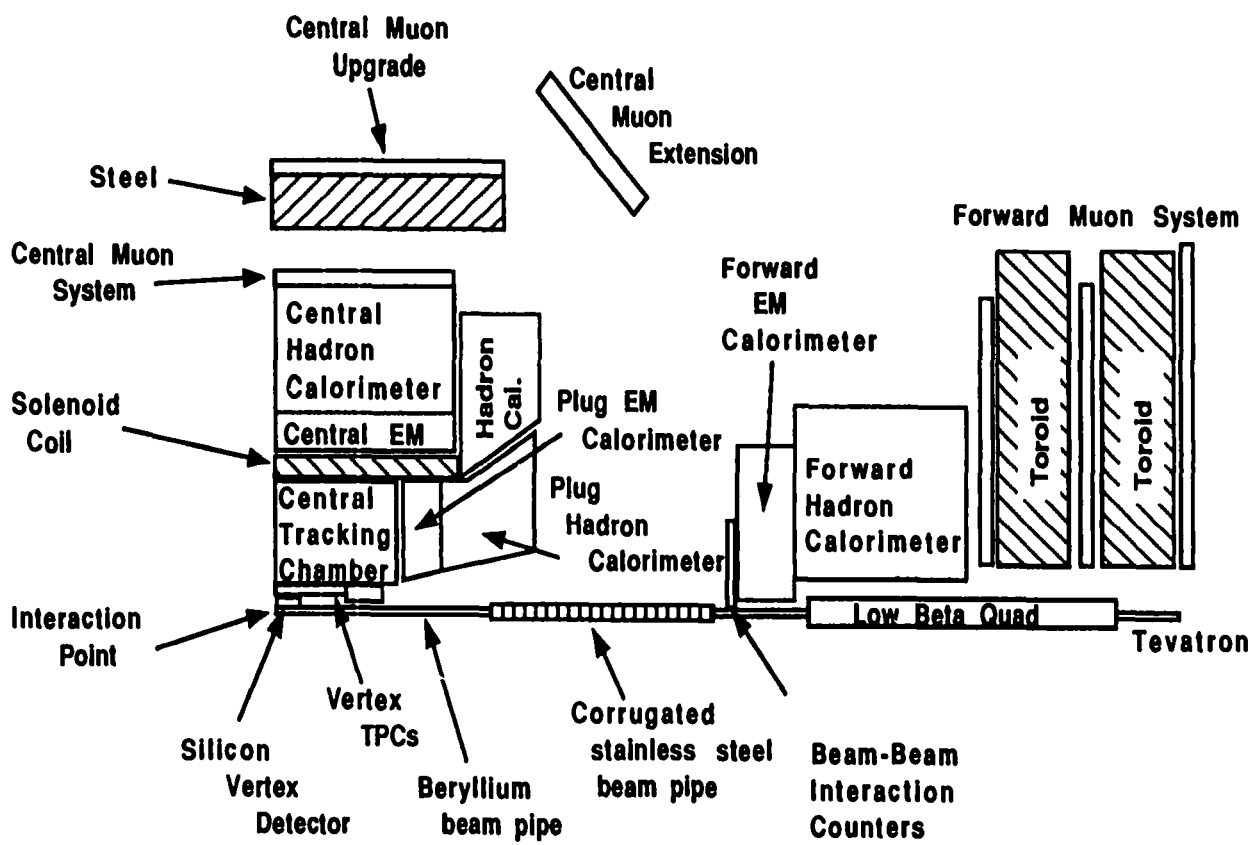


Figure 2.2: A quarter of the CDF detector. The detector is symmetric about the z axis and x-y plane.

of proton beams. The y axis is vertically upward and the x axis is radially outward from the center of the Tevatron ring. The detector is divided in terms of pseudorapidity variable $\eta = -\ln[\tan(\theta/2)]$ and azimuthal angle ϕ , where θ is the polar angle with respect to the z direction. It uses scintillator counters to measure luminosity. A superconducting solenoid provides a magnetic field of 1.4 T for momentum measurement of charged particles in the central ($|\eta| < 1.1$) region. The detector components directly involved in this analysis are the central and plug electromagnetic calorimeters, central and forward muon drift chambers, central tracking chamber, and vertex drift chamber. Other components serve in indirect ways, such as balancing transverse energy and detecting jets. In the following sections, I will give more detailed description of these components.

2.2.1 Luminosity

CDF uses two planes of scintillator counters to measure luminosity. Known as the beam-beam counters (BBC's), they cover the angular regions 0.32° to 4.47° and 175.53° to 179.68° ($3.24 < |\eta| < 5.88$). The rate of coincident hits, divided by the effective cross section of the counters (51.7 ± 1.7 mb), gives the instantaneous luminosity. The integrated luminosity is obtained by integrating the instantaneous luminosity over time.

2.2.2 Tracking

The CDF central tracking system is composed of a silicon vertex (SVX) detector located immediately outside the beampipe, a vertex (VTX) drift chamber outside the SVX, and a large central tracking chamber (CTC) contained within the uniform magnetic field region of the solenoid. The four-layer SVX is 51 cm long, covering roughly 60 % of the interaction region. These four layers provide a precision measurement of interaction points and tracks. The impact parameter resolution in the SVX system, a critical quantity for the measurement of particle lifetimes, is $\sigma = 17 \mu\text{m}$ (it plays a central role in the discovery of top quarks—tagging b jets which are associated with top quark production and have a long life time). The VTX system provides tracking information in the r - ϕ plane up to a radius of 22 cm and $|\eta| < 3.25$. The main function of the VTX system is to measure interaction points along the z axis. The VTX resolution of z vertices is about 1 mm. The CTC system encloses the VTX chamber and gives precise track momentum measurement in the region $|\eta| < 1.1$. The CTC system is a 3.2 m long drift chamber with an outer radius of 1.3 m, containing 84 layers of cylindrical sense wires, grouped into nine axial and stereo superlayers. Five axial superlayers consisting of 12 sense wire layers each provide tracking information in the r - ϕ plane. Four stereo layers have six sense wire layers each, tilted at $\pm 3^\circ$ relative to the beam direction. Together, the axial and stereo wires provide tracking information in the r - z plane. The momentum resolution of the CTC system

is $\delta P_T/P_T = 0.0020P_T$ (P_T in GeV/c thereafter) for isolated tracks, where P_T is the transverse momentum. A better resolution can be achieved if interaction vertices are included in the track-fitting procedure: $\delta P_T/P_T = 0.0011P_T$ in the CTC-VTX system, and $\delta P_T/P_T = [(0.0009P_T)^2 + (0.0066)^2]^{1/2}$ in the CTC-SVX system.

2.2.3 Calorimeters

The calorimeters have fine segmentation in the η - ϕ plane and are grouped into projective towers pointing towards the interaction region. The calorimeters cover all of ϕ , and extend to $|\eta| < 4.2$. Each calorimeter tower consists of an electromagnetic shower counter in front of a hadronic calorimeter element. In the central region ($|\eta| < 1.1$) the calorimeters are scintillator-based, while the plug and forward calorimeters are gas-based, using proportional tubes and cathode pad readout. Electrons and photons are identified by their localized kinetic energy deposition in the electromagnetic calorimeters. Muons are identified, in coincidence with hits in muon drift chambers, by their minimum ionizing energy deposition signature in the calorimeters. Jets are identified by their energy depositions in both electromagnetic and hadronic calorimeters.

The central electromagnetic (CEM) calorimeter ($|\eta| < 1.1$) is 18 radiation lengths thick and consists of polystyrene scintillator layers separated by lead sheets. Each tower is 15° wide in ϕ and 0.1 wide in η . The light from the scintillator is shifted through wavelength shifters coupled via light-guides to conventional

photomultiplier tubes. The CEM calorimeter has an energy resolution of $\delta E/E = 13.7 \% / \sqrt{E_T} \oplus 2\%$ (E_T in GeV thereafter) for incident electrons and photons, where E_T is the transverse energy, and \oplus indicates that the constant term is added in quadrature. To determine the position and transverse development of an electromagnetic shower at shower maximum (~ 6 radiation lengths), the central electromagnetic strip (CES) chambers are used to measure the charge deposition on orthogonal, fine-gained strips and wires. The CES chambers provide precise location of an electromagnetic shower in the z and $r-\phi$ views, with an accuracy of ~ 3.0 mm in $r-z$ and ~ 1.7 mm in $r-\phi$.

The central hadronic (CHA) calorimeter ($|\eta| < 0.9$) consists of steel absorber interspersed with acrylic scintillator, with a thickness of 4.5 absorption lengths. The CHA has an energy resolution of $\delta E/E = 50 \% / \sqrt{E_T} \oplus 3\%$ for incident isolated pions. The wall hadronic (WHA) calorimeter is similar to the CHA except that it covers $0.7 < |\eta| < 1.3$ and has a slightly worse resolution ($\delta E/E = 75 \% / \sqrt{E} \oplus 4\%$).

The plug electromagnetic (PEM) calorimeter ($1.1 < |\eta| < 2.4$) is divided into quadrants. It is constructed from lead absorber panels sandwiched with gas proportional chambers with cathode pad readout. The thickness of the PEM varies from 18 radiation lengths in the middle to 21 radiation lengths near the edge. The tower size is 5° wide in ϕ and 0.1 wide in η . The PEM system has an energy resolution of $\delta E/E = 22 \% / \sqrt{E} \oplus 2\%$. Shower positions are determined from θ and ϕ pad information, with a spatial resolution of $2 \text{ mm} \times 2 \text{ mm}$.

The forward electromagnetic (FEM) calorimeter ($2.2 < |\eta| < 4.2$) is also constructed from lead absorber panels interspersed with gas proportional wire chambers and cathode pad readout, with a thickness of 25 radiation lengths. The tower size is 5° wide in ϕ and 0.1 wide in η . The FEM system has an energy resolution of $\delta E/E = 26\% / \sqrt{E} \oplus 2\%$. Shower positions are determined from θ and ϕ pad information, with a spatial resolution of 1 – 4 mm, depending on the shower location in the calorimeter.

The plug (PHA) and forward (FHA) hadronic calorimeters are constructed from steel absorber separated by gas proportional chambers. The PHA ($1.3 < |\eta| < 2.4$) is 5.7 absorption lengths thick and has an energy resolution of $\delta E/E = 106\% / \sqrt{E} \oplus 6\%$ for isolated incident pions. The FHA ($2.4 < |\eta| < 4.2$) is 7.7 absorption lengths thick and has an energy resolution of $\delta E/E = 137\% / \sqrt{E} \oplus 3\%$ for incident isolated pions.

2.2.4 Central Muon Chambers

The central muon (CMU) chambers consist of drift chambers behind the central calorimeters which, with a thickness of approximately 5 absorption lengths of lead and steel, act as a hadron absorber. Four layers of drift cells in a muon chamber provide three-dimensional reconstruction of tracks from drift-time information in the transverse (r - θ) direction with a drift resolution $\sigma = 250 \mu\text{m}$. Behind the CMU system are 0.6 m of steel and four more layers of drift chambers for additional hadron absorption. This system is referred to as the central muon

upgrade (CMP) system. In the region $|\eta| < 0.6$, approximately 84 % of the solid angle is covered by the CMU system, 63 % by the CMP system, and 53 % by both. For solid angle $0.6 < |\eta| < 1.0$, additional drift chambers sandwiched between scintillator counters were added in 1992, and are referred to as the central muon extension (CMX) system. Approximately 70 % of the solid angle for $0.6 < |\eta| < 1.0$ is covered by the CMX system. In all central muon systems, muon P_T and its resolution are determined by the tracking systems discussed earlier.

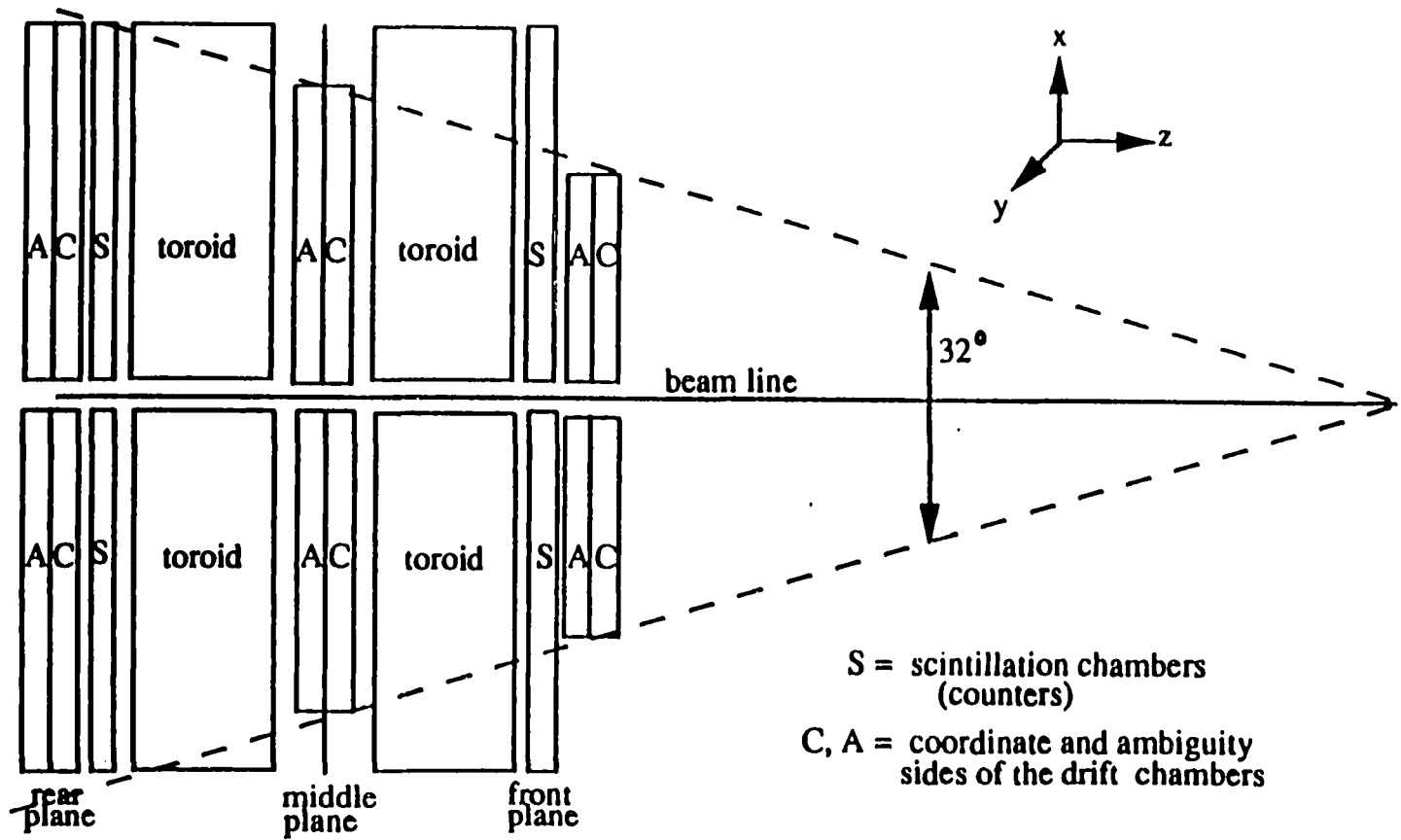
2.2.5 Forward Muon Detector

The forward muon (FMU) system consists of two spectrometers covering the small angle regions $5^\circ < \theta < 15^\circ$ and $165^\circ < \theta < 175^\circ$ as shown in Figure 2.3. Like all muon detectors, the FMU system is located behind the electromagnetic and hadronic calorimeters so that jets are most likely stopped before they reach the FMU detector. The charge and momentum information of muons is extracted from their trajectories in the FMU region. In this section, I will describe the design and function of the toroids, chambers, scintillator counters, triggers and other FMU apparatus.

2.2.5.1 Toroids

Two steel toroid magnets are located at each of the forward and backward regions, each with a dimension of 7.6 m o.d. \times 1.0 m i.d. \times 1.0 m. Copper coils with current 600 Amps provide an azimuthal magnetic field in the toroids. A thorough

Figure 2.3: A side-view cross section of the FMU detector.



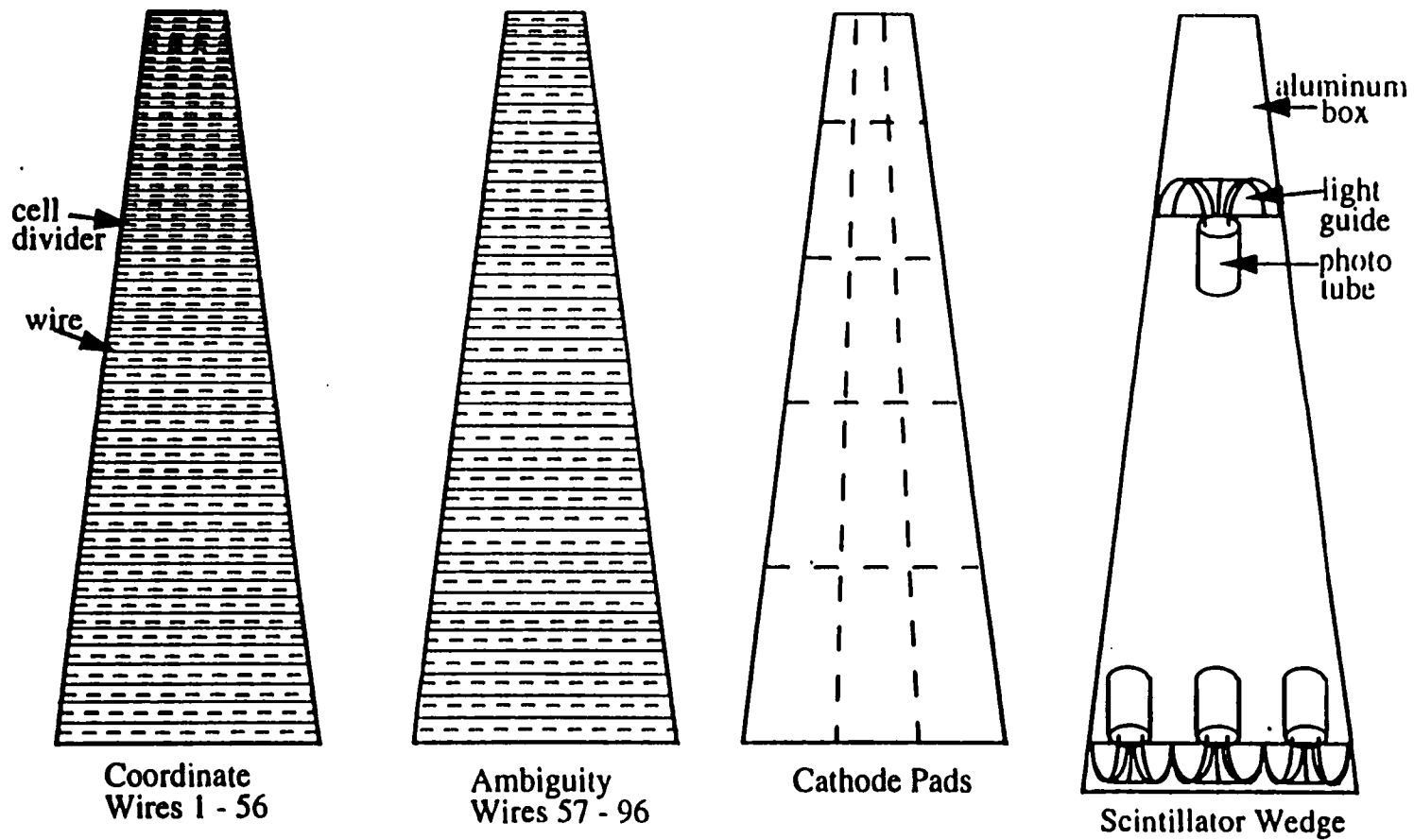
knowledge of the magnetic field is crucial to the FMU momentum measurement, so Appendix B is devoted to field mapping procedures and results. The mapping of the field will help to improve the momentum resolution of the FMU system.

2.2.5.2 Chambers

At each end of the CDF there are three drift chambers located in the front, middle, and rear planes. They are used to measure the position of forward muons, and thus provide charge and momentum information. Each plane consists of 24 chamber wedges as shown in Figure 2.4.

A drift chamber contains two planes of drift cells to resolve the left-right ambiguity: a coordinate plane of 56 wire cells, and an ambiguity plane of 40 wire cells. Therefore a forward muon will go through six planes (three coordinate planes and three ambiguity planes), and leave six hits on sense wires for pattern reconstruction (patterns with less than five hits are rejected). A common copper foil cathode plane (PAD) divides a chamber into 5° wedges in ϕ . Wires and PADs are arranged to form projective towers. Anode wires are held at high voltages and a PAD forms the ground plane between the two sides of a chamber. The drift chambers contain a mixture of 50/50 argon-ethane gas with a constant drift velocity of $5 \text{ cm}/\mu\text{s}$. Sense wires are read out by TDC cards, while PADs are read out by the RABBIT electronics. Three adjacent sense wires are grouped together to reduce the number of electronics channels. The ϕ segmentation is left to PADs and scintillator counters. The average position resolution is about 600

Figure 2.4: Schematic of the FMU chamber.



μm .

2.2.5.3 Scintillator Counters

At each end of the CDF, one scintillator plane is placed in front of the front plane of drift chambers and other behind of the rear plane of drift chambers. Each scintillator plane is segmented into 5° wedges with four Amperex 2202B photomultiplier tubes for each wedge. A Schmitt-trigger circuit is installed at each phototube base to provide an ECL logic pulse for trigger logics.

One important feature of scintillator counters is their noise rate, which is recorded during the quiet time (no beams in the detector). One can monitor the stability of scintillator counters by examining the noise rate over a period of time. It can also serve as a diagnosis tool. Figure 2.5 illustrates how this can be achieved. The 5° scintillator wedges are numbered in the following way: 0–71 for the west front, 72–143 for the west rear, 144–215 for the east front, and 216–287 for the east rear. The noise rate is counted in an interval of 10 seconds. Normal counts range from 1,000 to 5,000. Clearly peaks above this normal range indicate either leakage of light or electronics oscillations at the corresponding wedges. Also the average noise rate is recorded every day so one can monitor the counter performance over a long period. Figure 2.6 shows the average noise rate from March to July of 1994. This plot could be used to adjust the high voltages of tubes so that the gain of scintillator counters remain unchanged over the run period. Although it was relatively stable, the noise rate increased slightly during

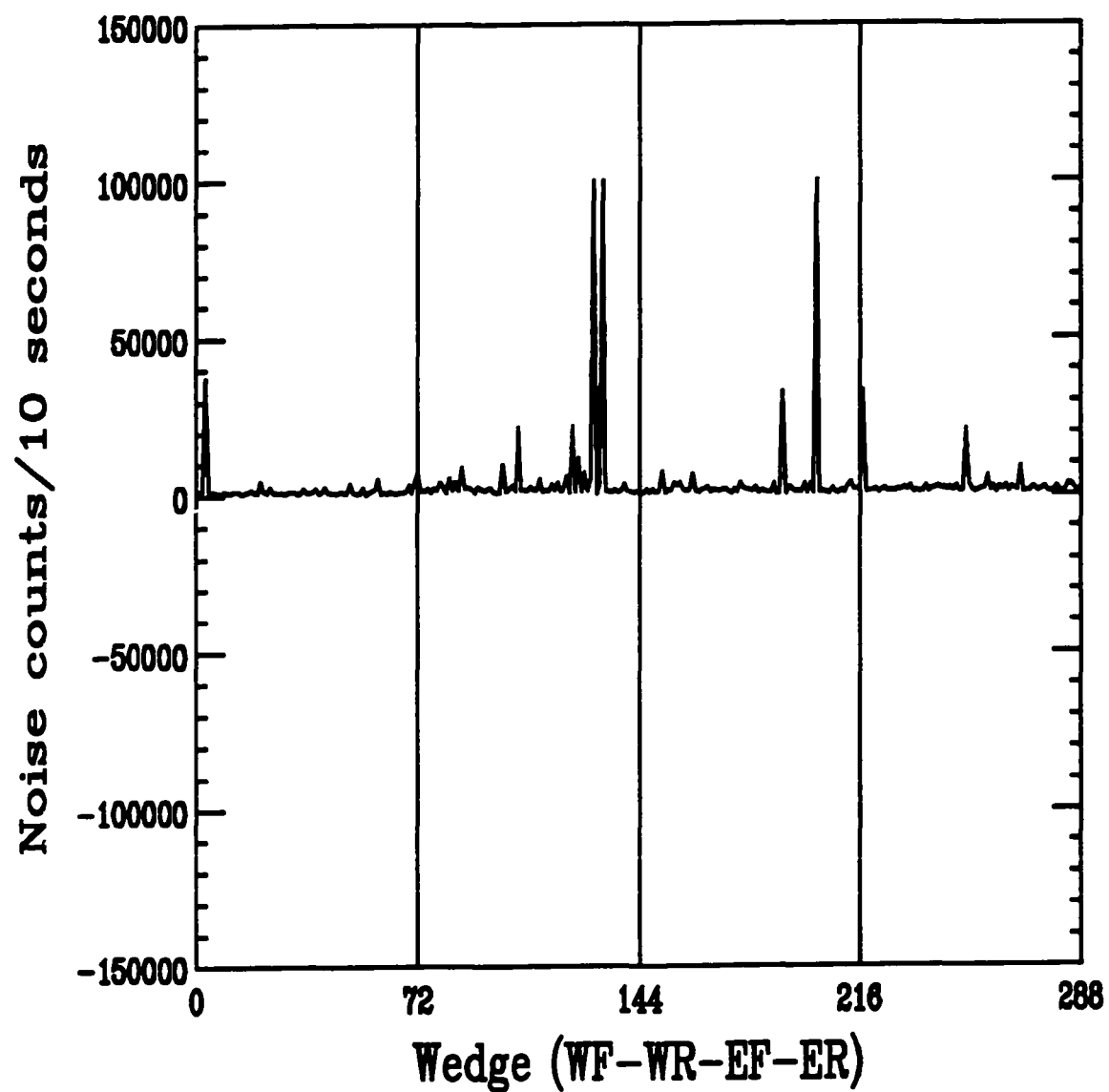


Figure 2.5: Scintillator counter noise rate. Wedges are divided into the west front (WF), west rear (WR), east front (EF), and east rear (ER) planes. Each plane has 72 wedges.

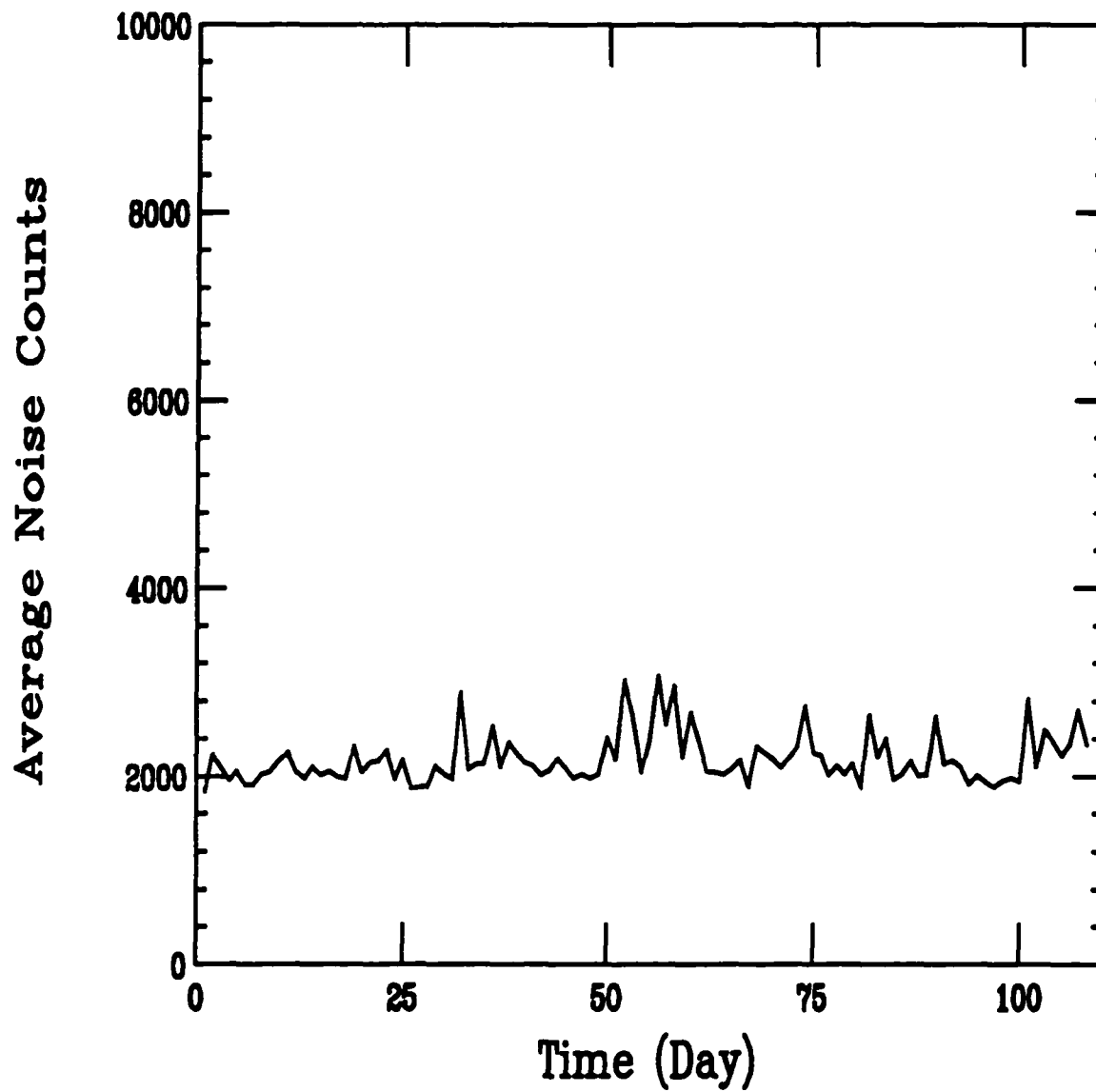


Figure 2.6: Scintillator noise rate evolution with time.

this period—an indication of aging effect.

2.2.5.4 Triggers

The FMU trigger configuration takes advantage of the sophisticated structure of the FMU system: six hits in the drift chambers, confirmed hits from the PADs and scintillator counters in the same octant.

A valid track road on the drift chambers is defined as having three hits on the coordinate planes and three hits on the ambiguity planes in the same octant. This is achieved with trigger boards called NUPU (new half octant pattern units) which originate from old boards HOPU (half octant pattern units). The signal from a chamber cell is sent to a preamplifier ($\times 40$). Then this signal is shifted to an amplifier/discriminator board which sends a logic pulse if the incoming signal is above a pre-fixed threshold. The NUPU boards take the wire pulses from three TDC boards associated with the front, middle and rear planes, and search for a valid pattern according to the pattern classification discussed earlier.

As mentioned before, the scintillator counters and PADs are divided into 5° wedges in the azimuthal plane. The PAD signals are read out by the RABBIT crates and a logic pulse is sent whenever there is a hit on a PAD wedge. Signals from the scintillator counters and PADs are correlated in a circuit board called SINPAD, and therefore the FMU ϕ resolution is restored to 5° .

Finally, trigger signals from the NUPU and SINPAD are sent to a trigger board called PUCKER where they are added together. A trigger latch is set if

there is a coincidence within one octant. The trigger efficiency is about 70 %.

A computer program is available to analyze FMU triggers. It uses CMU-FMU dimuon events triggered by CMU muons. First, FMU data banks are looped over to locate muons in the FMU fiducial region. Then this program looks for patterns along the track roads and decides if they are valid FMU muons: wire hits in the coordinate and ambiguity planes; hits on the scintillator counters and PADs. It can also serve as a diagnosis tool. Figure 2.7 gives an example how it works for the SINPAD trigger. In the second octant, for instance, there is no FMU muon trigger bit in the FMU trigger bank. However, seven FMU muons hit this octant according to this trigger program which is based on CMU volunteer triggers. This is a clear indication of a hardware failure of either scintillator counters or PADs in this octant. This program can also be used to calculate the FMU trigger efficiency in the same fashion as it detects hardware failures.

2.2.5.5 Momentum Resolution

The momentum resolution of the FMU system has three components: multiple scattering, chamber resolution, and uncertainty in the chamber positions from the survey.

Multiple scattering is the result of electromagnetic interactions between incident particles and target nuclei in the medium. Its contribution is momentum

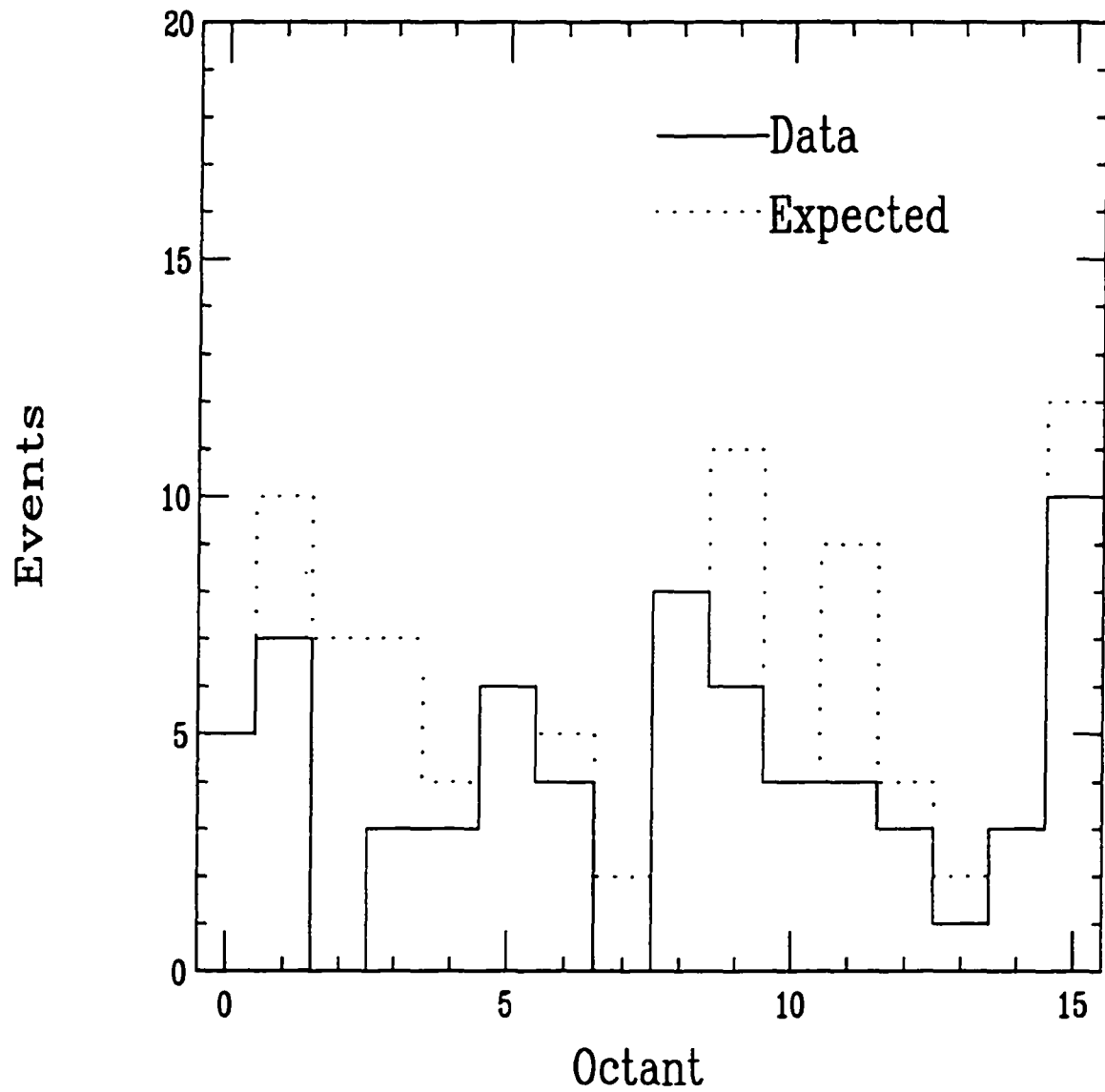


Figure 2.7: FMU events detected by the SINPAD trigger board. The dotted histogram indicates the number of events that should be triggered, while the solid histogram shows the actual triggered events.

independent, and is found to be (P in GeV/c)[11]

$$\frac{\Delta P}{P} = 0.166.$$

The chamber resolution comes from the intrinsic resolution of electronics and pulse signals. A detailed analysis of FMU data finds the chamber position resolution to be about $650 \mu\text{m}$, which corresponds to[12]

$$\frac{\Delta P}{P} = (0.0015 \pm 0.0003)P.$$

Finally, the survey misalignment of chambers also contributes to the momentum resolution[11]

$$\frac{\Delta P}{P} = (0.0012 \pm 0.0003)P.$$

The combined resolution of these three components is give by

$$\frac{\Delta P}{P} = [(0.166)^2 + (0.0019P)^2]^{1/2}.$$

2.3 CDF Upgrade

The CDF detector has been going through a major upgrade to exploit a much higher luminosity in the future. A new Main Injector accelerator is currently under construction. The future luminosity is expected to be greater than $2 \times 10^{32} \text{cm}^{-2} \text{sec}^{-1}$ and the bunch spacing as small as 132 ns. The current CDF detector was designed for luminosity up to $10^{30} \text{cm}^{-2} \text{sec}^{-1}$ and bunch spacing 3.5

μsec . Clearly, many parts of the existing system must be upgraded or replaced to meet these new parameters. Figure 2.8 shows the proposed CDF detector for Run II. In this section, I will briefly discuss the upgrade project.

The scintillator-based CEM and CHA systems only experience a slightly aging effect, about 1 % of yield loss per year. The plastic scintillator counters and wave-shifters should not have any serious radiation damage problem. So the central calorimeters will remain essentially unchanged.

The gas chamber-based plug and forward calorimeters are going to be replaced by new, more compact calorimeters. The new calorimeters are scintillator-based: lead and scintillator for the electromagnetic calorimeters; iron and scintillator for the hadronic calorimeters.

The existing 51 cm long SVX system just covers about 60 % of the interaction region and experiences some radiation damage to the readout chips. The proposed new SVX system (SVX II) will be 87 cm long, almost double the current coverage. The five layers of the SVX II will be double-sided, which enables the SVX II to construct three-dimensional tracks. The current SVX can only provide two-dimensional tracking information.

The CTC system is observed to experience an aging effect: The tracking efficiency continues to decline. Also the maximum drift time in the CTC system is ~ 800 ns, far longer than the beam crossing space of 132 ns. The vertex drift chambers have to be removed to leave the space for new designs. The function of the VTX system and the inner layers of the CTC system will be taken over

The CDF Upgrade

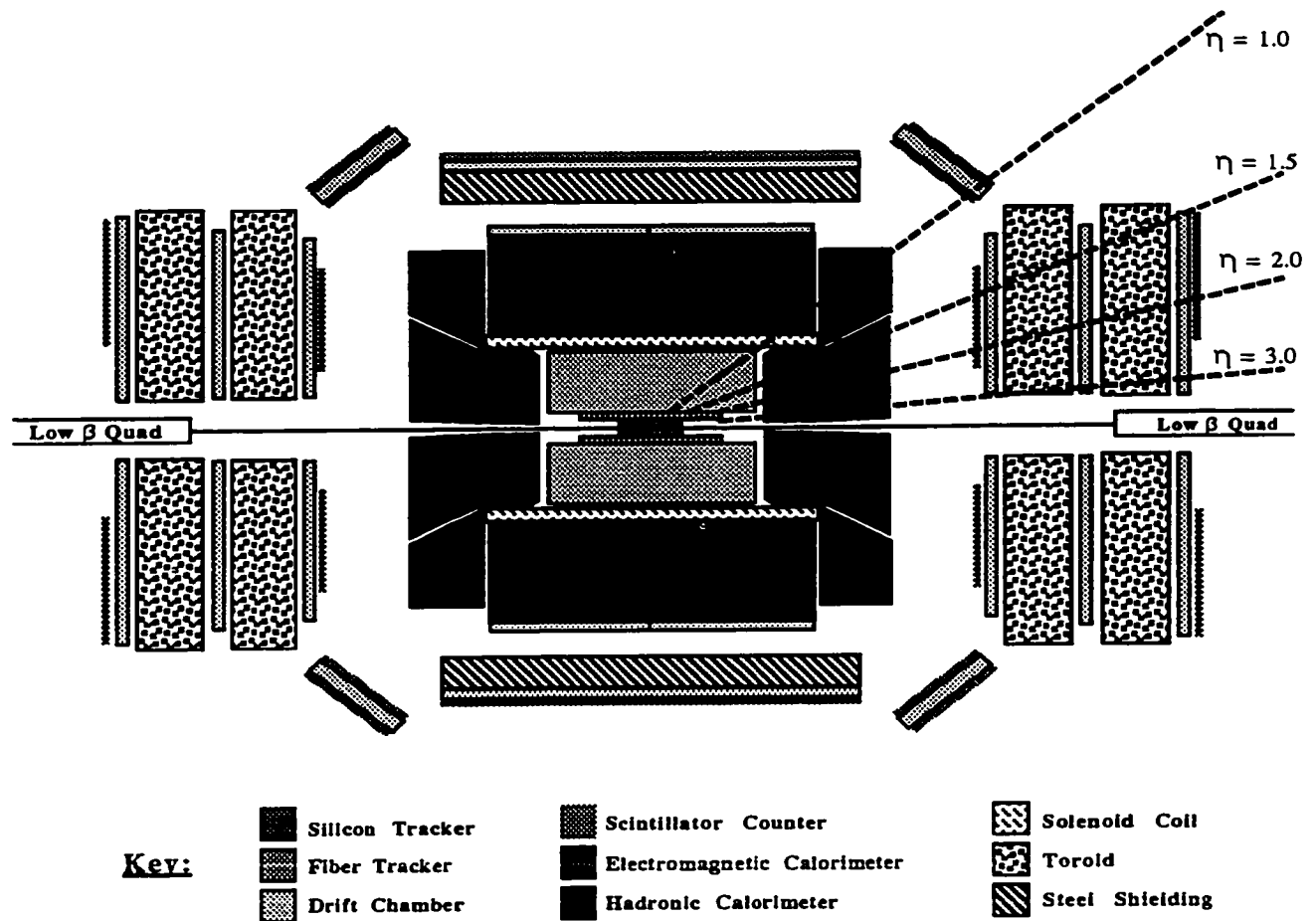


Figure 2.8: Proposed CDF detector for Run II.

by an Intermediate Fiber Tracker (IFT). The IFT system consists of a set of cylindrical scintillating fiber layers outside the SVX II. The resolution is of the order of $100 \mu m$, compatible to the design of the SVX II (resolution $\sigma = 15 \mu m$). Straw chambers have been proposed to take over the role of the CTC system. The basic elements are small diameter straw tubes. They are configured into four superlayers, each consisting of axial and stereo layers of straw tubes. This structure will suit the Run II conditions, namely high luminosity and short crossing time.

For the central muon system, more chambers will be added to increase its coverage. As a result, the fraction of the CMU system covered by the CMP system will be increased from 70 % to 85 %. The CMX will be completed by filling ϕ gaps at the top and bottom of the existing system. The ϕ coverage will increase from current 66 % to 93 %. The FMU system will be moved closer to the interaction point as the current plug and forward calorimeters will be replaced by more compact ones. The η coverage will change from 2.0–3.6 to 1.5–3.0.

The higher luminosity and shorter beam crossing time in the future require that the front-end electronics have more event storage capacity, earlier signal digitization, and faster trigger decisions. This will be accomplished by the technology based on the charge integrating and encoding (QIE) chips. The existing RABBIT crates will be replaced by 9U VME crates.

The existing CDF systems have been extremely successful in a wide variety of physics topics: top quark discovery, diboson production, W mass measure-

ment, and other physics processes. The new upgrade system will provide a more powerful tool for physicists in the field of particle physics.

Chapter 3

Data Selection

Since this analysis focuses on the dilepton channel $W^+W^- \rightarrow l^+l^-\nu\bar{\nu}$, we are interested in events with two high P_T leptons and a large missing transverse energy \cancel{E}_T from the two neutrinos. Most of lepton selection criteria, such as electromagnetic shower profiles, are more or less fixed in the sense that they have been scrutinized for a long time and there is a general consensus regarding the thresholds of these selection cuts. Other selection cuts, such as lepton momentum P_T , are constrained by run conditions—trigger tables and available data samples. Nevertheless, there is still room to optimize these cuts so that we can get maximum acceptance and keep backgrounds under control at the same time. In this chapter I will outline single-lepton selection cuts for central electrons, plug electrons, central muons, and forward muons. Leptons from other regions of the CDF detector are not included because they either introduce an unacceptable

large background or have poor resolutions, or contribute very little to the total acceptance. As a crucial part of W^+W^- search, cuts on jets and \cancel{E}_T are also discussed.

3.1 Central Electrons

3.1.1 Triggers

Electrons detected in the central electromagnetic (CEM) calorimeter are called central electrons. This calorimeter covers the pseudorapidity region $|\eta| < 1.1$. The calorimeter trigger first requires a single EM tower in the central region with E_T above a threshold of 6 GeV. Then an EM cluster is constructed starting from a seed tower with $E_T > 9$ GeV and extending to neighboring towers with $E_T > 7$ GeV, but limited to three towers in pseudorapidity ($\Delta\eta = 0.3$) and one tower in azimuth ($\Delta\phi = 15^\circ$). In the next level of the central electron trigger, a CTC track, above a threshold of $P_T > 9$ GeV/c, that extrapolates to this cluster is required. The tracking information is analyzed and sent to the trigger supervisor by a hardware track processor [central fast tracker (CFT)]. Finally, the level-3 algorithm requires $E_T > 18$ GeV and $P_T > 13$ GeV/c.

3.1.2 Selection Cuts

For central electrons, fiducial cuts on the EM shower positions excluding calorimeter boundaries ensure that the energy is well measured. Electrons from converted photons can be removed with high efficiency by exploiting their tracking information: Any electron that does not have a matching VTX track, or that can be paired with an oppositely charged CTC track to form a small effective mass ($M_{ee} < 500 \text{ MeV}/c^2$), is rejected as a photon conversion candidate.

Hadrons and jets usually go through the CEM calorimeter and may be misidentified as electrons. A set of electron identification cuts are used to identify electrons and remove charged hadrons. For an EM cluster in the CEM calorimeter:

- The hadronic energy fraction of the cluster, HAD/EM, should be small;
- The ratio of cluster energy to track momentum, E/P, should be close to 1;
- The lateral shower profile L_{shr} (defined below) is compared with the standard shower shape from test beam electrons, and the difference should be negligible;
- The distance between the position of the extrapolated track and the shower position measured by the strip chambers in the CEM calorimeter, viewed in the r - ϕ (Δx) and z (Δz) planes, should be within tolerance;
- At least one track is pointed to the cluster, and the track must satisfy some minimum hit requirements (3D track) in the CTC superlayers;

- The χ^2 comparison of the strip chamber shower profile with that from test beam electrons, χ_{strip}^2 , should be reasonable ;
- The distance between the event vertex and the reconstructed track in the z direction, z-vertex match, should be within tolerance;
- The distance between the interaction vertex and the center of the detector in the z direction, z0, should be within some range so that luminosity is well measured.

The lateral shower profile L_{shr} introduced earlier is defined by

$$L_{shr} = 0.14 \sum_i \frac{E_i^{adj} - E_i^{prob}}{[(0.14E)^2 + (\Delta E_i^{prob})^2]^{1/2}}. \quad (3.1)$$

Here, E_i^{adj} is the measured energy in the tower adjacent to the seed tower; E_i^{prob} is the expected energy in that tower calculated from the seed energy of the cluster, the impact point from the strip chamber, and the event vertex using a shower profile parameterization from test beam data; and ΔE_i^{prob} is the error in E_i^{prob} associated with a 1-cm error in the impact point measurement.

Two isolation cuts are imposed on a central electron: 1) calorimeter isolation, defined as the ratio of the transverse energy in the EM towers within a cone of radius 0.4 in the η - ϕ plane centered on the electron but excluding the transverse energy of the electron cluster, to the transverse energy of the electron; 2) track isolation, defined as the ratio of P_T sum of CTC tracks within a cone of radius 0.4 but excluding the electron track contribution, to the electron momentum.

Variable	Cut
E_T	$> 20 \text{ GeV}$
P_T	$> 10 \text{ GeV}/c$
HAD/EM	< 0.05
L_{shr}	< 0.2
E/p	< 2
$ \Delta x $	$< 1.5 \text{ cm}$
$ \Delta z $	$< 3 \text{ cm}$
z-vertex match	$< 5 \text{ cm}$
$ z_0 $	$< 60 \text{ cm}$
χ^2_{strip}	< 10
3D tracks	≥ 1
Iso	< 0.1
Fiducial cut	C\$ELE:FIDELE module

Table 3.1: Central electron selection cuts.

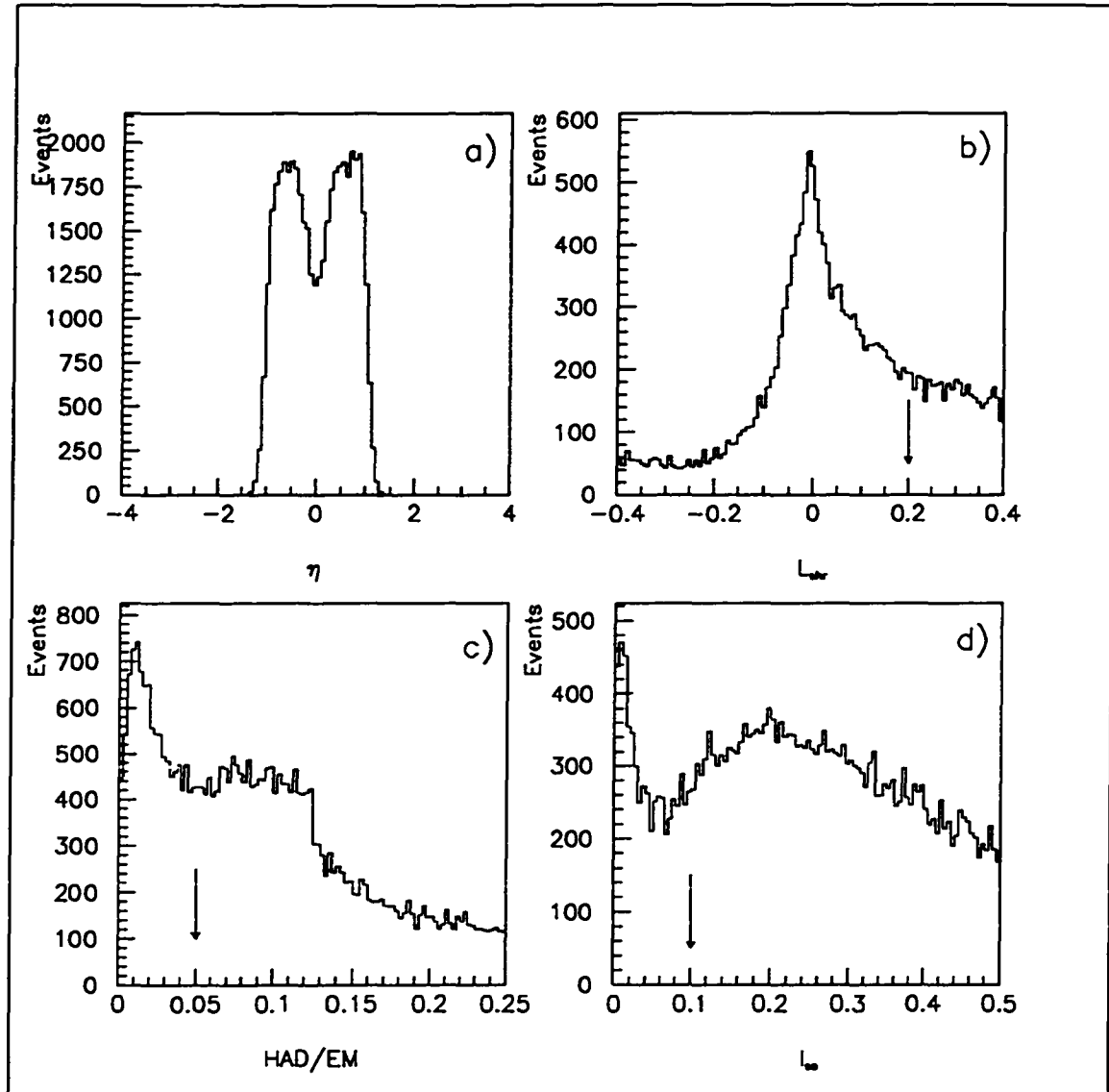


Figure 3.1: Pseudorapidity distribution and quality variables of central electrons. (a) pseudorapidity, (b) lateral shower profile variable, (c) ratio of hadronic and electromagnetic energy, and (d) calorimeter isolation variable. Arrows denote the values of the selection cuts.

All these cuts are listed in Table 3.1. Figure 3.1 shows some distributions of the central electron variables. Studies of $Z \rightarrow e^+e^-$ events show that the central electron selection efficiency (sometimes called identification efficiency) is 81.3 % [13, 14]. Here a Z boson is defined as an e^+e^- pair with invariant mass between $75 \text{ GeV}/c^2$ and $105 \text{ GeV}/c^2$. The procedure is as follows: First select those $Z \rightarrow e^+e^-$ events with one central electron passing all cuts and a second object in the electron data bank. Then one by one, the electron identification cuts are imposed on the second EM cluster to obtain cut efficiencies. Finally, all individual cut efficiencies are combined to give a total identification cut efficiency.

3.2 Plug Electrons

3.2.1 Triggers

Electrons detected in the plug electromagnetic (PEM) calorimeter are called plug electrons. The coverage of the PEM system is $1.1 < |\eta| < 2.4$. The PEM calorimeter trigger requirements are quite similar to those for the CEM calorimeter. However, there are some differences. The seed tower threshold is $E_T = 6 \text{ GeV}$, and the cluster developed from this seed tower can have as many as five towers in pseudorapidity ($\Delta\eta = 0.5$) and up to five towers in azimuth ($\Delta\phi = 25^\circ$), with $E_T > 4 \text{ GeV}$ for each tower. The level-3 trigger requires $E_T > 20 \text{ GeV}$. Since the CTC coverage only extends to $|\eta| = 1.0$, no tracking requirement is imposed

on the PEM trigger.

3.2.2 Selection Cuts

Fiducial cuts are applied to plug electrons to ensure that EM energy clusters are away from the boundaries and cracks of the PEM calorimeter. The following variables are used to identify plug electrons:

- HAD/EM, same as for central electrons;
- The χ^2 comparison of the longitudinal and transverse shower profiles, χ_{depth}^2 and $\chi_{3\times 3}^2$, with those from test beam electrons, should be reasonable;
- The occupancy of VTX hits should not be too low;
- 3D tracks, same as for central electrons.

A few issues need to be addressed regarding the plug electron selection. First, the χ_{depth}^2 cut is not applied to those plug electrons near the boundary of the plug calorimeter because there is no “standard shape” of showers in this region. A standard shower shape in the longitudinal direction is obtained from W and Z electrons. A candidate shower shape is then compared to this standard with χ_{depth}^2 representing how well the shower matches the standard shape. Unfortunately, this standard shape has only been developed for electrons which are near the center of the plug calorimeter, where the shower traverses all three longitudinal segments. In other words, χ_{depth}^2 cannot be defined for electrons near the outer edge of the

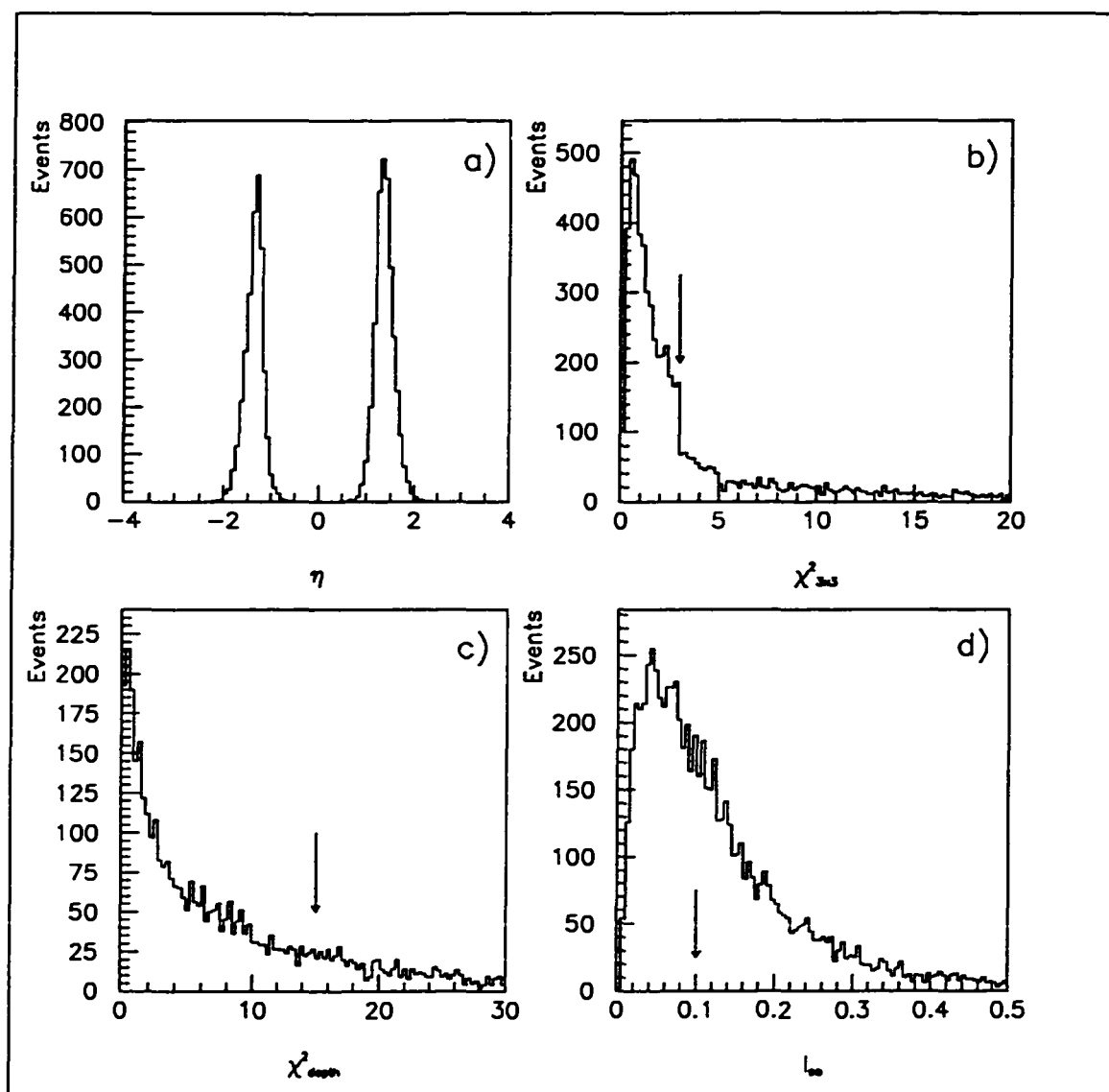


Figure 3.2: Pseudorapidity distribution and quality variables of plug electrons. (a) pseudorapidity, (b) χ^2 for the electron hypothesis from the shape of the shower in the transverse direction, (c) χ^2 for the electron hypothesis from the shape of the shower in the longitudinal direction, and (d) calorimeter isolation variable. Arrows denote the cutoffs used in the plug electron selection.

Variable	Cut
E_T	$> 20 \text{ GeV}$
HAD/EM	< 0.05
3D tracks	≥ 1
χ_{depth}^2	< 15
$\chi_{3 \times 3}^2$	< 3
VTX occupancy	$> 50\%$
I_{so}	< 0.1
Fiducial cut	C\$ELE:FIDELE module

Table 3.2: Plug electron selection cuts.

plug calorimeter. The corresponding η tower addresses are 31, 32, 53, and 54. The second issue is that, except the 3D track requirement, no tracking quality cuts are applied to plug electrons because of the limited coverage of the CTC system. Again, plug electrons are required to pass both calorimeter and track isolation cuts (same as for central electrons).

Table 3.2 lists all these cuts. Again $Z \rightarrow e^+e^-$ data samples are used to get the plug electron selection efficiency. First select those $Z \rightarrow e^+e^-$ events with one central electron passing all cuts and a second PEM object in the data bank. Then the selection cuts are imposed on the PEM cluster. The efficiency is found to be 85.7 % [13, 14]. Figure 3.2 shows some distributions of the plug electron variables.

3.3 Central Muons

3.3.1 Triggers

The coverage of central muon chambers is $|\eta| < 0.6$ by the central muon (CMU) system, $0.6 < |\eta| < 1.0$ by the central muon extension (CMX) system. The central muon upgrade (CMP) system doesn't trigger a muon event. The central muon trigger requires a track segment in the CMU system with $P_T > 6$ GeV/c in coincidence with hits in the CMP system when available, or a track segment in the CMX system with $P_T > 10$ GeV/c. Next, the muon trigger matches this track segment in the CMU or CMX with a track pattern with $P_T > 9$ GeV/c in the CTC system. The level-3 trigger selects only those muons with $P_T > 18$ GeV/c.

3.3.2 Selection Cuts

A muon candidate is expected to have a minimum ionizing energy when it goes through the calorimeters. This is one of the key criteria used to separate muons from hadrons. A list of muon selection cuts are as follows:

- Energy deposited in the electromagnetic and hadronic calorimeters, EM and HAD, must be of the order of characteristic of minimum ionizing particles;
- The closest distance between a muon track and the beam line, d_0 (impact parameter), should be small in order to reduce backgrounds from cosmic

rays and π/K decays;

- The distance between the event vertex and the reconstructed track in the z direction, z -vertex match, should be within tolerance;
- The matching distance between the extrapolated track and the track segment in the muon chambers, Δx , should be small;
- The number of hits in the CTC superlayers should meet some minimum requirements;
- The interaction vertex z_0 , same as for central electrons.

Both calorimeter and track isolation cuts (same as for central electrons) are applied to central muons in order to reduce jet backgrounds. Table 3.3 specifies all these selection cuts. Here I will address a few additional issues regarding muon selection. They are important for removing backgrounds and getting precise measurements.

First, muon candidates are required to pass a cosmic filter at the muon level-3 trigger. If two muons with oppositely charged tracks are back-to-back ($|\Delta\phi| > 178^\circ$ in the ϕ plane and $|\eta_1 + \eta_2| < 0.2$ in the η plane), they are removed as cosmic rays. Also if a pair of muons trigger two hadronic TDC's and the timing is above a threshold, these two muons are rejected[15]. To remove the residual cosmic rays in the dimuon channel, I also apply one additional cut which will be discussed in next chapter.

Variable	Cut
P_T	$> 20 \text{ GeV}/c$
EM	$< 2 \text{ GeV}$
HAD	$< 6 \text{ GeV}$
EM + HAD	$> 0.1 \text{ GeV}$
$ \Delta x $ (CMU)	$< 5 \text{ cm}$
$ \Delta x $ (CMP)	$< 10 \text{ cm}$
$ \Delta x $ (CMX)	$< 10 \text{ cm}$
number of stereo SL hits	> 2
number of axial SL hits	> 3
Impact parameter d_0	$< 0.3 \text{ cm}$
z-vertex match	$< 5 \text{ cm}$
$ z_0 $	$< 60 \text{ cm}$
I_{so}	< 0.1
Remove cosmic rays	back-to-back, timing

Table 3.3: Central muon selection cuts.

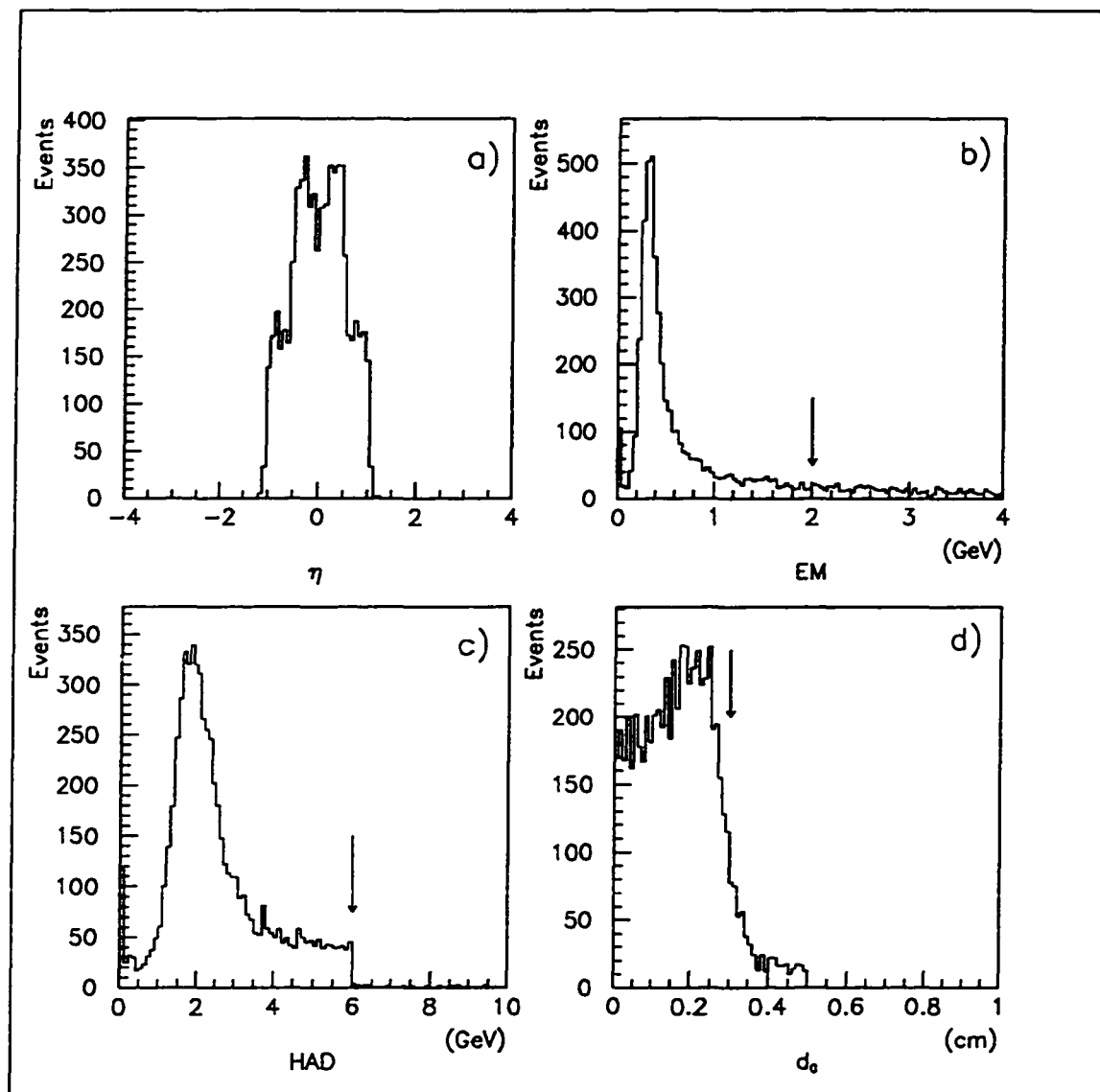


Figure 3.3: Pseudorapidity distribution and quality variables of central muons. (a) pseudorapidity, (b) energy deposited in the electromagnetic calorimeter, (c) energy deposited in the hadronic calorimeter, and (d) distance between the muon track and beam line. Also shown are cutoffs used in the central muon selection.

The P_T cut is actually applied to the beam-constrained momentum. By default, the P_T fitting program only uses the hit positions in the CTC system. However, better resolution can be achieved by including the position of the interaction vertex as a “hit” on the track, and refitting the track road. We know that the interaction vertex is somewhere within the beam spot, which is a Gaussian distribution with well-measured mean and width. This procedure is called beam constraint. Also one can get even better results by adding information from the SVX. But I do not intend to go that far as this analysis is merely a counting experiment, not a precision measurement.

Finally, there is a special muon category called the central minimum ionizing (CMIO) muons. These are the muons found in the region $|\eta| < 1.2$ not covered by muon chambers, but where tracking information is still available. The selection cuts of CMIO muons are identical to those listed in Table 3.3 except that the Δx cut is not used. In addition, they are required to pass fiducial cuts to avoid the chimney and cracks at the central calorimeters. The contribution of CMIO muons to the total detection efficiency is very small, largely due to the small angular coverage, and the fact that they do not cause triggers.

Again, $Z \rightarrow \mu^+ \mu^-$ data samples, with one muon passing all cuts and a second object in the muon data bank, are used to get the muon selection efficiency. The efficiency is found to be 92.3 % for CMU muons, 95.2 % for CMX muons and 92.5 % for CMIO muons[13, 14]. Figure 3.3 shows some of the muon distributions.

3.4 Forward Muons

3.4.1 Triggers

Muons detected in the forward muon (FMU) detector are called forward muons. The forward muon trigger first searches for six-hit allowed patterns in the drift chambers, as discussed in detail in Chapter 2. Then a coincidence is required for PADs and scintillator counters in the same octant where a six-hit pattern has been located and validated. And finally, forward muons with $P_T > 15$ GeV/c are selected by the triggering algorithm.

3.4.2 Selection Cuts

The FMU system covers $2.0 < |\eta| < 2.8$. Therefore, no CTC information is available for forward muon selection. The other disadvantage is that this pseudorapidity region is covered by either plug or forward calorimeter which has very poor energy and position resolutions. As a result, most of forward muon selection cuts depend on the information provided by the FMU system itself:

- N_{cell} , the first cell for a six-hit pattern in the front drift chambers, should not be too close to the beam since inner cells usually have a very high occupancy due to beam radiations;
- χ^2 of track fitting, should be reasonable;

- EM + HAD, same as for central muons, except that the energy is deposited in the plug and forward calorimeters;
- Number of hits used in track fitting should not be too low in order to get a reliable track;
- The distance between the event vertex and the reconstructed track in the z direction, z -vertex match, same as for central muons;
- The interaction vertex z_0 , same as for central muons.

The calorimeter energy cut needs to be elaborated. Since the resolution of the plug and forward calorimeters is very poor, we just require that the total energy deposited in the calorimeters meet a minimal requirement. No isolation cuts are applied to forward muons due to the limited CTC coverage and poor calorimeter resolution. Table 3.4 lists all these selection cuts.

As before, we use $Z \rightarrow \mu^+\mu^-$ data samples to get the FMU muon selection efficiency. Here we select those Z events which have a good central muon and a FMU object in the FMU data bank. Then the FMU selection cuts are applied to the FMU object to obtain the selection efficiency. The efficiency is found to be 89.0 % [16]. Figure 3.4 shows some of the muon distributions.

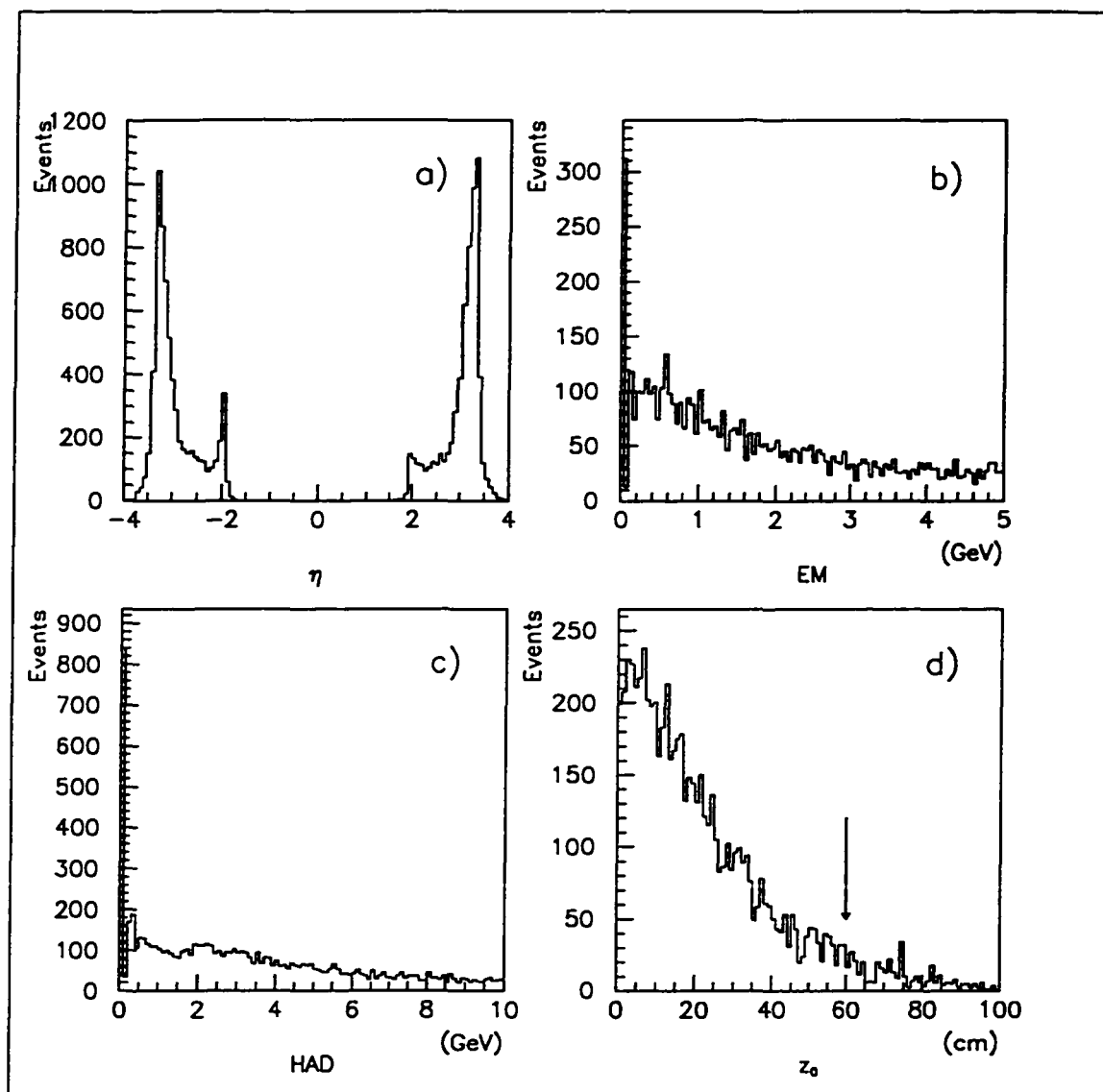


Figure 3.4: Pseudorapidity distribution and quality variables of forward muons. (a) pseudorapidity, (b) energy deposited in the electromagnetic calorimeter, (c) energy deposited in the hadronic calorimeter, and (d) interaction vertex. Also shown are cutoffs used in the forward muon selection.

Variable	Cut
P_T	$> 20 \text{ GeV}/c$
χ^2	> 10
Number of hits	$= 6$
N_{cell}	> 33
EM + HAD	$> 0.5 \text{ GeV}$
z-vertex match	$< 20 \text{ cm}$
$ z_0 $	$< 60 \text{ cm}$

Table 3.4: Forward muon selection cuts.

3.5 Jets

3.5.1 Triggers

The jet trigger first requires a single energy tower above thresholds (see the electron discussion earlier) in the region $|\eta| < 4.2$. Then the jet triggering algorithm seeks the highest energy tower ($E_T > 3 \text{ GeV}$) in the calorimeters as the seed tower. Then a jet cluster is formed within a cone of radius 0.4 in η - ϕ around the nominal jet direction. The cluster energy is calculated by summing up all continuous energy towers in both electromagnetic and hadronic calorimeters. Finally, four jet triggers are used with separate thresholds of 20, 50, 70, and 100 GeV on the transverse energy of the clusters.

3.5.2 Selection Cuts

The jet E_T obtained from jet triggering algorithm is called uncorrected jet E_T .

In this analysis, jets are selected with uncorrected jet $E_T > 10$ GeV and $|\eta| <$

2.4. This energy differs from its true parton value for a variety of reasons:

- The conversion from calorimeter pulse heights to nominal jet energy assumes a fixed proportional constant, which is obtained from test beam measurements of single pion response. On the other hand, the calorimeters exhibit a nonlinear response to low energy hadrons;
- The magnetic field in the CTC system bends low momentum charged particles outside the calorimeters or the clustering cone;
- Uneven calorimeter response at the calorimeter boundaries and cracks;
- Others physics, such as undetectable neutrinos and muons in the calorimeters, fragmentation, and underlying event.

Since it is impossible to completely map the detector response to different particles at different energy and fully understand the theoretical aspects of jets, jet energy is corrected for these known effects in an average way, with a very large uncertainty. The jet E_T increases about 30 % after corrections.

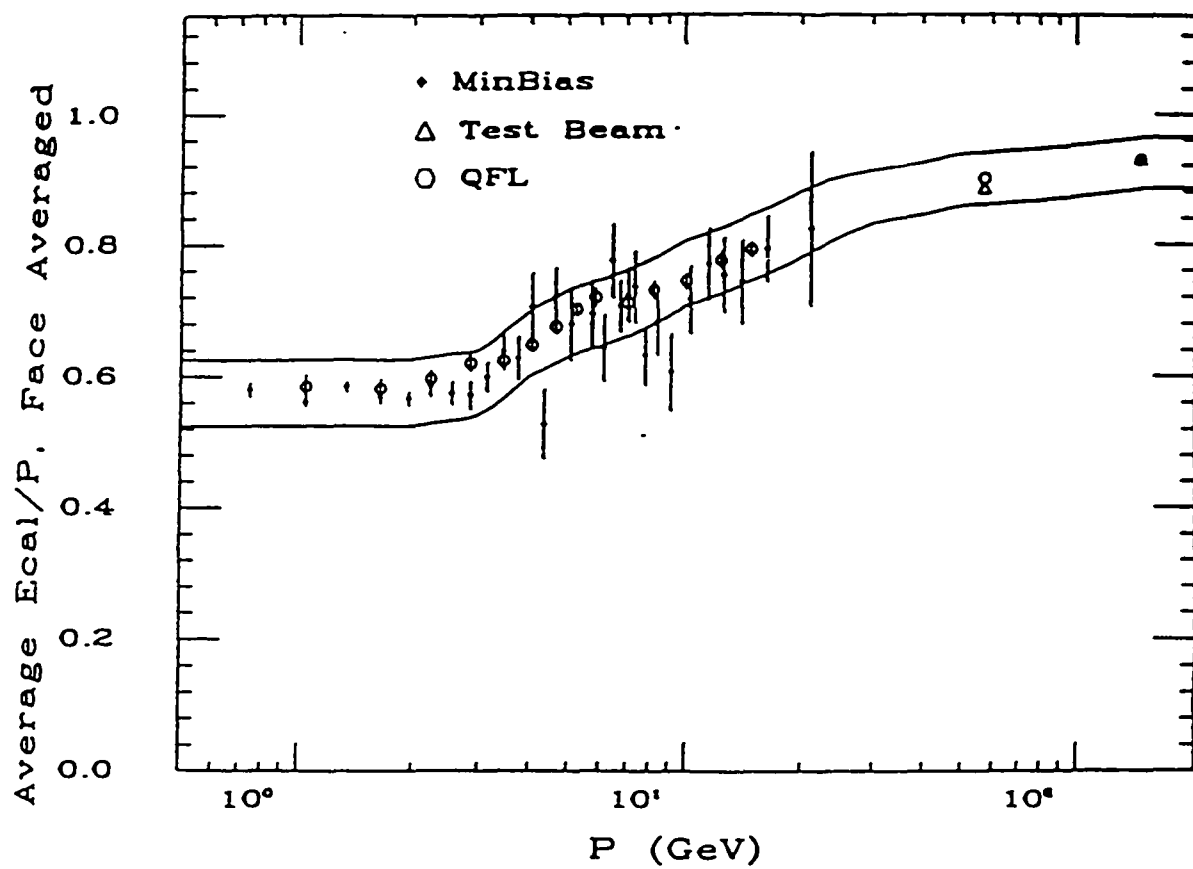


Figure 3.5: The central calorimeter response (E/p) to pions with momentum p .

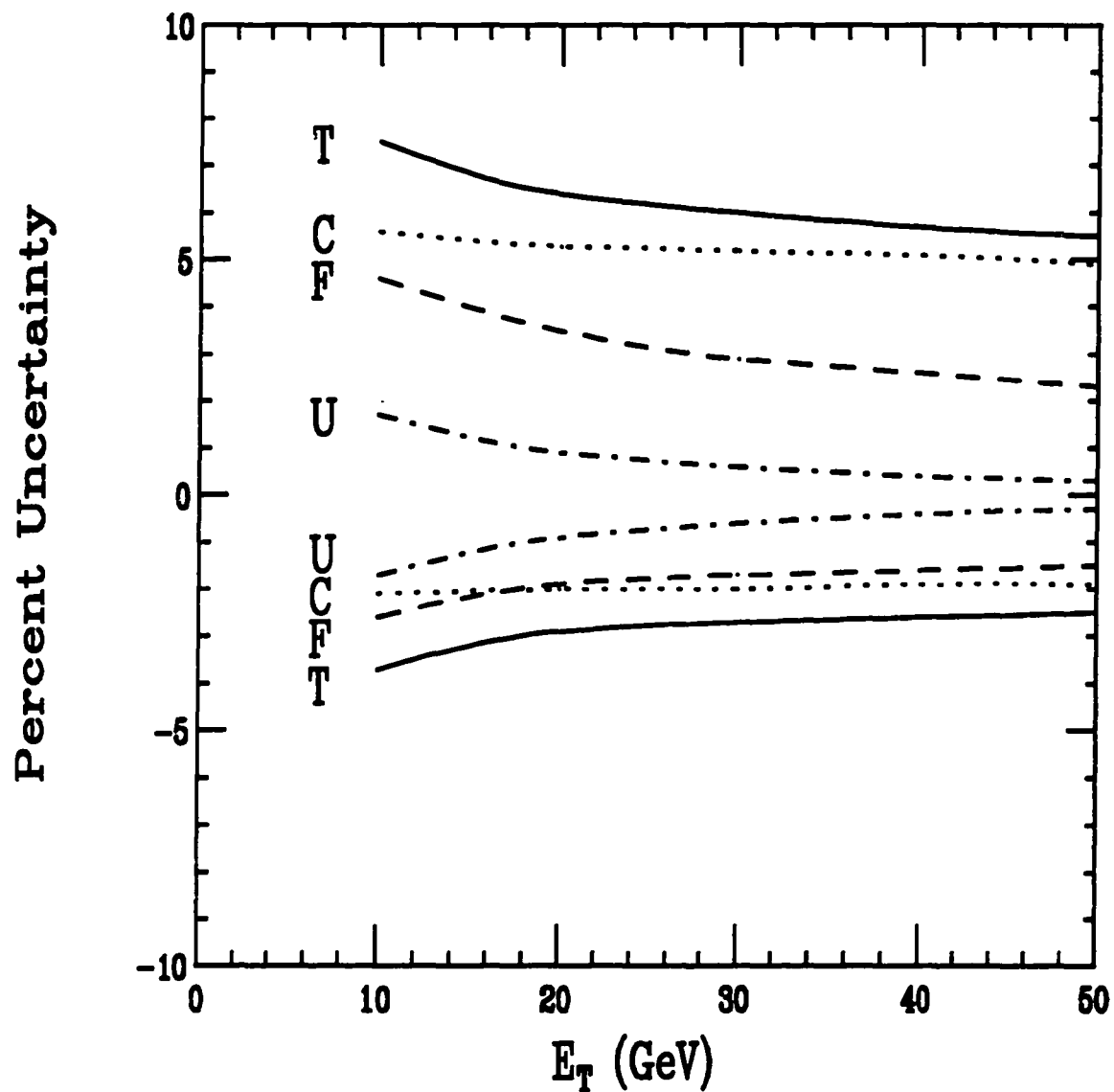


Figure 3.6: Total uncertainty (T) in the jet energy scale as a function of corrected jet E_T . The sources of uncertainty are the calorimeter response (C), fragmentation (F), and underlying event (U).

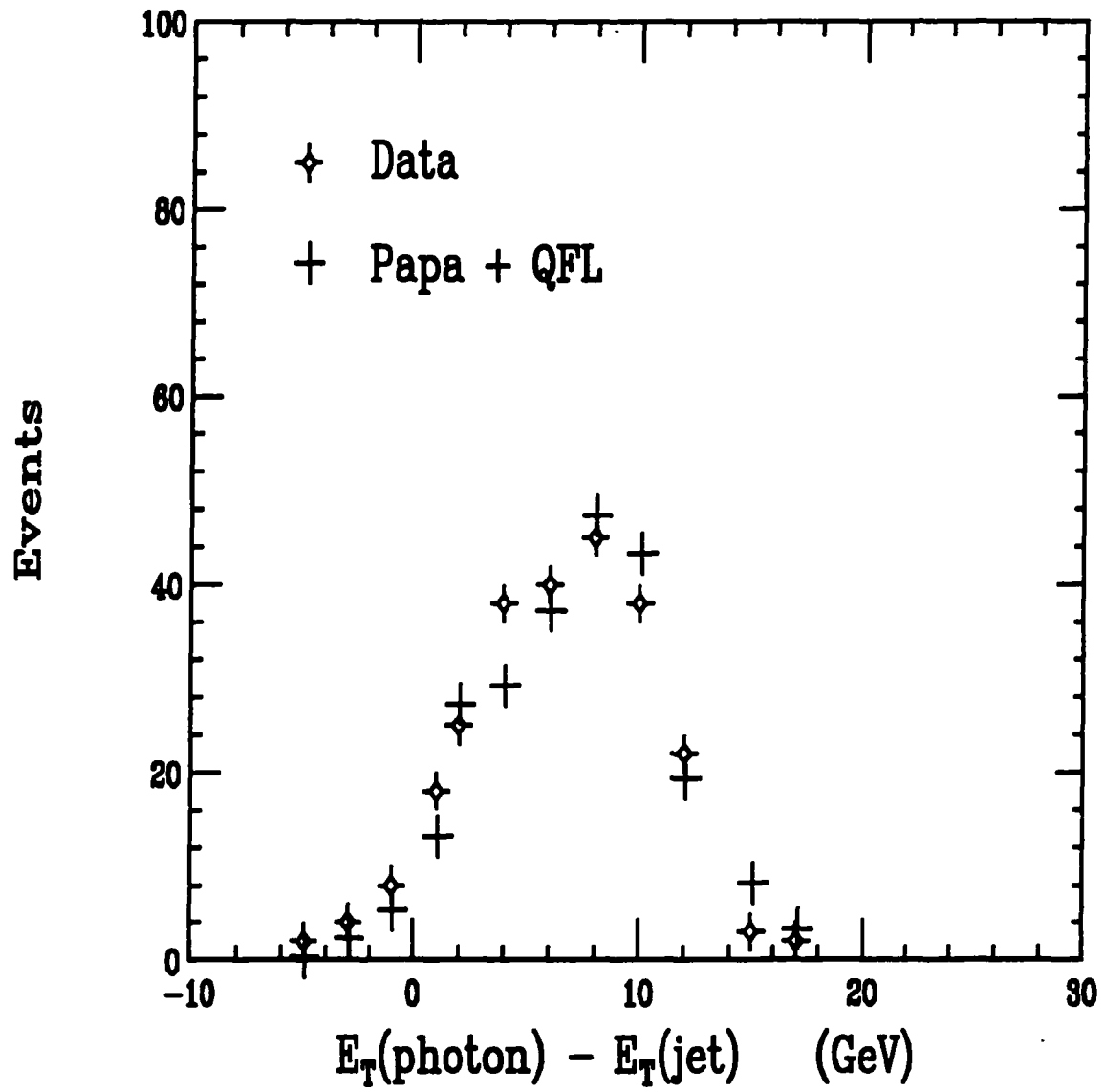


Figure 3.7: Unbalanced E_T in photon+jet events: data and PAPANENO+QFL simulations.

3.5.3 Energy Uncertainty

The dominant systematic uncertainty in the jet energy scale arises from the calorimeter response to incident hadrons. Figure 3.5 shows the central calorimeter response to incident pions[17]. The measurements come from test beams and minimum-bias events. The response is clearly nonlinear at low energy. The detector simulation QFL uses an averaged response to pions (see Figure 3.5), with a typical 5 % uncertainty. It simulates the calorimeter cracks in ϕ and η as well as the π/K ratio of jets. Finally, the QFL simulation of jets is tuned in such way that it gives the correct inclusive jet distribution[18]. The total uncertainty is plotted in Figure 3.6 as a function of corrected jet E_T by combining all uncertainties in quadrature. Here uncertainties come from the calorimeter response, fragmentation, and underlying event[19]. There is an additional theoretical uncertainty which arises from our modeling of gluon radiation in Monte Carlo programs. Studies on Z +jets and photon+jets show that this uncertainty can be controlled under 5 % [20]. In this analysis the combined uncertainty is taken as 10 % [21], which is somewhat conservative.

The uncertainty in the jet energy scale can also be estimated from studies of transverse energy balance in photon+jet and electron+jet processes. To estimate this uncertainty, one uses the fact that the imbalance of transverse energy is caused by mismeasurements of jet energy. The uncertainty obtained from this method is usually smaller than 10 %. The balancing technique, however, intro-

duces some new ambiguities such as soft gluons that are undetectable. Figure 3.7 shows the unbalanced E_T in photon+jet events[22]. Here for comparison, PAPAGENO+QFL programs are used to generate photon+jet events. Note that QFL reasonably reproduces the calorimeter resolution. The uncertainty obtained in this way, however, is smeared by, among other things, misidentified photons. For instance, π^0 associated with jets often fakes photons in the photon+jet data sample.

3.6 Missing Transverse Energy

Missing transverse energy \cancel{E}_T , coming from undetectable neutrinos and other sources, is defined as the negative of the vector sum of transverse energy in all energy towers

$$\vec{\cancel{E}}_T(\text{raw}) = - \sum \vec{E}_T, \quad (3.2)$$

where the sum is over all the calorimeters with $|\eta| < 3.6$. The tower threshold ranges from 100 MeV in the central region to 800 MeV in the forward region. The \cancel{E}_T resolution is found to be $0.7\sqrt{\sum E_T}$ (E_T in GeV), where \sum is the scalar sum of the transverse energy.

The raw \cancel{E}_T obtained in this way must be corrected in several cases. First, muons only leave a minimum ionizing energy in the calorimeters. So when there is a muon candidate, the \cancel{E}_T is corrected by adding the muon energy deposited in the calorimeters and subtracting the muon momentum measured in the tracking

system

$$\vec{E}_T(\text{corrected}) = \vec{E}_T(\text{raw}) + \vec{E}(\text{muon}) - \vec{P}(\text{muon}). \quad (3.3)$$

Second, for events with jets, the \cancel{E}_T should be calculated using the corrected jet E_T . In Eq. 3.2, on the other hand, the E_T is summed over uncorrected jet E_T . Therefore, the difference between corrected and uncorrected jet energy should be taken into account. In this analysis, however, I apply a jet veto to the event selection—rejecting any event with jets (see Chapter 4). So this correction to \cancel{E}_T becomes unnecessary. Finally, since the calorimeter response to single leptons is linear, and fiducial cuts are imposed on leptons, the correction of lepton E_T is very small. As a result, its effect on \cancel{E}_T is negligible.

Other factors also contribute to \cancel{E}_T . For instance, if leptons or jets fall into those regions not covered by the detector, one may find a large \cancel{E}_T which does not come from neutrinos. This “fake” \cancel{E}_T is often found in Z events, which is one of the main reasons why the Drell-Yan process is the biggest background to W^+W^- search.

Two neutrinos from $W^+W^- \rightarrow l^+l^-\nu\bar{\nu}$ give a very large \cancel{E}_T as shown in Figure 3.8. This provides an opportunity to suppress those backgrounds to W^+W^- where no or little \cancel{E}_T is expected, while still keep most of WW candidates intact. In this analysis, \cancel{E}_T is required to be $\cancel{E}_T > 25$ GeV.

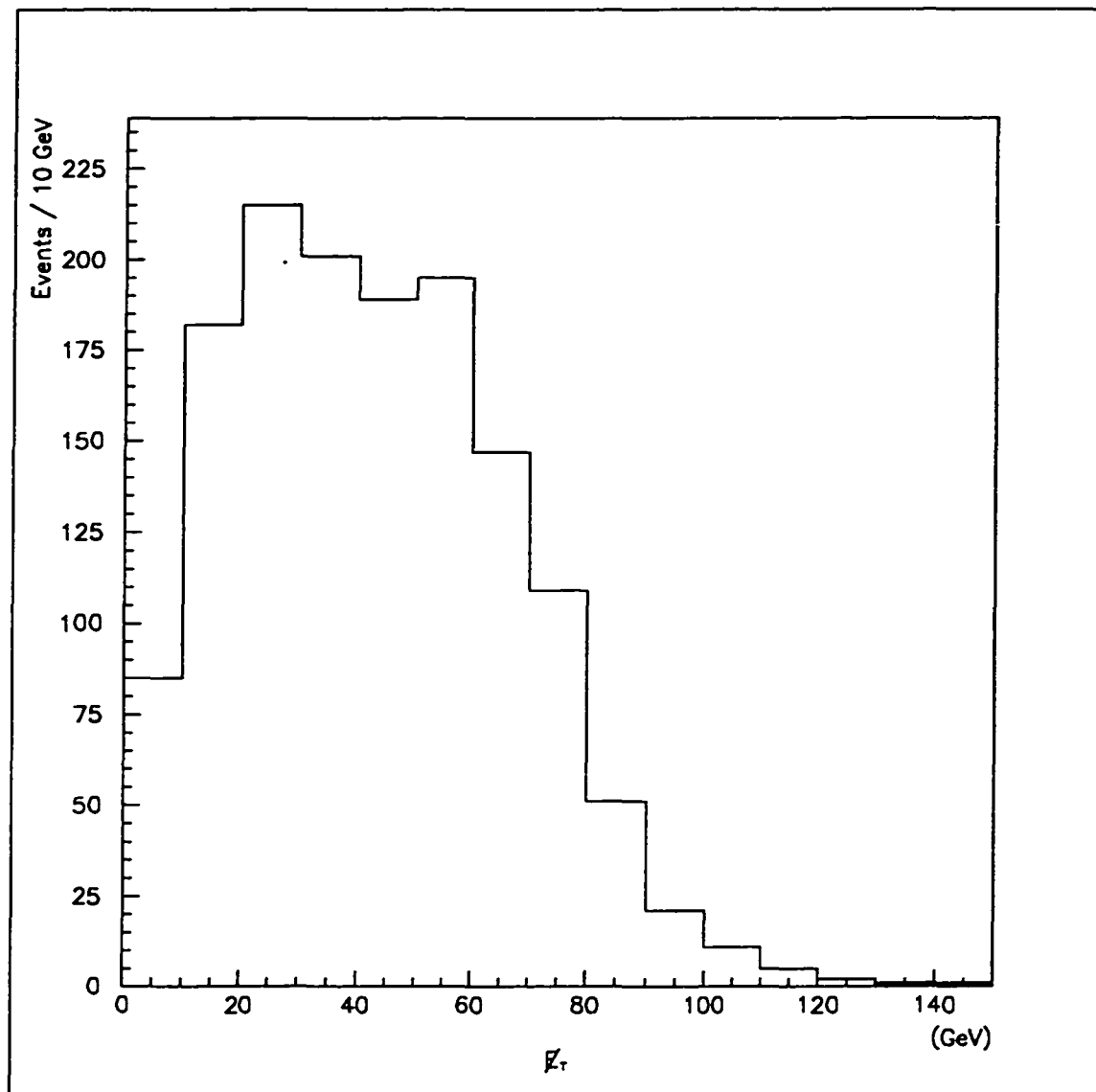


Figure 3.8: \cancel{E}_T distribution in $W^+W^- \rightarrow l^+l^-\nu\bar{\nu}$ from ISAJET simulations.

Chapter 4

Acceptance and Background

In this chapter I will present the W^+W^- acceptance calculation and event selection criteria. The background estimate, one important aspect of W^+W^- search, is also discussed.

4.1 Acceptance

In this section, I will analyze all factors in the W^+W^- detection efficiency: detector coverage, lepton selection, trigger path, and special cuts designed to either enhance W^+W^- signals or reduce the background to W^+W^- . Among them one interesting, yet very challenging issue is the jet veto, which is designed to reduce the top background. This cut will be discussed in great detail at the end of this section.

4.1.1 Dilepton Classification

In the channel $W^+W^- \rightarrow l^+l^-\nu\bar{\nu}$, dileptons are classified into 10 categories, depending on where they are detected in the CDF detector (Table 4.1). Note that those muons outside the coverage of muon chambers only have minimum ionizing tracks in the calorimeters, and therefore do not cause triggers. This is the reason why there is no MI-MI category. In the dimuon channel, at least one muon is required to be CMU.AND.CMP (see the muon selection description in Chapter 3 for this trigger) to minimize fake muons from jets, which is one of the main backgrounds to W^+W^- search.

4.1.2 Detection Efficiency

ISAJET version V6_43 Monte Carlo [23] is used to generate W^+W^- events, and the output is fed to the fast CDF detector simulation QFL. For comparison, PYTHIA[24] and a Monte Carlo program written by Tao Han[25] (denoted as TAOHAN thereafter) are also used. They agree with each other within 3 % except jet multiplicity which will be discussed later.

Given the number of $W^+W^- \rightarrow l^+l^-\nu\bar{\nu}$ events generated through Monte Carlo programs, the detection efficiency is defined as the fraction of these events detectable at the CDF detector. It can be decomposed into several factors:

$$\epsilon_{total} = \sum_{class} \epsilon_{geom.P_T} \epsilon_{ID} \epsilon_{Isol} \epsilon_{event} \epsilon_{0-jet} \epsilon_{trigger}. \quad (4.1)$$

Class	Origin
CE-CE	ee from CEM
CE-PE	ee from CEM and PEM
CE-MU	$e\mu$ from CEM and CMUO
CE-MI	$e\mu$ from CEM and CMIO
CE-FM	$e\mu$ from CEM and FMU
PE-MU	$e\mu$ from PEM and CMUO
PE-MI	$e\mu$ from PEM and CMIO
MU-MU	$\mu\mu$ from CMUO
MU-MI	$\mu\mu$ from CMUO and CMIO
MU-FM	$\mu\mu$ from CMUO and FMU

Table 4.1: Dilepton Classification. CEM and PEM denote the electromagnetic calorimeters in the central and plug regions, respectively. CMU, CMP and CMX are labeled with CMUO, while CMIO refers to a minimum ionizing track. FMU stands for the forward muon chambers.

The sum is over all the dilepton classes discussed earlier. The individual efficiencies in Eq. 4.1 will be discussed in the follows.

Geometry and Momentum

The acceptance due to geometrical and transverse momentum cuts, denoted by $\epsilon_{geom.P_T}$, is the fraction of W^+W^- events for which both leptons are inside the fiducial region and pass the P_T cut. This fraction is determined by running ISAJET Monte Carlo simulations. Figure 4.1 shows the pseudorapidity and transverse momentum distributions from $W^+W^- \rightarrow e\mu$ simulations.

Identification

The lepton identification efficiency, ϵ_{ID} , includes the combined effect of all lepton identification cuts. First, we use Z data samples to calculate the identification efficiency for single leptons, as briefly discussed in Chapter 3. Here a Z boson is defined as an e^+e^- ($\mu^+\mu^-$) pair with invariant mass between $75 \text{ GeV}/c^2$ and $105 \text{ GeV}/c^2$. The procedure is as follows: First select those $Z \rightarrow e^+e^-$ ($\mu^+\mu^-$) events with one central electron (muon) passing all cuts and a second object in the electron (muon) data bank. Then the electron (muon) identification cuts are applied to the second object in the data bank to obtain the identification efficiency for single leptons. Table 4.2 gives the single-lepton efficiencies[13, 14, 16]. For a given dilepton class, the dilepton identification efficiency ϵ_{ID} is the product

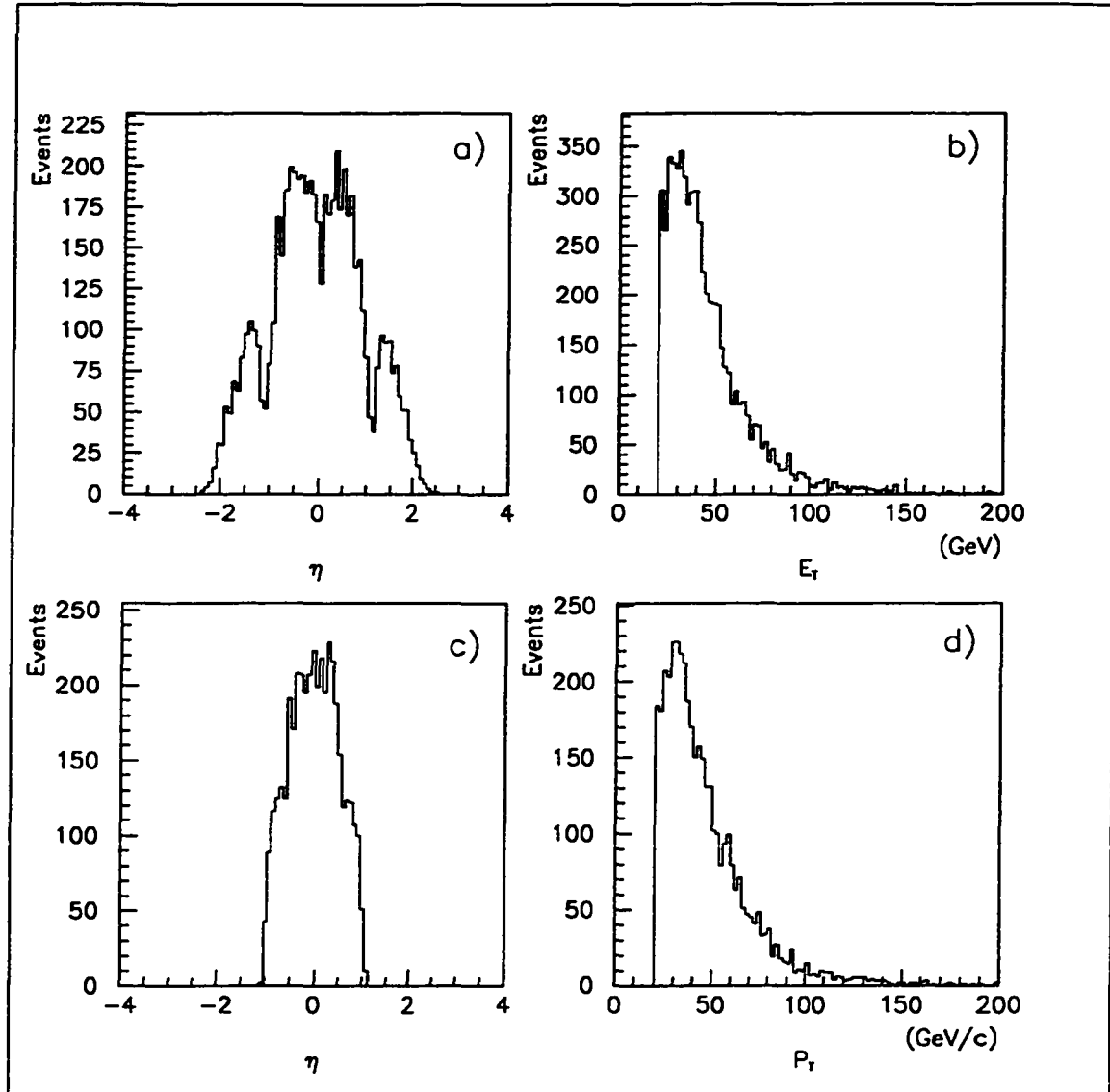


Figure 4.1: Pseudorapidity η and transverse energy E_T (momentum P_T) distributions from $W^+W^- \rightarrow e\mu$ simulations: (a) and (b) for electrons; (c) and (d) for muons.

Category	ID efficiency
CE	81.3 %
PE	85.7 %
CMU/CMP	92.3 %
CMX	95.2 %
MI	92.5 %
FM	89.0 %

Table 4.2: Single-lepton identification efficiencies.

of the single-lepton efficiencies corresponding to that class.

Isolation

To reduce backgrounds, all leptons are required to be well isolated—both calorimeter and track isolation cuts must be satisfied. The lepton calorimeter isolation is defined as the ratio of the transverse energy in the calorimeters within a cone of radius 0.4 in η - ϕ centered on the lepton but excluding the transverse energy of the lepton, to the transverse energy of the lepton. The lepton track isolation is defined as the ratio of P_T sum of CTC tracks within a cone of radius 0.4 but excluding the lepton track contribution, to the lepton momentum. The dilepton isolation efficiency, ϵ_{isol} , is obtained from Monte Carlo samples. No isolation cut is imposed on FMU muons since the plug and forward calorimeters have very poor energy and position resolutions, and no CTC information is avail-

able in the FMU region. The isolation distributions are shown in Figures 4.2 and 4.3.

Event

To discriminate against the backgrounds from $Z \rightarrow \tau\tau$ and the Drell-Yan process, events are required to have a minimal missing transverse energy \cancel{E}_T exceeding 25 GeV. Here \cancel{E}_T is corrected for muons, but no correction is made for jets since any event with jet activity is rejected. To further reduce these backgrounds, we reject events where \cancel{E}_T points along the direction of one of the leptons[21]: We require $\Delta\phi(\vec{\cancel{E}}_T, \text{lepton}) > 20^\circ$ for those events with $\cancel{E}_T < 50$ GeV, where $\Delta\phi$ is the azimuthal angle between the direction of \cancel{E}_T and the direction of the nearest lepton. Also in the e^+e^- ($\mu^+\mu^-$) channel, we remove events with $75 \text{ GeV}/c^2 < M_{l^+l^-} < 105 \text{ GeV}/c^2$. This cut, together with the \cancel{E}_T cuts, will effectively reduce the Drell-Yan background. Finally, dileptons are required to have opposite charges to satisfy the charge conservation in the channel $W^+W^- \rightarrow l^+l^-\nu\bar{\nu}$. The efficiency of these cuts is denoted by ϵ_{event} .

The dimuon channel is complicated by cosmic rays. Although muons are selected through an online cosmic filter, there are still small number of cosmic rays in the muon data sample with high \cancel{E}_T and small $\Delta\phi$. To remove these cosmic rays, we reject all dimuon events with $\Delta\phi(\vec{\cancel{E}}_T, \text{lepton}) < 20^\circ$. Recall that we impose this cut only if $\cancel{E}_T < 50$ GeV in the ee and e μ channels. As a result, the dimuon detection efficiency is reduced by about 2 %.

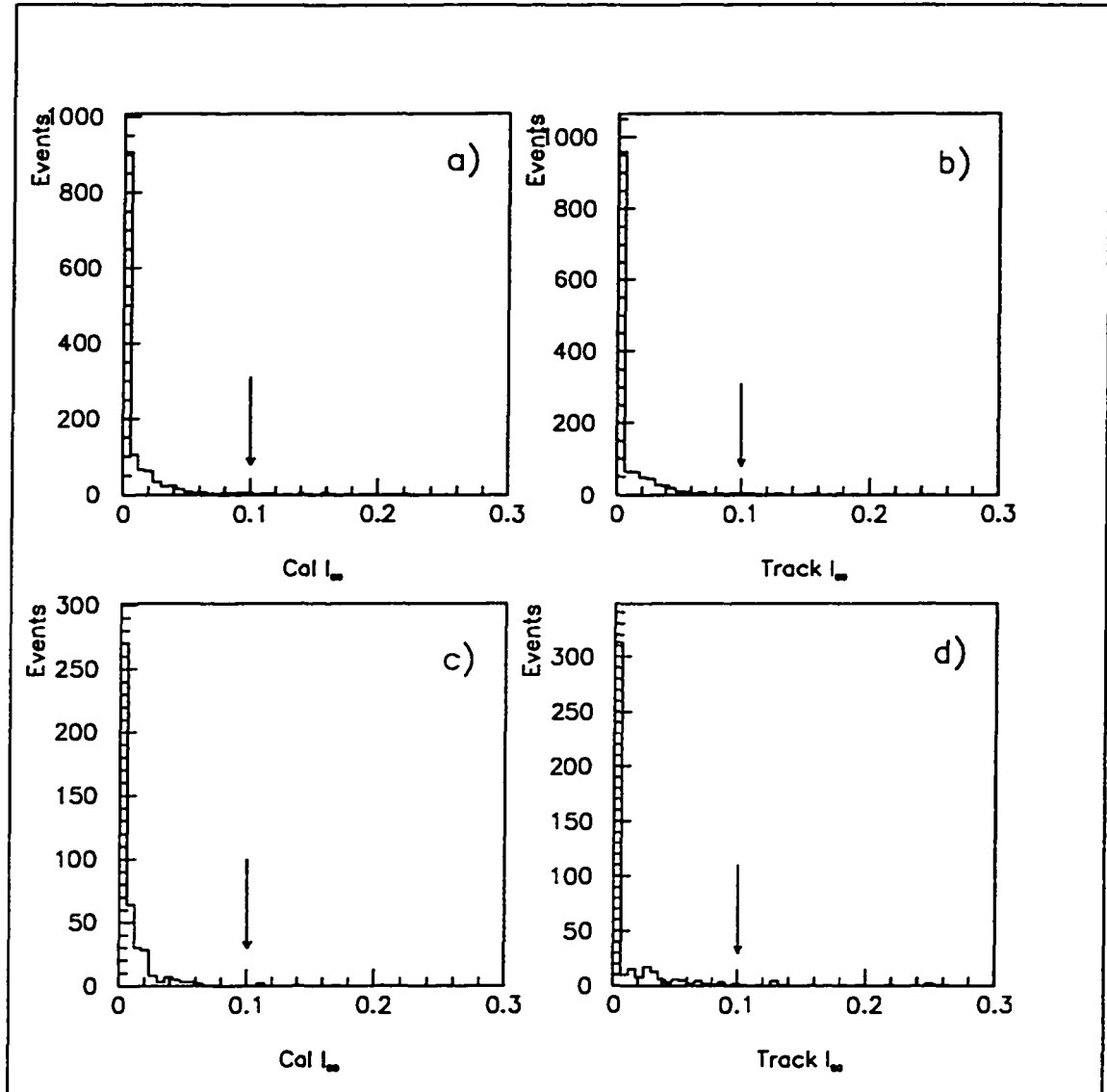


Figure 4.2: Electron isolation distributions from W^+W^- simulations: calorimeter isolation (a) and track isolation (b) for central electrons; calorimeter isolation (c) and track isolation (d) for plug electrons.

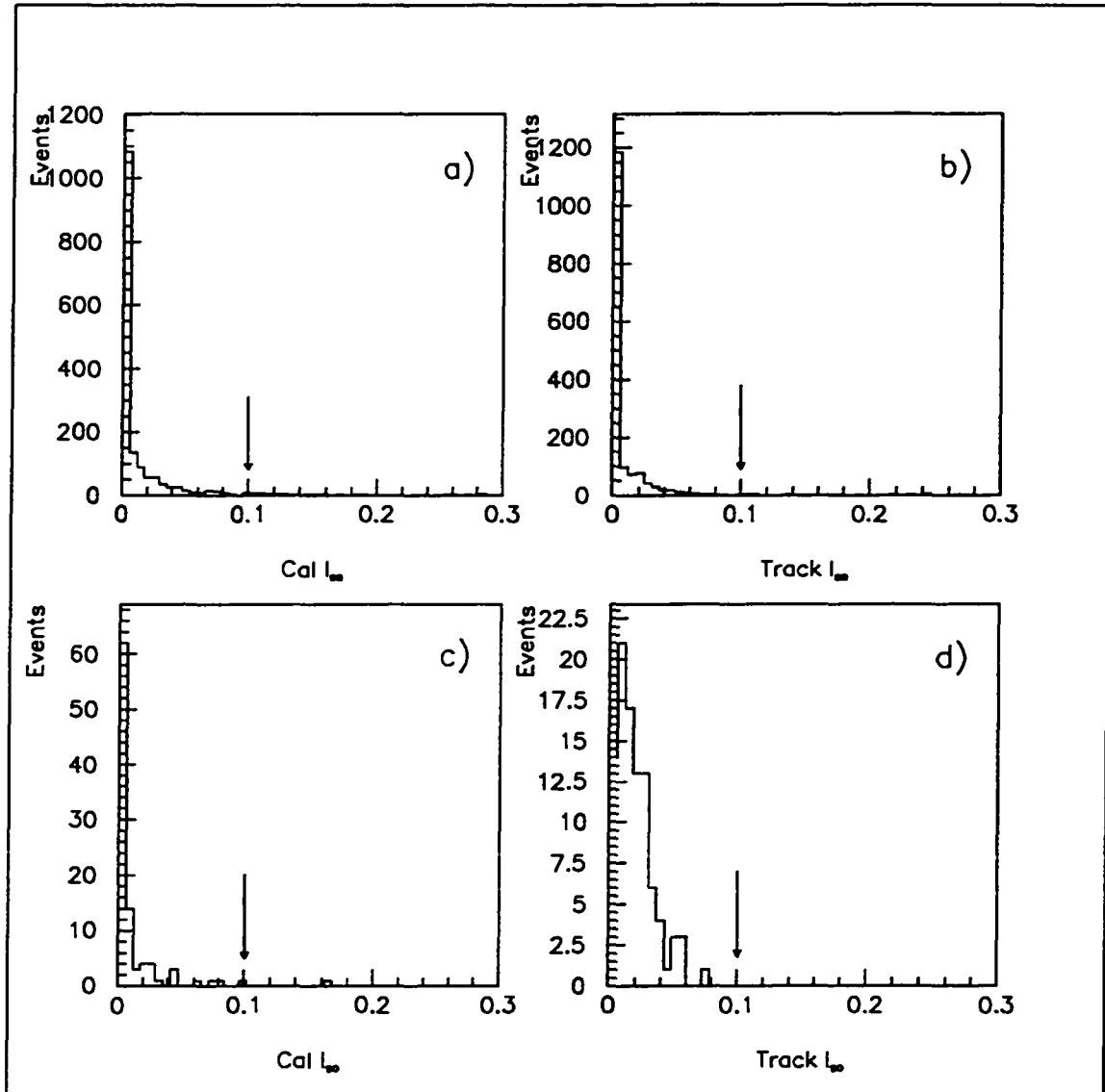


Figure 4.3: Muon isolation distributions from W^+W^- simulations: calorimeter isolation (a) and track isolation (b) for central muons; calorimeter isolation (c) and track isolation (d) for minimum ionizing tracks.

Trigger

The trigger efficiency $\epsilon_{trigger}$ is determined from data samples by using events which satisfy multiple triggers. Prescale and CFT effects for 1B data have been taken into account.

- The central electron trigger efficiency was very stable during 1A and early 1B ($\epsilon_{CEM} = 90.3\%$, see [26]). Later it was revealed that the tracking efficiency decreased from 98.0% to 93.4%, which was attributed to the CTC aging effect[27] (after Run 60972, with an integrated luminosity $\sim 80 pb^{-1}$). I use 95.0% as the average CFT efficiency over this period. So the central electron trigger efficiency, proportional to the tracking efficiency, is corrected to

$$90.3\% \times \frac{95.0\%}{98.0\%} = 87.5\%$$

for 1B data.

- The trigger efficiency calculation for central muons is complicated by trigger configurations, prescales, and dead channels during the run. No prescale was applied to muon triggers during Run 1A. So we don't need to calculate separately CMU.AND.CMP and CMU-ONLY trigger efficiencies. It is found

$$\epsilon_{CMU.AND.CMP} = \epsilon_{CMU-ONLY} = 86.1\%$$

for 1A data[28, 29]. The CMX system was only partially functioning during Run 1A and there were a series of changes to trigger configurations, so CMX muons from Run 1A are not included in this analysis. For 1B data after Run 60972, the average luminosity was very high. As a result, both CMU-ONLY and CMX triggers were prescaled. A careful analysis found[30] $\epsilon_{CMU-ONLY} = 87.1\%$ and $\epsilon_{CMX} = 70.0\%$ before Run 60972, $\epsilon_{CMU-ONLY} = 47.0\%$ and $\epsilon_{CMX} = 37.9\%$ after Run 60972. Prescale factors have been included in the efficiencies cited here. The efficiency $\epsilon_{CMU.AND.CMP}$ remained essentially unchanged during the whole run.

- The trigger efficiency of forward muons is obtained from those CMU-FMU Z events which were collected by CMU triggers. The efficiency is found to be 71.0 %, see [16].
- The trigger efficiency of plug electrons strongly depends on electron E_T : $\epsilon_{PEM} \sim 10\%$ at $E_T = 20$ GeV, and $\epsilon_{PEM} \sim 90\%$ at $E_T = 30$ GeV. Fitting 1A data yields

$$\epsilon_{PEM}(E_T) = \frac{1 + 45017}{\exp(251.0/E_T) + 45017},$$

where the difference between east and west plugs is found negligible[31]. There is no CFT requirement in the plug electron trigger, so I assume that this efficiency function still holds for 1B data. The plug electron trigger efficiency is obtained by convoluting this efficiency function with the E_T

spectrum from W^+W^- simulations. The average trigger efficiency is found to be 81.0 %.

Unlike single-lepton analyses, dilepton search is very insensitive to any particular trigger efficiency, mainly due to the fact that we have two lepton triggers in the dilepton search, and if one of them changes, the total trigger efficiency just changes slightly. For example, the CMX and CMU-ONLY prescale in 1B (roughly 1.5) only causes about a 1 % drop in the detection efficiency. To demonstrate the insensitivity of $\epsilon_{trigger}$ to a particular trigger efficiency, let's take the CEM-MU channel as an example. The contribution of the channel CEM and CMU-ONLY to the total CEM-MU trigger efficiency is given by

$$0.15[1 - (1 - \epsilon_{CEM})(1 - \epsilon_{CMU-ONLY})],$$

where 0.15 is the weight of the channel CEM and CMU-ONLY relative to the whole CEM-MU channel, and $\epsilon_{CEM} \sim 90\%$. So the total trigger efficiency is reduced to

$$0.015\Delta\epsilon_{CMU-ONLY}$$

if $\Delta\epsilon_{CMU-ONLY}$ is the change of CMU-ONLY trigger efficiency. It drops only about 1% even $\epsilon_{CMU-ONLY}$ decreases 50 %!

Jet Veto

The top quark production cross section is of the same order as the W^+W^- production cross section, so $t\bar{t}$ production is one of the main backgrounds to

W^+W^- search. In the top quark dilepton channel $t\bar{t} \rightarrow W^+W^-b\bar{b}$, top quarks decay into W bosons and b quarks, with b quarks hadronized into jets with large E_T (see the background discussion for detail). A jet veto is imposed to discriminate against the top background: We remove events with any jet with uncorrected transverse energy exceeding 10 GeV. This 0-jet cut efficiency is very complicated so I will discuss in great detail how this efficiency is estimated .

ISAJET+QFL simulations indicate $\epsilon_{0-jet} = 58\%$ in the channel $W^+W^- \rightarrow l^+l^-\nu\bar{\nu}$. Here ϵ_{0-jet} is the 0-jet fraction of W^+W^- events. The QCD correction procedure in ISAJET is as follows: The leading order QCD correction is based on the matrix element calculation, and higher order QCD corrections are reduced to a classical cascade process. ISAJET modeling of QCD radiation is essentially yet confirmed. For example, ISAJET predicts $\epsilon_{0-jet} = 71\%$ in the Z production. On the other hand, CDF measurements show that this efficiency is about 79%, see [32, 33]. Clearly, ISAJET overestimates the jet activity. This gives us a clue that $\epsilon_{0-jet} = 58\%$ in the W^+W^- production from ISAJET might be too low.

TAOHAN is based on the matrix element calculation up to two jets, and it gives $\epsilon_{0-jet} = 69\%$ in the W^+W^- production. PYTHIA, with emphasis on high P_T physics, predicts $\epsilon_{0-jet} = 76\%$. Table 4.3 summarizes all results from these three Monte Carlo programs.

As far as jet multiplicity concerned, W^+W^- production resembles the Drell-Yan process in the sense that jets mainly come from the initial-state radiation. However, the similarity only goes this far. The invariant mass in the Z production

Monte Carlo	ϵ_{0-jet}	ϵ_{1-jet}	ϵ_{2-jet}
ISAJET	58	29	13
PYTHIA	76	20	4
TAOHAN	69	26	5

Table 4.3: Jet multiplicity of W^+W^- production from various W^+W^- Monte Carlo simulations.

is $91 \text{ GeV}/c^2$, while in the W^+W^- production it would increase up to about $240 \text{ GeV}/c^2$ (see Figures 4.4 and 4.5). So we expect to see more jets in the W^+W^- production, although by how much is still an open question.

One method of estimating ϵ_{0-jet} is as follows: If M_Z is changed to $240 \text{ GeV}/c^2$ in the $Z \rightarrow l^+l^-$ Monte Carlo simulation, we expect that the jet multiplicity in $Z \rightarrow l^+l^-$ will be close to that of W^+W^- production. Following this approach, we estimate the jet multiplicity in the W^+W^- production by

$$\begin{aligned}
\epsilon_{n-jet}(WW) &= \frac{\epsilon_{n-jet}(WW) \epsilon_{n-jet}(2.7M_Z)}{\epsilon_{n-jet}(2.7M_Z) \epsilon_{n-jet}(M_Z)} \epsilon_{n-jet}(M_Z) \\
&\equiv \alpha_n \beta_n \epsilon_{n-jet}(M_Z).
\end{aligned} \tag{4.2}$$

In this approach, the Drell-Yan process is used as a “bridge” to estimate the jet activity in the W^+W^- production, largely because the Drell-Yan process is well understood. Here $\epsilon_{n-jet}(WW)$ is the n-jet fraction for W^+W^- production, $\epsilon_{n-jet}(M_Z)$ and $\epsilon_{n-jet}(2.7M_Z)$ are the n-jet fractions for the Drell-Yan process at $M_Z = 91 \text{ GeV}/c^2$ and $240 \text{ GeV}/c^2$ ($2.7M_Z$), respectively. The two ratios α_n and

β_n are obtained from Monte Carlo simulations, and experimental measurements of $\epsilon_{n-jet}(M_Z)$ are used as input[32, 33].

First, QTW = 0 in ISAJET is used to calculate these parameters, where QTW is the transverse momentum transfer. This choice is the default of ISAJET: After a primary hard scattering is generated, QCD radiative corrections are added based on the low P_T approximation. Then QTW \neq 0 in ISAJET is also tested. This option starts with W^+W^- +gluon diagrams. Therefore, it is primarily used for studies of QCD radiative corrections. According to the author, “It represents the standard QCD answer for any QTW above 10–20 GeV. Thus one should use it, e.g., to calculate backgrounds for a heavy top quark decaying via $t \rightarrow W + b$.” However, there is a problem associated with this choice. Since this option starts with W^+W^- +gluon diagrams, there are no 0-jet events. Therefore the generated events cannot be normalized. The ratios cited for this option are obtained in the following way: When increasing the Z mass, we keep all other parameters in the generator unchanged. Count how many events that pass the W^+W^- selection cuts in both cases, and then take the ratio of the number of events passed. Finally, VECBOS[34] $Z \rightarrow l^+l^-$ simulations are also used to obtain the parameter β_n (Table 4.5), with the choice of $Q^2 = M_Z^2$.

All these results are summarized in Table 4.6. It should be pointed out that we only use this approach (Eq. 4.2) for ISAJET-related results (the first three rows in Table 4.6). The theoretical result (denoted by BHZO) is calculated at the parton level[4] with $P_T(\text{jet}) \geq 15$ GeV/c and $|\eta(\text{jet})| \leq 2.5$. We take ϵ_{0-jet}

Monte Carlo	Process	ϵ_{0-jet}	ϵ_{1-jet}	ϵ_{2-jet}
ISAJET	WW	58	29	13
	Z with $M_Z = 240 \text{ GeV}/c^2$	59	24	17
	α_n		1.21	0.76

Table 4.4: Jet multiplicity of W^+W^- and Z ($M_Z = 240 \text{ GeV}/c^2$) productions from ISAJET Monte Carlo simulations. Note that QTW = 0 (default) is used for ISAJET generator. Here α_n is obtained by taking the ratio of $\epsilon_{n-jet}(WW)$ to $\epsilon_{n-jet}(2.7M_Z)$.

= 68% in the W^+W^- analysis and assign 10% uncertainty to it.

4.1.3 Uncertainties

Tables 4.7 and 4.8 list all the efficiencies. Typically 10K W^+W^- Monte Carlo events are generated and 1K events are left after all selection cuts. This leads to a 3 % statistical uncertainty for the total detection efficiency. We calculate $\epsilon_{geom.P_T}$ from ISAJET, PYTHIA, and TAOHAN, and they differ by less than 1 %. Based on Z data studies, the lepton identification efficiency is very stable and the uncertainty is about 2 %. The event cut efficiency changes about 4 %, depending on generators used. The total detection efficiency varies slightly (3 %) when different parton structure functions are tested. The 10 % uncertainty of jet energy scale affects jet multiplicity and the accuracy of \cancel{E}_T . A 4 % uncertainty is

Monte Carlo	Process	ϵ_{0-jet}	ϵ_{1-jet}	ϵ_{2-jet}
ISAJET	Z with $M_Z = 91 \text{ GeV}/c^2$	71	21	8
	Z with $M_Z = 240 \text{ GeV}/c^2$	59	24	17
	β_n		1.14	2.13
	β_n^*		1.47	1.76
VECBOS	Z with $M_Z = 91 \text{ GeV}/c^2$	74	22	4
	Z with $M_Z = 240 \text{ GeV}/c^2$	63	31	6
	β_n		1.41	1.50

Table 4.5: Jet multiplicity of Z production from ISAJET and VECBOS Monte Carlo simulations. Here β_n is obtained by taking the ratio of $\epsilon_{n-jet}(2.7M_Z)$ to $\epsilon_{n-jet}(M_Z)$. Note that QTW = 0 (default) is used in ISAJET simulations for β_n , while β_n^* is obtained with QTW \neq 0. See text for these options.

Monte Carlo	ϵ_{0-jet}	ϵ_{1-jet}	ϵ_{2-jet}
ISAJET(QTW=0)	72	22	6
ISAJET(QTW \neq 0)	67	28	5
ISAJET(QTW=0)+VECBOS	68	27	5
PYTHIA	76	20	4
TAOHAN	69	26	5
BHZO	70	25	5

Table 4.6: Jet multiplicity of W^+W^- production. See text for detail.

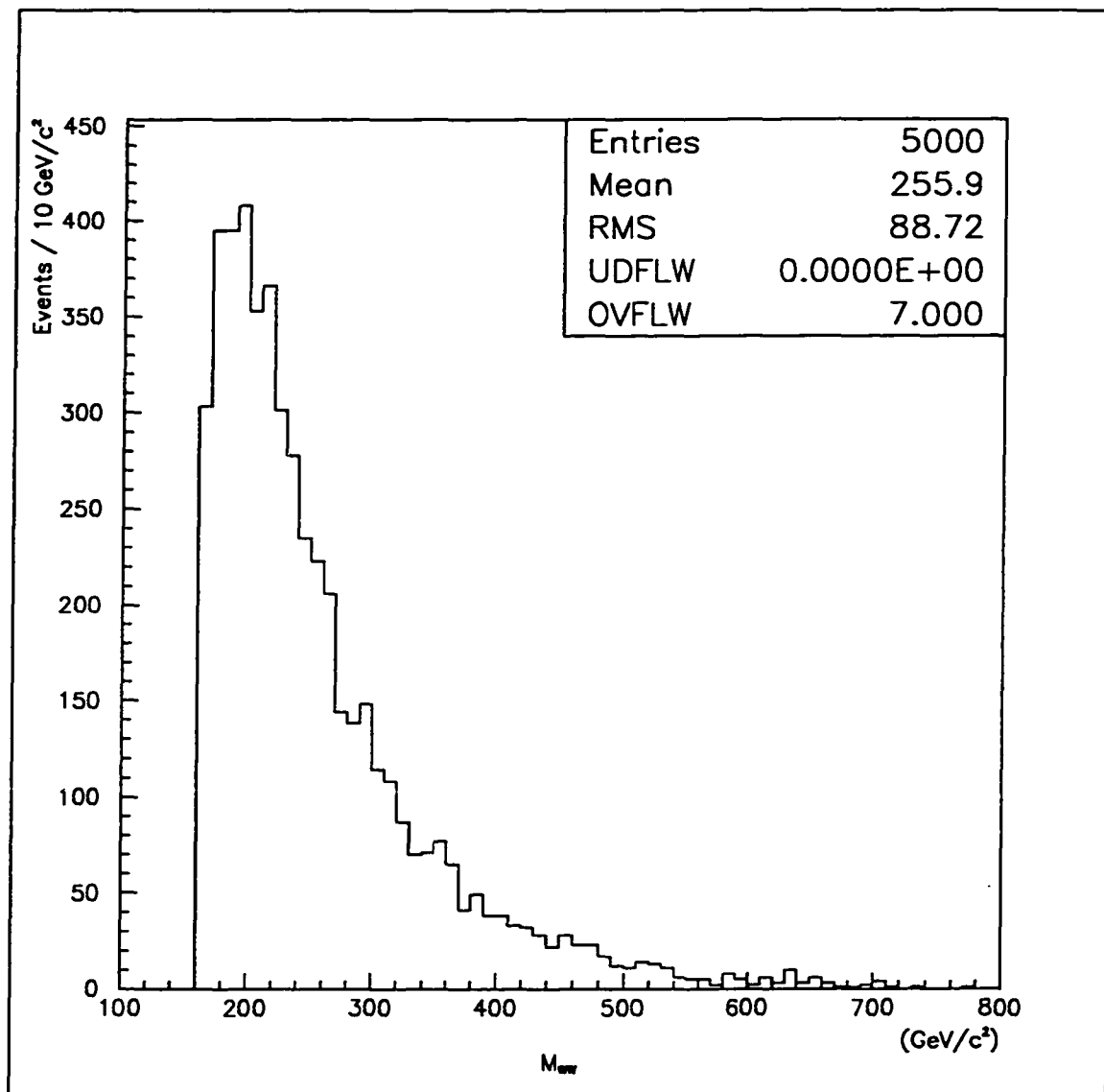


Figure 4.4: W^+W^- invariant mass from $\bar{p}p \rightarrow W^+W^-$ simulations (ISAJET).

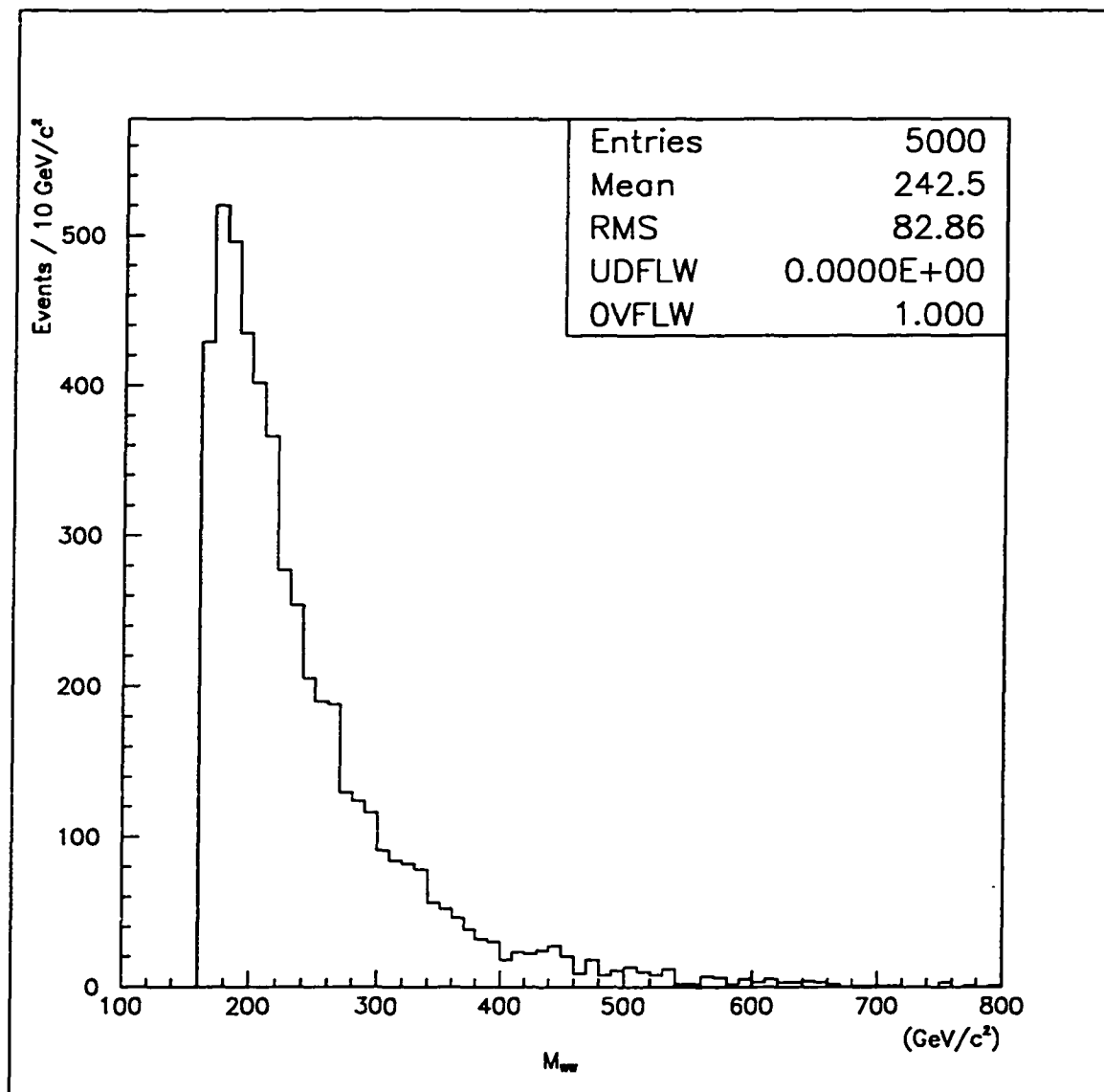


Figure 4.5: W^+W^- invariant mass from $\bar{p}p \rightarrow W^+W^-$ simulations (PYTHIA).

Class	$\epsilon_{geom.P_T}$	ϵ_{ID}	ϵ_{Isol}	ϵ_{event}	ϵ_{0-jet}	$\epsilon_{trigger}$	ϵ_{total}
CE-CE	20.4	66.1	93.3	55.0	68.0	98.6	4.64
CE-PE	9.6	69.7	91.9	54.1	68.0	97.8	0.24
CE-MU	21.4	75.6	89.0	72.1	68.0	95.0	6.70
CE-MI	2.0	75.2	89.4	75.4	68.0	88.2	0.60
CE-FM	3.6	72.4	90.4	73.3	68.0	96.6	1.13
PE-MU	4.8	79.8	86.9	67.1	68.0	92.3	1.40
PE-MI	0.6	79.3	87.1	73.6	68.0	81.0	0.16
MU-MU	15.2	86.1	90.0	56.3	68.0	92.8	4.16
MU-MI	4.8	85.4	88.1	58.9	68.0	86.1	1.24
MU-FM	1.6	82.1	88.5	54.1	68.0	96.0	0.41

Table 4.7: Dilepton detection efficiency.

found by changing jet energy within $\pm 10\%$. It has been demonstrated earlier that the dilepton search is very insensitive to trigger efficiencies, so the uncertainty of the trigger efficiency is ignored. The total uncertainty is the sum of these uncertainties (include the uncertainty from ϵ_{0-jet}) in quadrature.

Class	ee	$e\mu$	$\mu\mu$
ϵ_{total}	4.88	9.99	5.81

Table 4.8: Total dilepton detection efficiency.

4.2 Background

Background estimation is crucial to the analysis. It directly affects the accuracy of measurements such as the W^+W^- cross section and limits on vector boson anomalous couplings. There are a variety of sources which could mimic the W^+W^- signature: $t\bar{t} \rightarrow W^+W^-b\bar{b}$, the Drell-Yan process, $Z \rightarrow \tau\tau$, WZ production, and W+jets processes in which jets fake leptons. I use Monte Carlo programs, as well as data samples in some cases, to study these processes, applying the same selection criteria as for W^+W^- .

4.2.1 $t\bar{t}$

In the last two years, the CDF and D0 collaborations have independently confirmed the existence of top quarks. The mass and production cross section of top quarks have been measured. Based on these measurements, the top quark background to W^+W^- is estimated. Here the top quark mass and production cross section are taken as $170 \text{ GeV}/c^2$ and 5.8 pb , respectively. Monte Carlo studies (ISAJET and PYTHIA) show that, in the dilepton channel $t\bar{t} \rightarrow W^+W^-b\bar{b}$, only about 0.7 % of top events have no jet at all (Figure 4.6). A total of 5.0 dilepton events is expected before the jet veto[14]. So the top dilepton background is given by

$$5.0 \times 0.7\% = 0.04.$$

There are uncertainties from the top dilepton detection efficiency and top

production cross section (10 % each as cited in Ref. [21]). In the top quark production, jets mainly come from hadronized b quarks. Therefore, the uncertainty of the 0-jet efficiency should be smaller than that in the W^+W^- production. So we assign a conservative 10 % uncertainty due to the jet veto. Then the total uncertainty is 17 %.

4.2.2 $Z \rightarrow \tau\tau$

The background from $Z \rightarrow \tau\tau \rightarrow ee, \mu\mu$, or $e\mu$ is estimated by using CDF Z events in which the two leptons from Z are replaced with two τ 's which are then forced to decay into electrons or muons. First, a data sample generated in this way is used to calculate the event and jet cut efficiencies. We find $\epsilon_{event} = 1.43$ % in the ee channel, 1.55 % in the $\mu\mu$ channel, and 2.78 % in the $e\mu$ channel. The uncertainty of these efficiencies (25 % each) is dominated by limited statistics. The 0-jet cut efficiency is found to be 34 % in this sample, with 25 % statistical uncertainty.

Then ISAJET is used to simulate $Z \rightarrow \tau\tau$ in order to calculate other efficiencies. We find $\epsilon_{geom.PT.ID.Iso} = 1.03$ %, 0.79 %, and 1.02 % in the ee , $\mu\mu$, and $e\mu$ channels, respectively. Assuming $\sigma_{Z \rightarrow \tau\tau} = \sigma_{Z \rightarrow ee} = 230$ pb[32, 33], and using the branching ratio $Br(\tau\tau \rightarrow ee + X) = 0.0317$, one can readily estimate this background by

$$N_{expected} = \sigma_{Z \rightarrow \tau\tau} \sum_{class} \int \mathcal{L} dt Br \epsilon_{total}$$

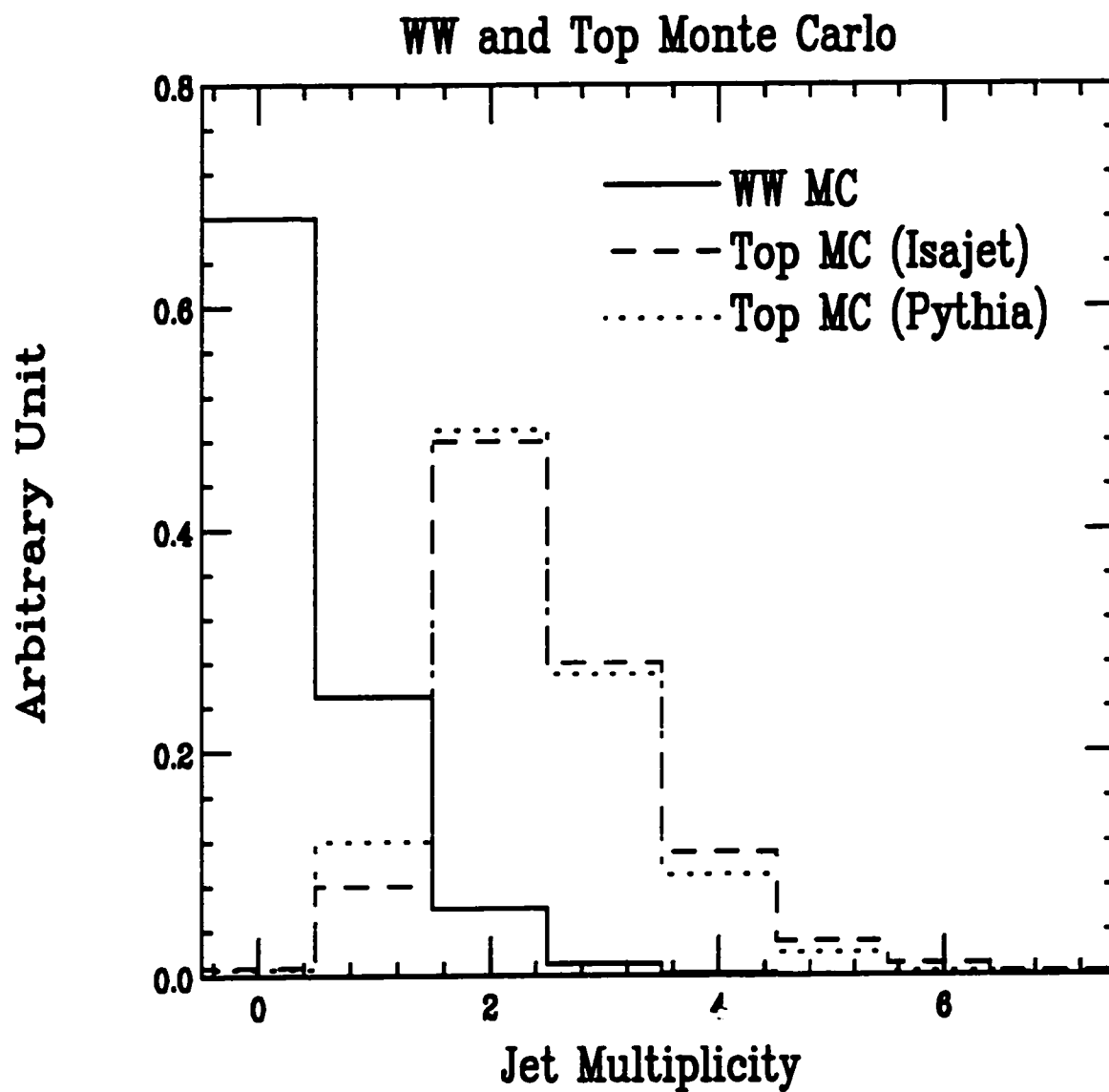


Figure 4.6: Jet multiplicity in $t\bar{t} \rightarrow W^+W^-b\bar{b}$ from ISAJET and PYTHIA simulations. The top quark mass is taken as $170 \text{ GeV}/c^2$. See text for W^+W^- jet multiplicity.

$$\begin{aligned}
&= 230 \times 108 \times 0.0317 \times 34\% \times \\
&\quad (1.03\% \times 1.43\% + 0.79\% \times 1.55\% + 2 \times 1.02\% \times 2.78\%) \\
&= 0.22.
\end{aligned}$$

Here $\int \mathcal{L} dt = 108 \text{ pb}^{-1}$ is the total integrated luminosity.

The two τ 's are most likely to be back-to-back, so the $\Delta\phi$ cut mentioned earlier is very efficient to reduce this background (Figures 4.7 and 4.8). In other words, jets are needed for $Z \rightarrow \tau\tau$ to survive this cut because the τ 's are no longer aligned in this case. So the 0-jet cut is also useful to reduce this background.

4.2.3 Drell-Yan

Among the dielectron events in the inclusive data set, 2,178 events are found inside the Z mass window and 213 events outside the mass window. Two of the 2,178 Z events pass all the selection cuts. So the background from $Z \rightarrow e^+e^-$ would be

$$213 \times \frac{2}{2178} = 0.20 \pm 0.14.$$

Here I first calculate the rejection factor obtained from the events inside the Z mass window, and then apply it to the events outside the mass window. The error is statistical only.

Similarly, for dimuon events in the data set, 1,457 events are found inside the Z mass window and 169 events outside the mass window. Two of the 1,457 Z

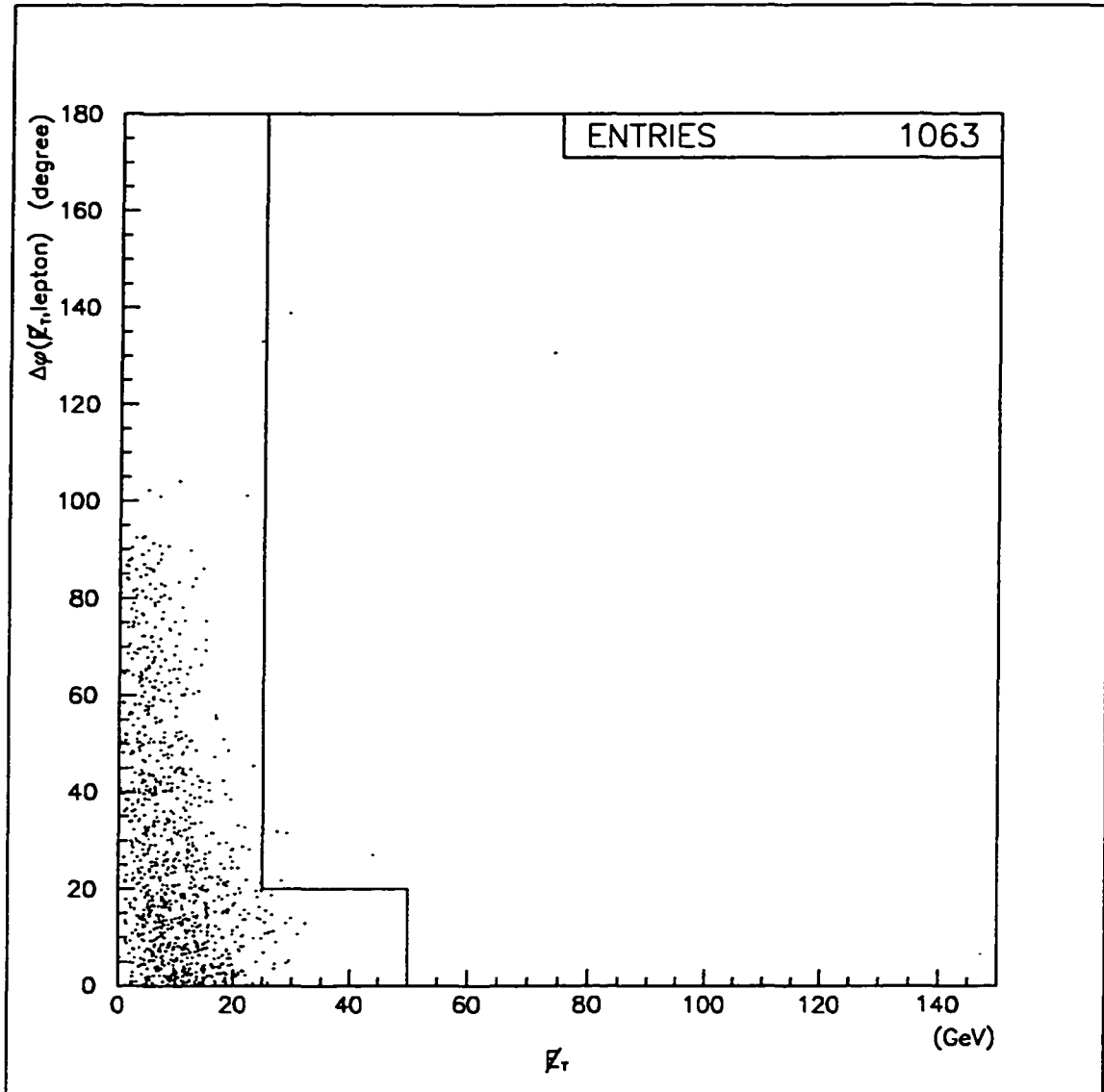


Figure 4.7: Distribution of the azimuthal angle between \cancel{E}_T and the closest lepton vs \cancel{E}_T , from $Z \rightarrow \tau\tau$ simulations. Leptons from $Z \rightarrow ee(\mu\mu)$ data samples are replaced with τ 's which are then forced to decay into electrons or muons.

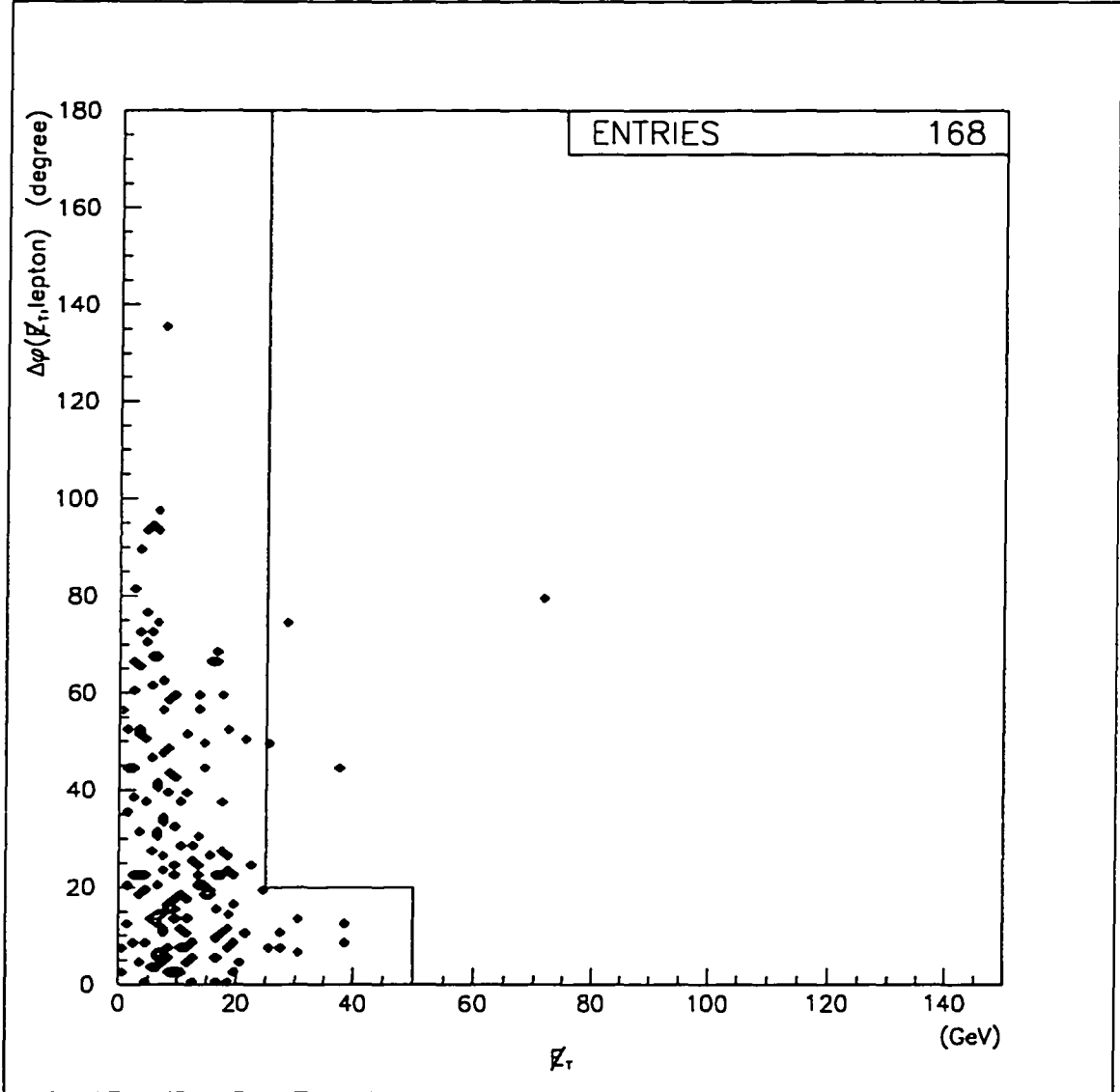


Figure 4.8: Distribution of the azimuthal angle between \cancel{E}_T and the closest lepton vs \cancel{E}_T , from ISAJET $Z \rightarrow \tau\tau$ simulations.

events pass all the selection cuts. So the background from $Z \rightarrow \mu^+ \mu^-$ would be

$$169 \times \frac{2}{1457} = 0.23 \pm 0.16.$$

The error is statistical only.

The \cancel{E}_T in Z events most likely comes from mismeasurements of lepton and jet energy. If the 0-jet cut is imposed in the W^+W^- selection, the Drell-Yan background, already suppressed by the Z mass window cut, is further reduced. After the 0-jet cut, many of those events with large \cancel{E}_T are gone. So besides the Z mass window cut, the 0-jet cut is a powerful cut to reduce the Drell-Yan background if $\cancel{E}_T > 25$ GeV is applied at the same time, see Figures 4.9 and 4.10.

4.2.4 Fake Leptons

The fake background is referred to those W +jets events with one jet misidentified as lepton. To estimate this background, jet data samples are used to find the fake probability, which is then applied to W +jets data samples.

The fake rate is calculated as follows: First find N_{real} —the number of jet events that pass all the lepton selection cuts. Then search for those jet events that fail the lepton selection cuts listed in Table 4.9 but pass the rest of the cuts, which are sometimes called “pseudo” leptons. Note that the cuts listed in Table 4.9 are commonly used to distinguish leptons from jets—shower profiles and energy deposited in the calorimeters. Let N_{pseudo} denote the number of these

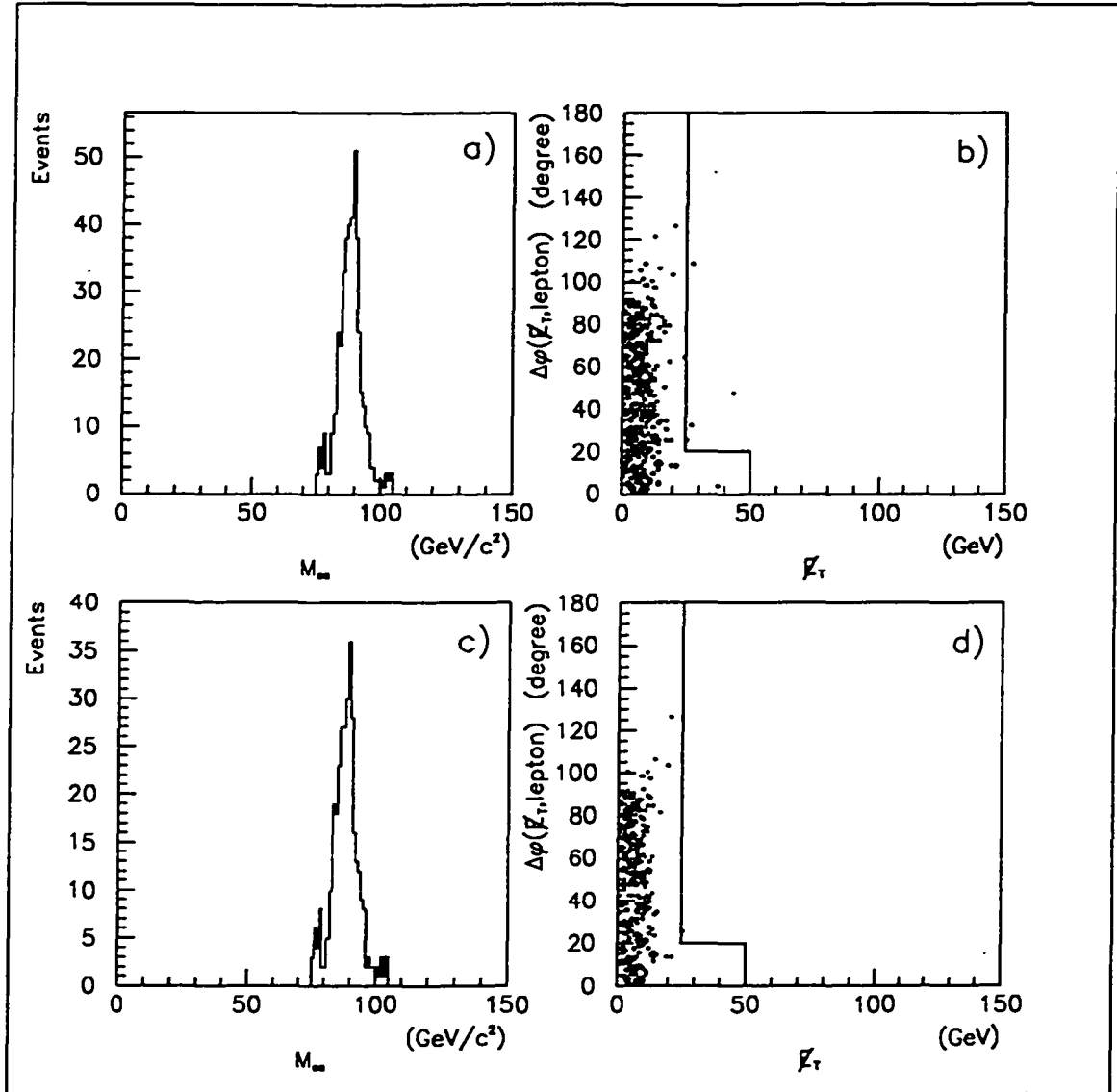


Figure 4.9: Distributions of the invariant mass and azimuthal angle between \vec{E}_T and the closest lepton in $Z \rightarrow e^+e^-$. (a) and (b) are distributions before the jet veto, while (c) and (d) are after the cut.

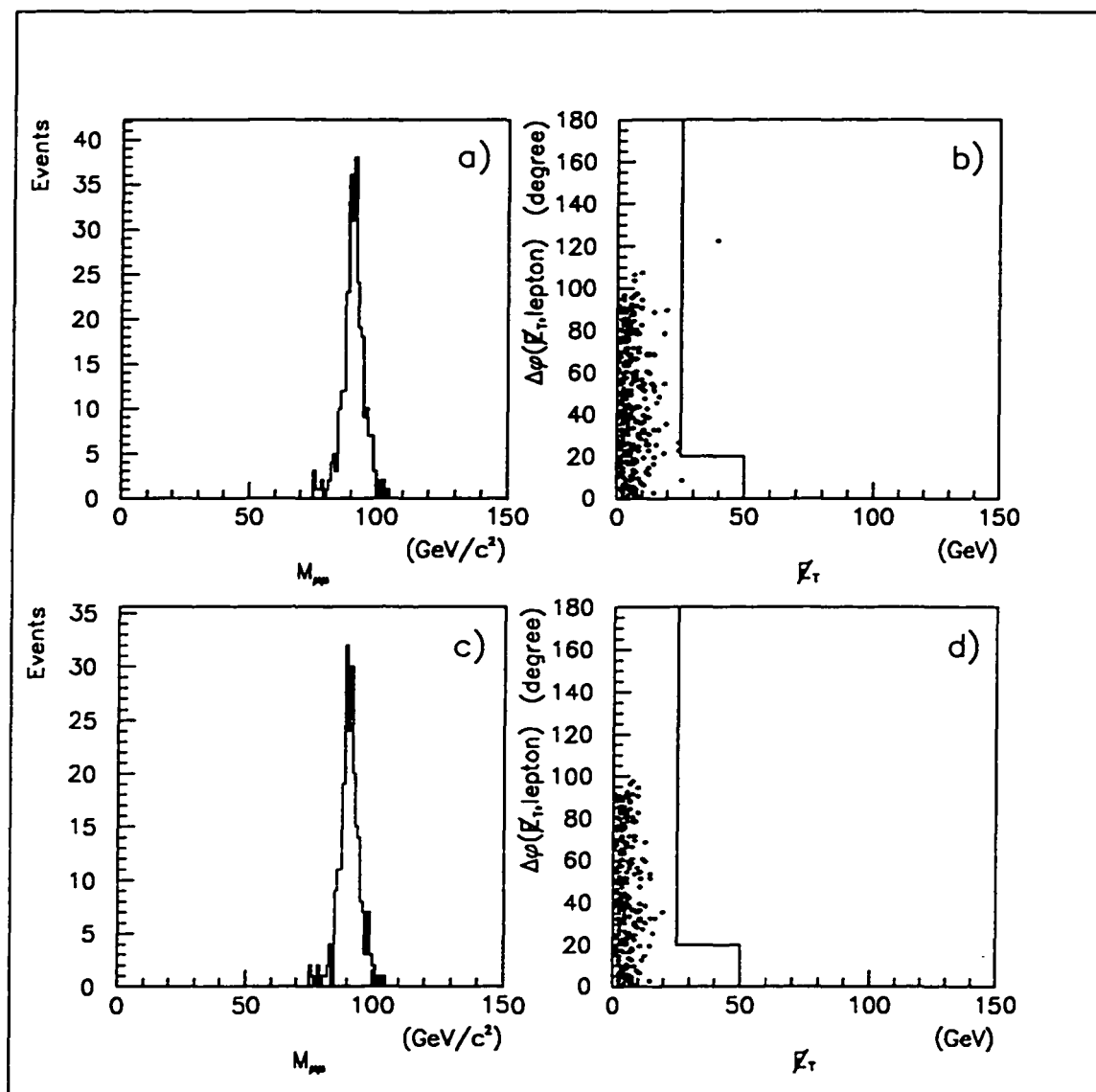


Figure 4.10: Distributions of the invariant mass and azimuthal angle between \cancel{P}_T and the closest lepton in $Z \rightarrow \mu^+ \mu^-$. (a) and (b) are distributions before the jet veto, while (c) and (d) are after the cut.

Lepton	Variable
Central muons	HAD > 6 GeV or EM > 2 GeV
Central electrons	$L_{shr} > 0.2$ or HAD/EM > 0.055
Plug electrons	$\chi_{3 \times 3}^2 > 3$, or $\chi_{depth}^2 > 15$, or VTX occupancy < 0.5

Table 4.9: Lepton selection variables that are used to separate leptons from jets. Their definitions are given in Chapter 3.

“pseudo” leptons, then the fake rate f_{fake} is given by N_{real}/N_{pseudo} . Table 4.10 lists the fake rates derived from jet data samples[35].

The fake rate of FMU muons is estimated from CMU–FMU Z data samples. Clearly, those Z events with two like-sign muons are fake Z events. Assume that we have equal positive and negative fake FMU muons, the FMU fake rate is found to be 0.06 ± 0.03 . It is obtained by

$$2 \times \frac{N_{like-sign}}{N_{total}},$$

where $N_{like-sign}$ is the number of like-sign events, and N_{total} is the number of all events[16]. The factor 2 comes from the charge independence of the fake rate.

In the inclusive lepton sample used to search for W^+W^- , we first search for those dilepton events (with $N_{dilepton}$ as the number of events) which have one lepton passing all the lepton selection cuts and the second lepton falling into the “pseudo” lepton category. Then the event and 0-jet cuts are imposed on these

dilepton events. After this selection procedure, two CMU/CMP–“CMU/CMP”, one CMU/CMP–“PEM”, and one CMX–“PEM” events are found, where leptons in the quotation marks are those “pseudo” leptons defined earlier. Then the fake background is obtained by

$$\begin{aligned}
 N_{expected} &= \sum_{class} N_{dilepton} \times f_{fake} \\
 &= 2 \times 0.11 + 1 \times 0.09 + 1 \times 0.09 \\
 &= 0.40.
 \end{aligned}$$

Here 0.11 and 0.09 are the fake rates for CMU/CMP muons and PEM electrons, respectively. The sum is over all dilepton classes. A 50 % statistical uncertainty is assigned to this background.

4.2.5 WZ

ISAJET Monte Carlo is used to study the WZ background where one lepton from Z is lost in the detector. First, the WZ detection efficiency is calculated by requiring explicitly that TWO and ONLY TWO leptons pass the selection cuts. The total detection efficiency, which includes contributions from all dilepton classes, is found to be 13.1%. Here we use the same 0-jet efficiency $\epsilon_{0-jet} = 68\%$ as in the W^+W^- production because the invariant mass of WZ is close to that of W^+W^- . The WZ production cross section is 2.5 pb as calculated in Ref. [36]; the branching ratio is $\text{Br}(WZ \rightarrow eee + X) = 0.0035$. Then the expected number

Category	Fake Rate
CEM	0.0153 ± 0.0055
PEM	0.0930 ± 0.0284
CMU/CMP	0.1053 ± 0.0573
CMX	0.2857 ± 0.2645
CMIO	0.0370 ± 0.0222

Table 4.10: Fake rates derived from jet data samples.

of events from this background is given by

$$\begin{aligned}
 N_{expected} &= \sigma_{\bar{p}p \rightarrow WZ} \int \mathcal{L} dt B \tau \epsilon_{total} \\
 &= 2.5 \times 108 \times 0.0035 \times 13.1\% \\
 &= 0.12 \pm 0.05.
 \end{aligned}$$

The uncertainty, similar to that in the W^+W^- analysis, comes from the detection efficiency (14 %), integrated luminosity (7 %), and WZ production cross section (35 %).

4.2.6 $b\bar{b}$

The background from $b\bar{b}$ production is found negligible, partly due to the fact that both leptons are required to be well isolated. I have scanned the $b\bar{b}$ Monte Carlo data sample described in Ref. [37]. The total integrated luminosity is about 200 pb^{-1} , and only about 0.01 events are expected from this background.

Process	Without	
	0-jet cut	All cuts
$t\bar{t}$	5.00	0.04 ± 0.01
$Z \rightarrow \tau\tau$	0.66	0.22 ± 0.06
Drell-Yan	1.90	0.43 ± 0.21
WZ	0.17	0.12 ± 0.05
Fake	1.80	0.40 ± 0.20
Total	9.53	1.21 ± 0.30

Table 4.11: Backgrounds to W^+W^- in the 108 pb^{-1} data sample.

So this background is dropped from W^+W^- search.

4.2.7 Summary

The background discussion is summarized in Table 4.11. Since no FMU-associated W^+W^- candidates are found, the FMU-related background is ignored in the analysis. The large background from the Drell-Yan process is disturbing. Naively, one would not expect large missing transverse energy from this process. One scenario is that jets from Z production are either lost or poorly measured in the calorimeters. The transverse energy is thus unbalanced, leading to a large \cancel{E}_T . Other backgrounds, on the other hand, are more or less under control by some specifically designed cuts.

Chapter 5

Results

A total of 108 pb^{-1} of $\bar{p}p$ collisions was collected at the CDF during the whole Run I. This large data set makes W^+W^- search possible for the first time in the history of high energy physics. Due to limited statistics, this study is by no means a precision measurement. Nevertheless, W^+W^- search will shed a light on trilinear gauge boson couplings—an important aspect of the standard model. In this chapter, I will present results of W^+W^- search at the CDF. The W^+W^- production cross section $\sigma(\bar{p}p \rightarrow W^+W^-)$ is measured for the first time. Then limits on $WW\gamma$ and WWZ anomalous couplings are set at 95 % confidence level.

5.1 Data Overview

Table 5.1 gives an overview of the 108 pb^{-1} data set. Each number shown in the table is the number of events after the cut listed in the corresponding column.

See Chapter 4 for the definition of these cuts. The missing E_T distributions just after the lepton selection and isolation cuts are given from Figure 5.1 to Figure 5.6. The invariant mass distributions in the ee and $\mu\mu$ channels are shown from Figure 5.7 to Figure 5.10. It should be pointed out that the data set has been validated by the CDF offline group, and therefore is the CDF official data for Run I. Finally, the uncertainty of luminosity is 4 % for 1A data (19.3 pb^{-1}) and 8 % for 1B data (88.7 pb^{-1})[21]. So the weighted overall uncertainty is 7 %.

Category	ID	Isolation	Z mass	\cancel{E}_T	Jet veto
e^+e^-	2587	2391	213	5	2
$\mu^+\mu^-$	1804	1626	169	9	0
$e^+\mu^- + e^-\mu^+$	37	28	28	10	3

Table 5.1: Summary of dilepton events in the 108 pb^{-1} data.

5.2 W^+W^- Cross Section

5.2.1 Measurement

To measure the W^+W^- production cross section $\sigma(\bar{p}p \rightarrow W^+W^-)$, one has to take account of the detection efficiency, integrated luminosity, branching ratio,

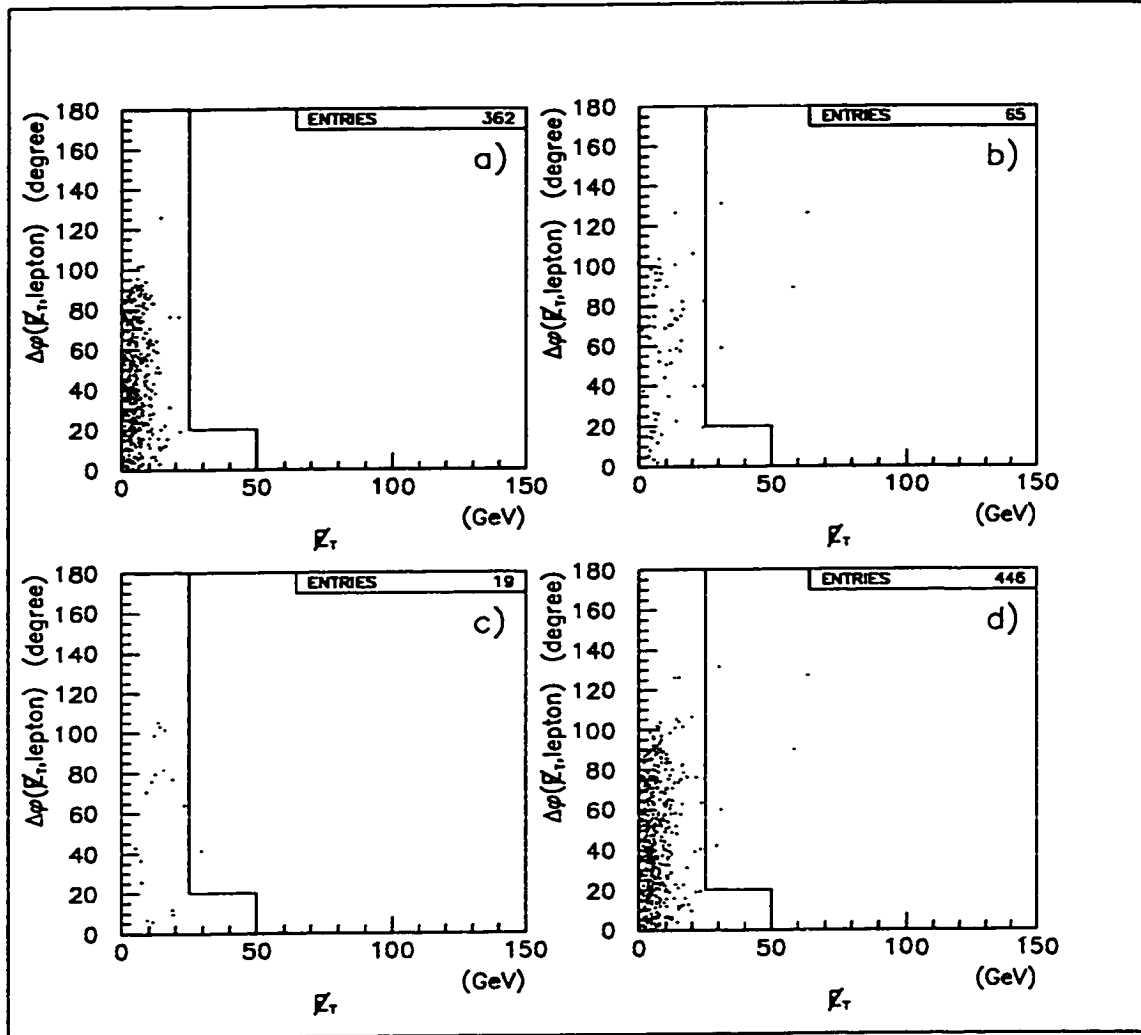


Figure 5.1: Distributions of the azimuthal angle between E_T and the closest lepton vs E_T in the ee channel. (a) Events without jets, (b) events with one jet, (c) events with two or more jets, and (d) all events. 1A data only.

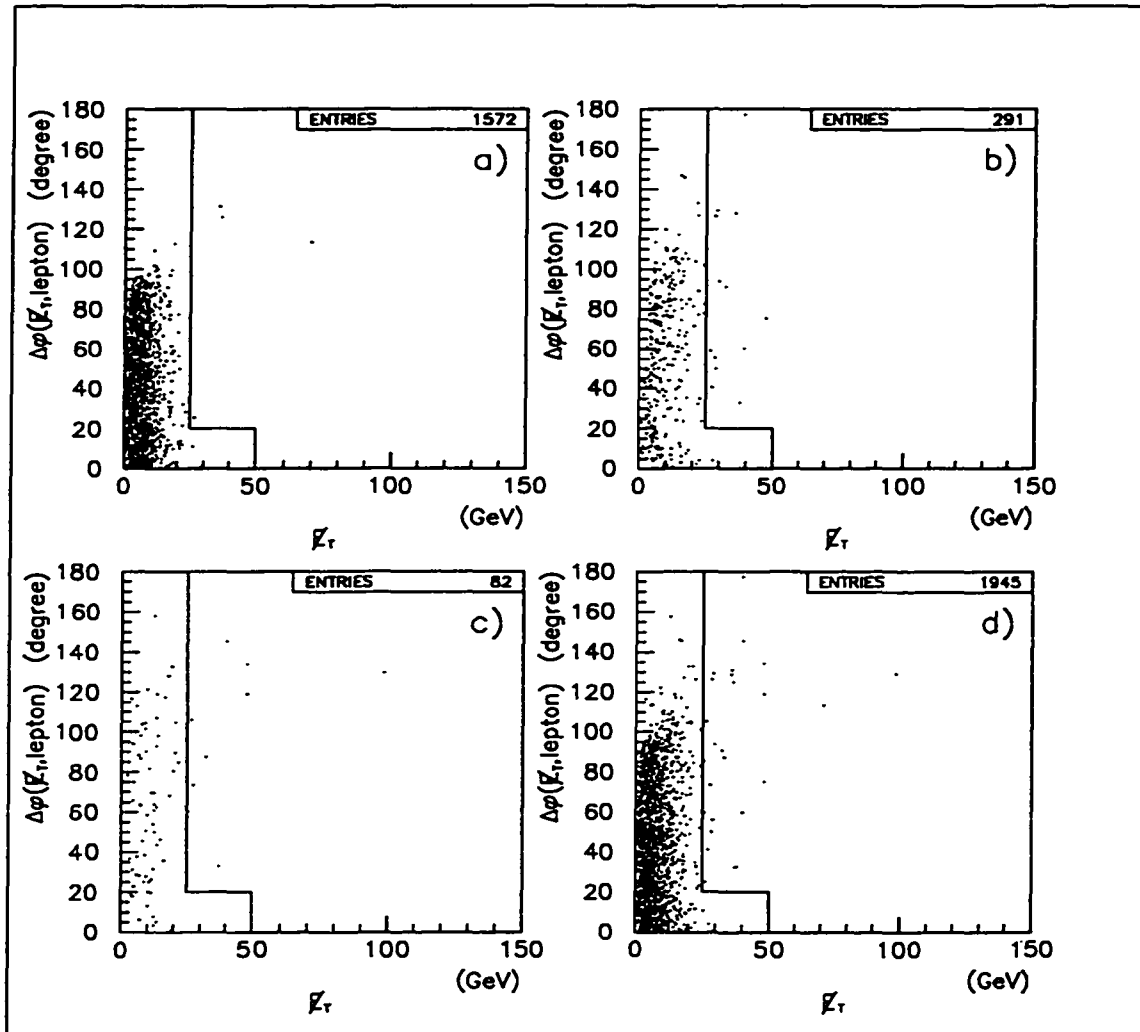


Figure 5.2: Distributions of the azimuthal angle between ℓ_T and the closest lepton vs ℓ_T in the ee channel. (a) Events without jets, (b) events with one jet, (c) events with two or more jets, and (d) all events. 1B data only.

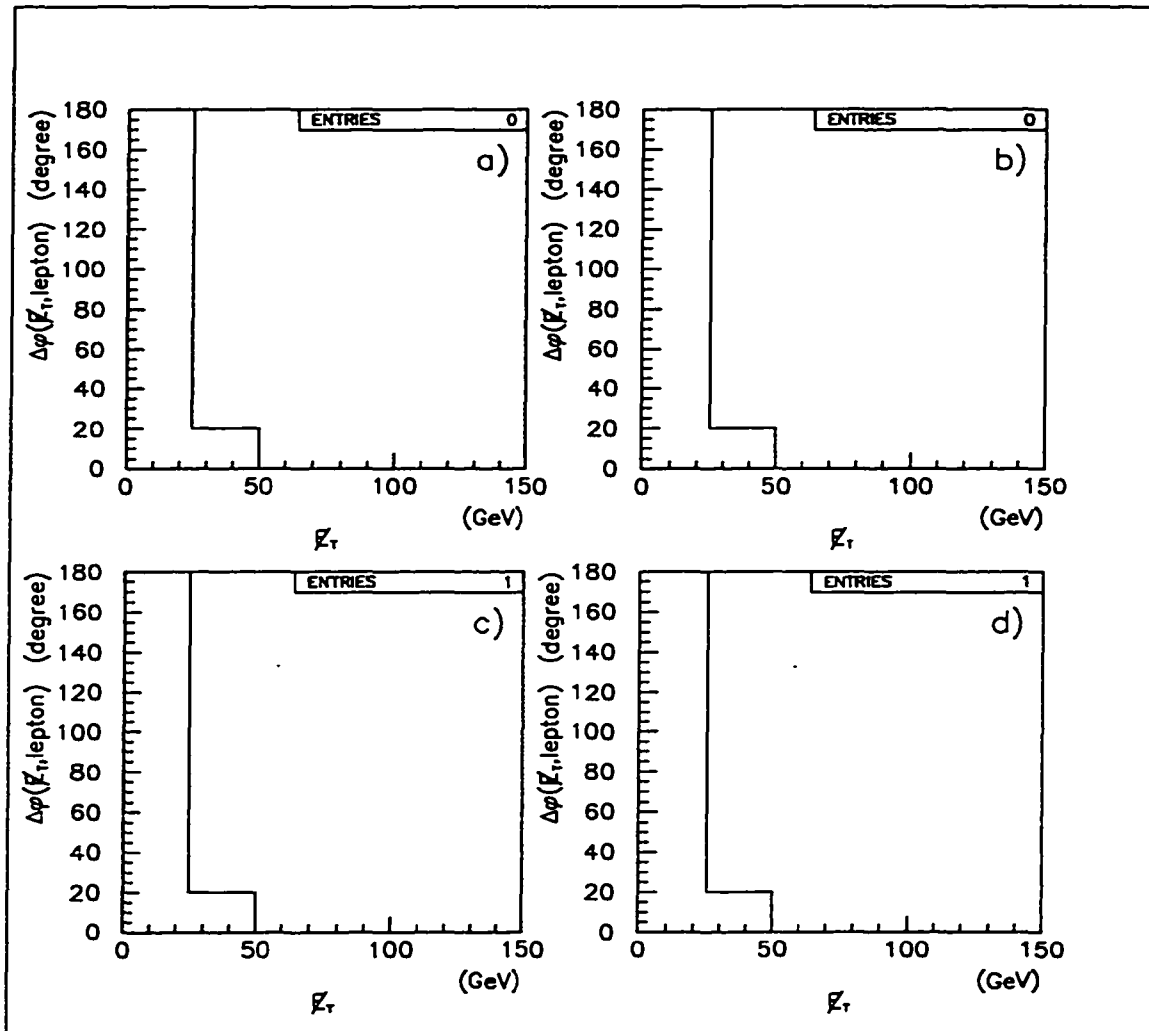


Figure 5.3: Distributions of the azimuthal angle between \cancel{E}_T and the closest lepton vs \cancel{E}_T in the $e\mu$ channel. (a) Events without jets, (b) events with one jet, (c) events with two or more jets, and (d) all events. 1A data only.

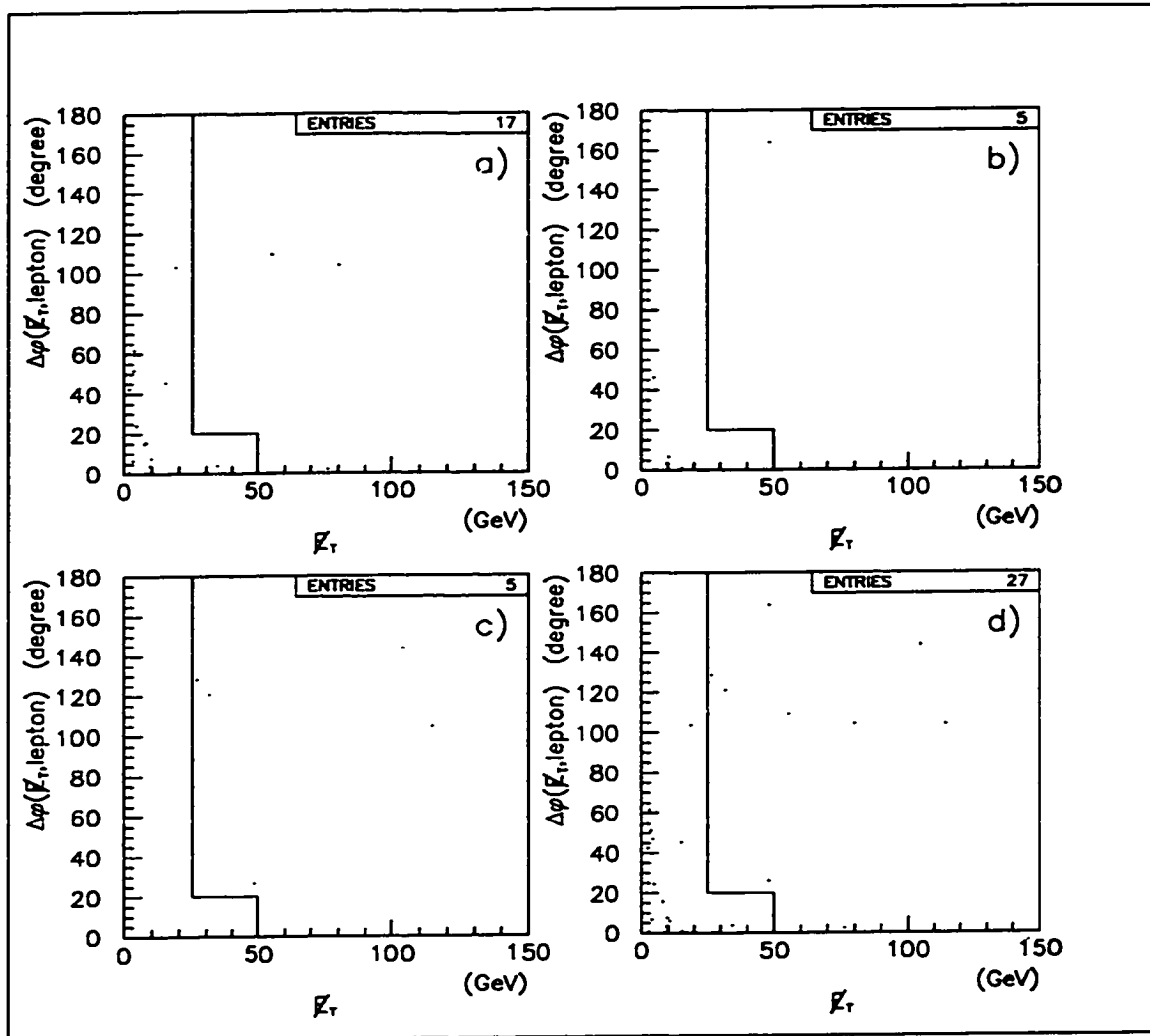


Figure 5.4: Distributions of the azimuthal angle between \cancel{E}_T and the closest lepton vs \cancel{E}_T in the $e\mu$ channel. (a) Events without jets, (b) events with one jet, (c) events with two or more jets, and (d) all events. 1B data only.

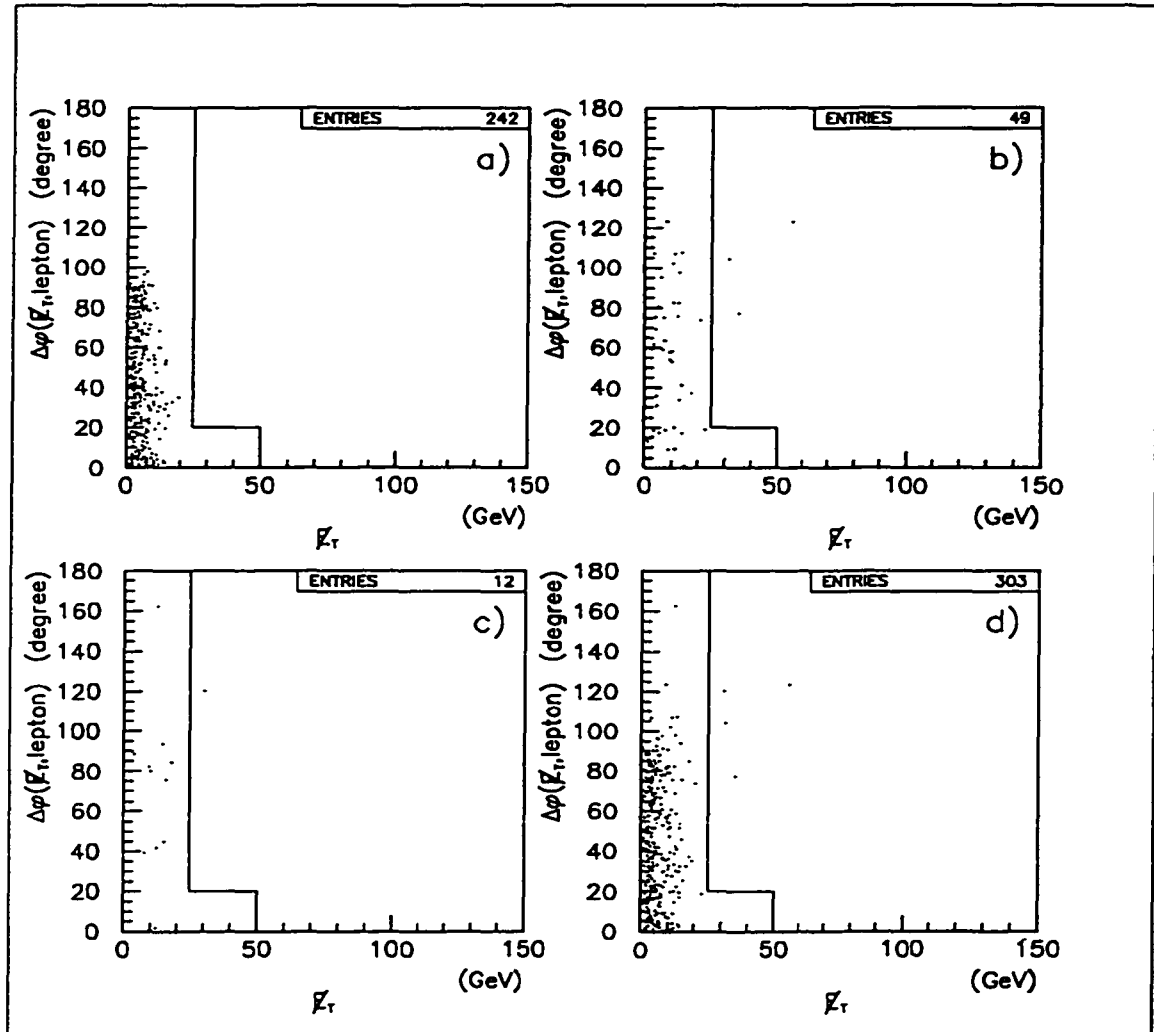


Figure 5.5: Distributions of the azimuthal angle between E_T and the closest lepton vs E_T in the $\mu\mu$ channel. (a) Events without jets, (b) events with one jet, (c) events with two or more jets, and (d) all events. 1A data only.

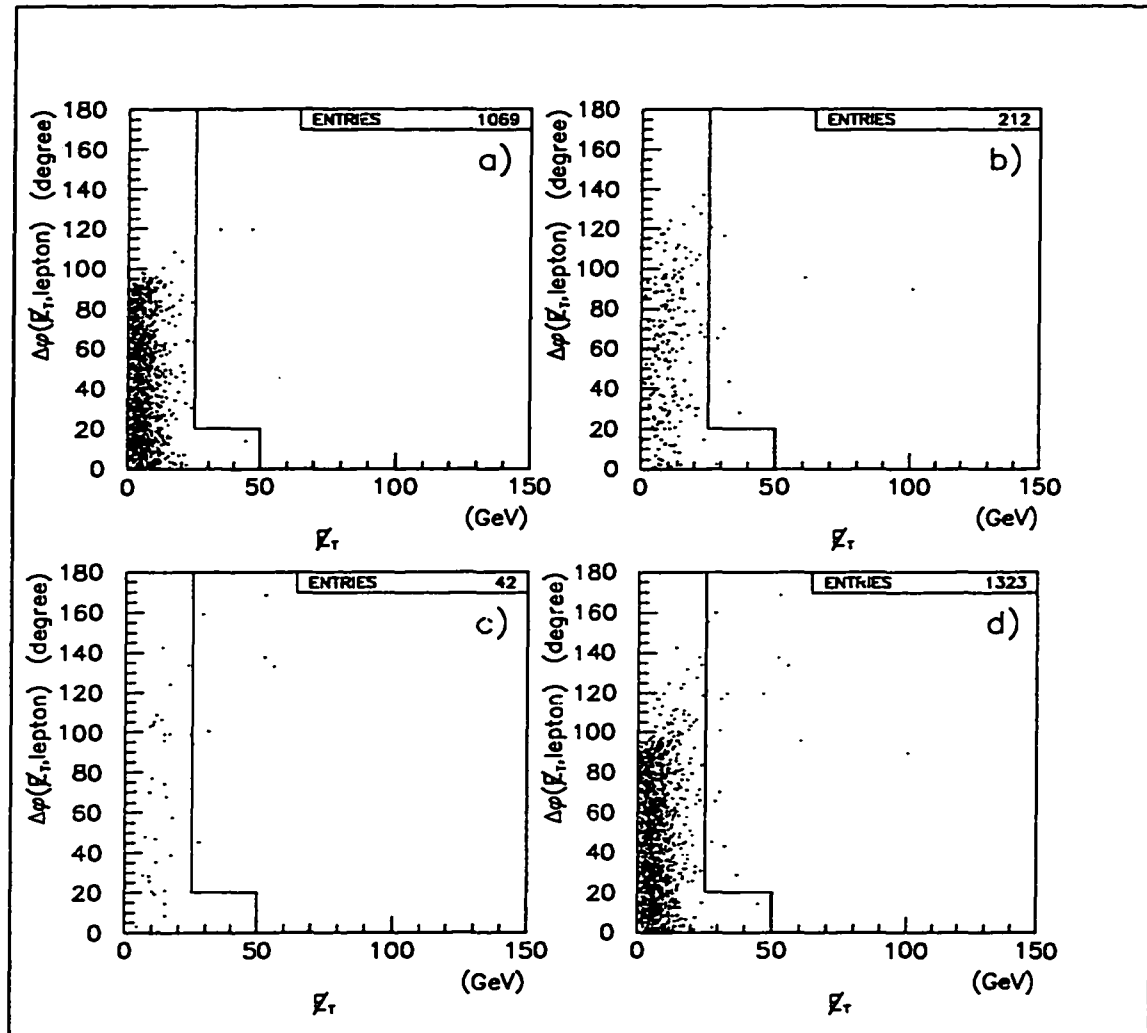


Figure 5.6: Distributions of the azimuthal angle between ℓ_T and the closest lepton vs ℓ_T in the $\mu\mu$ channel. (a) Events without jets, (b) events with one jet, (c) events with two or more jets, and (d) all events. 1B data only.

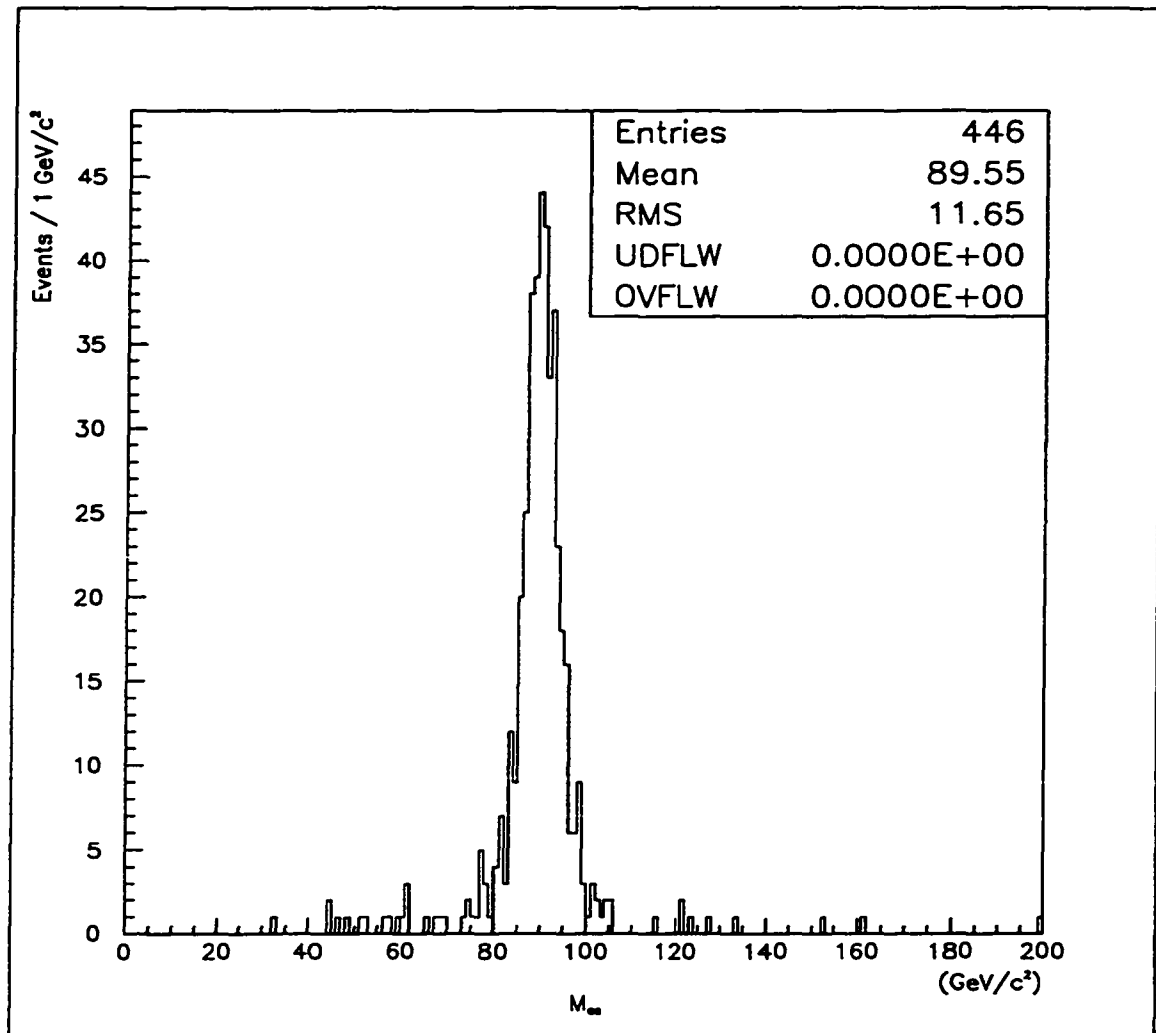


Figure 5.7: Distribution of the ee invariant mass, just after the lepton selection and isolation cuts. 1A data only.

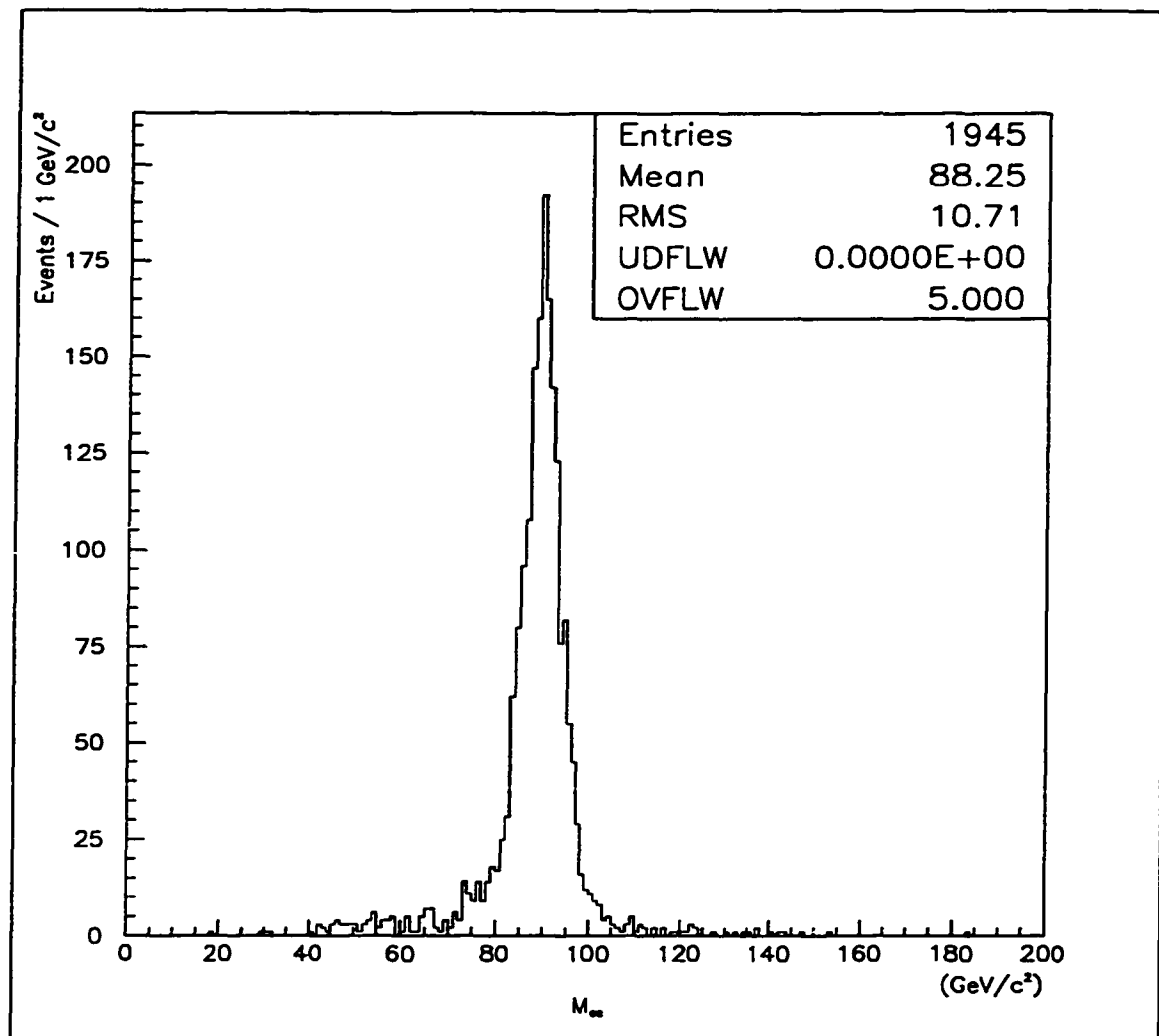


Figure 5.8: Distribution of the ee invariant mass, just after the lepton selection and isolation cuts. 1B data only.

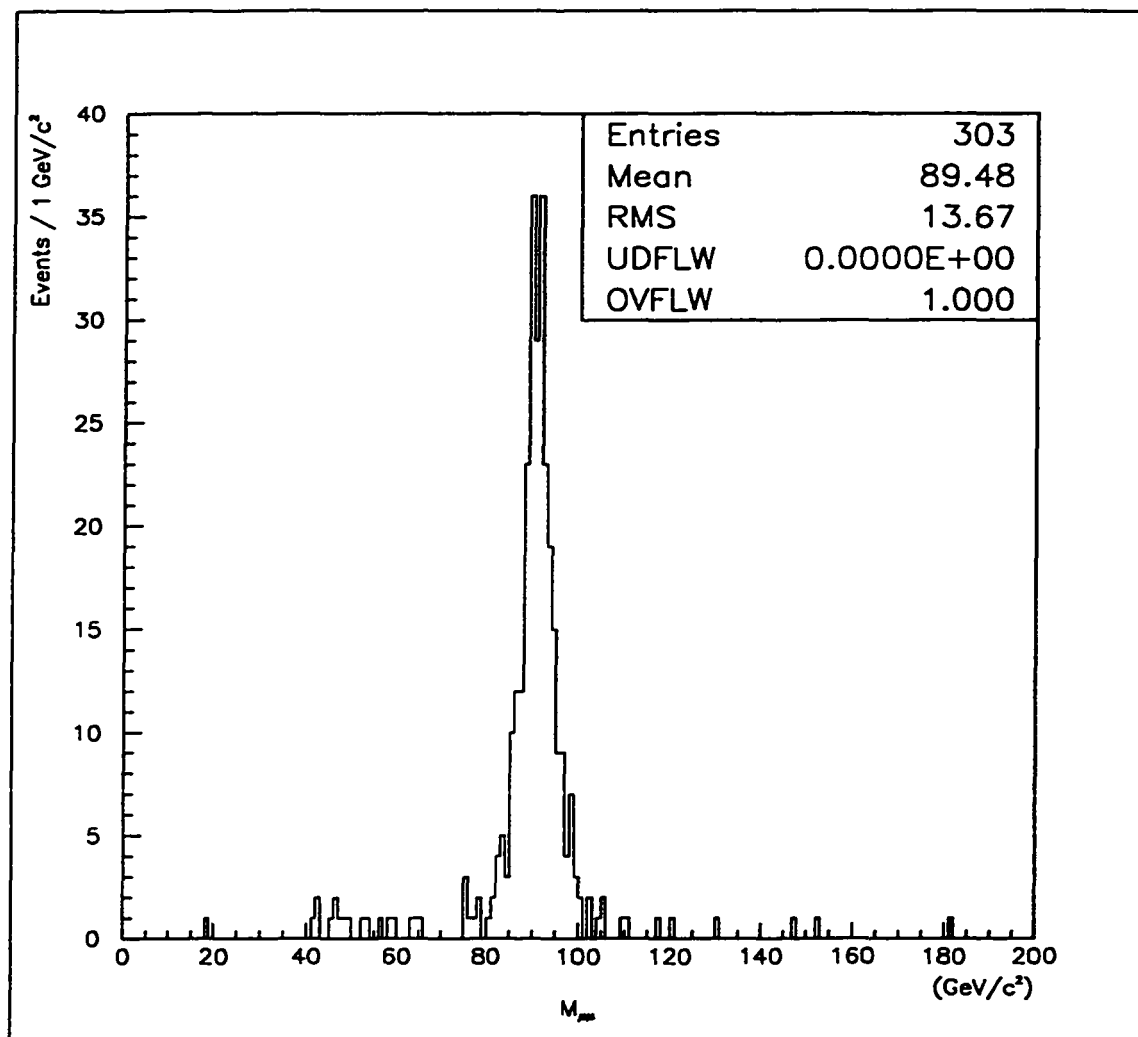


Figure 5.9: Distribution of the $\mu\mu$ invariant mass, just after the lepton selection and isolation cuts. 1A data only.

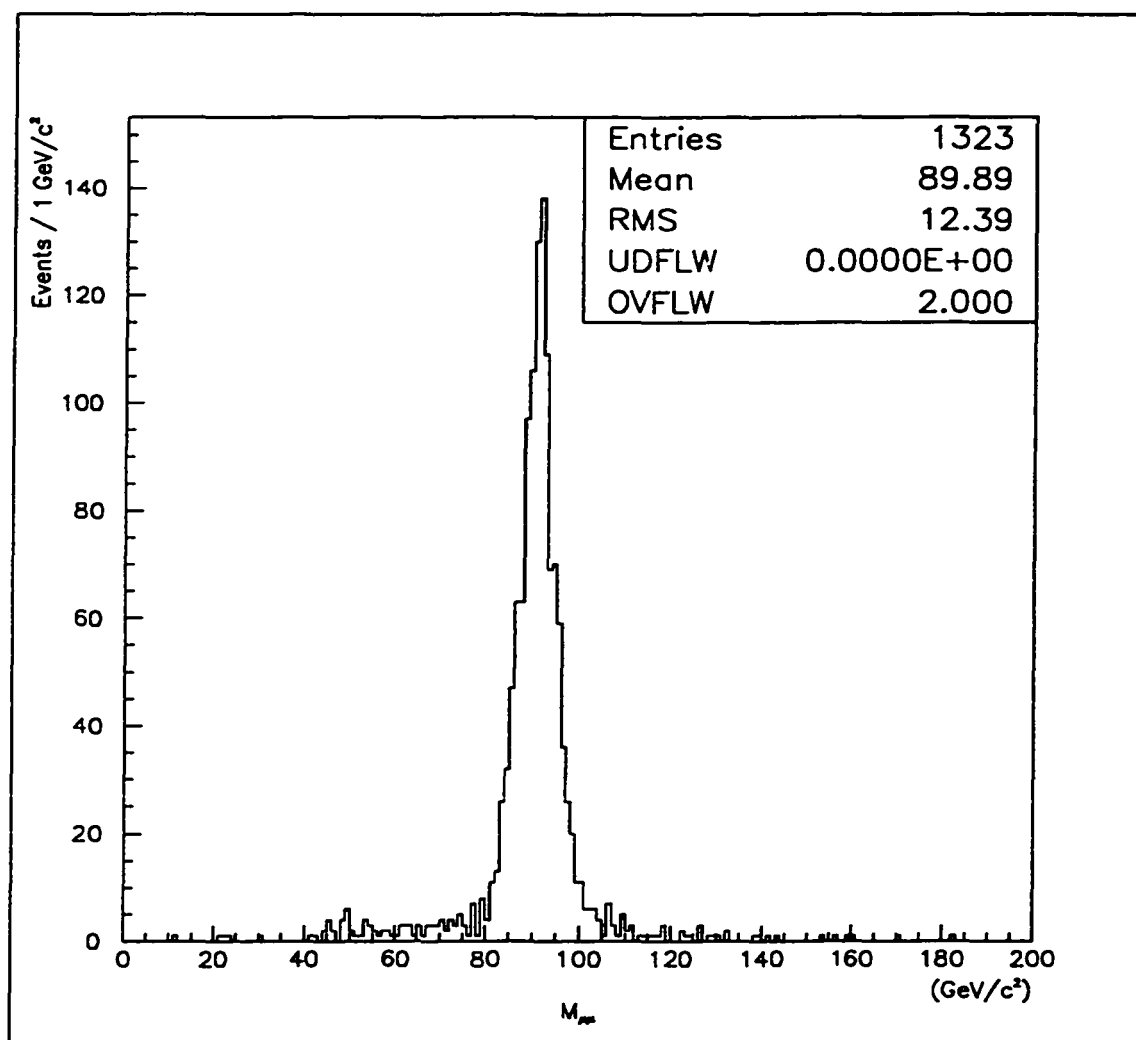


Figure 5.10: Distribution of the $\mu\mu$ invariant mass, just after the lepton selection and isolation cuts. 1B data only.

and background through the following expression

$$\sigma(\bar{p}p \rightarrow W^+W^-) = \frac{\text{candidates} - \text{background}}{\sum \int \mathcal{L}dt Br \epsilon_{total}}, \quad (5.1)$$

where $\int \mathcal{L}dt$ is the integrated luminosity, and the sum is over all dilepton classes. The branching ratio Br is 0.011 for $W^+W^- \rightarrow ee(\mu\mu)\nu\bar{\nu}$ and 0.022 for $W^+W^- \rightarrow e\mu\nu\bar{\nu}$. The small contribution from $W^+W^- \rightarrow l\tau$ or $\tau\tau$, followed by $\tau \rightarrow e$ or μ , is also included by using the branching ratio $\text{Br}(\tau \rightarrow \mu\nu\nu) = 0.18$. The total detection efficiency ϵ_{total} has been calculated in Chapter 4.

It will be very instructive to know how many $W^+W^- \rightarrow l^+l^-\nu\bar{\nu}$ events are expected in the 108 pb^{-1} data set. The number of W^+W^- events can be obtained from Eq. 5.1

$$N_{event} = \sigma(\bar{p}p \rightarrow W^+W^-) \sum_{class} \int \mathcal{L}dt Br \epsilon_{total}. \quad (5.2)$$

An order of α_s calculation[5] finds the continuum W^+W^- production cross section to be 9.5 pb, with 30 % uncertainty. Therefore, a total of 3.53 ± 1.24 W^+W^- events is expected. Adding the total background 1.21 ± 0.30 , we expect to observe about five W^+W^- candidates in the dilepton channel.

Five dilepton events in this data sample survive the W^+W^- selection cuts described in the last two chapters. These five candidates are displayed from Figure 5.11 to Figure 5.15. Shown are the calorimeter energy and CTC tracks. Table 5.2 lists some important quantities of these lepton pairs. The common features of these events are: (1) two high P_T leptons with opposite charges, (2) no jet activity, and (3) large \cancel{E}_T far away from either lepton. From Monte Carlo

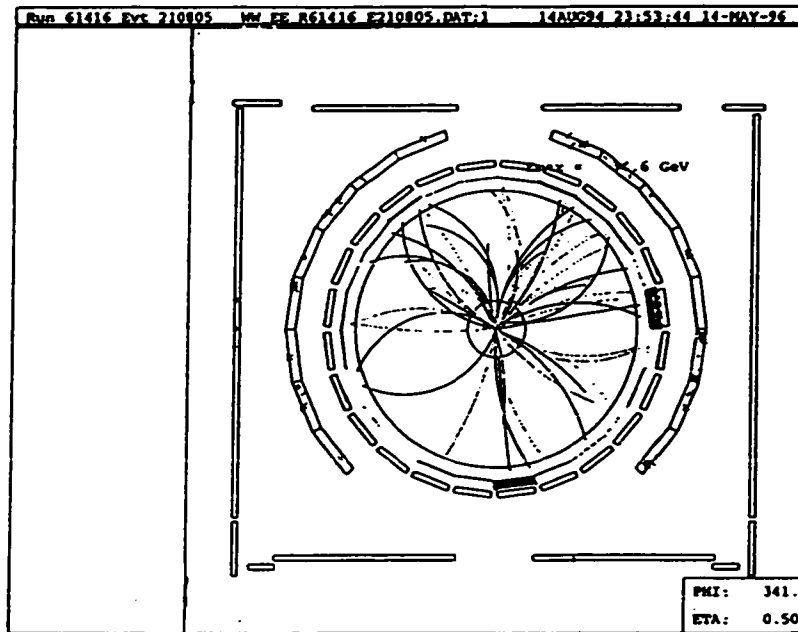
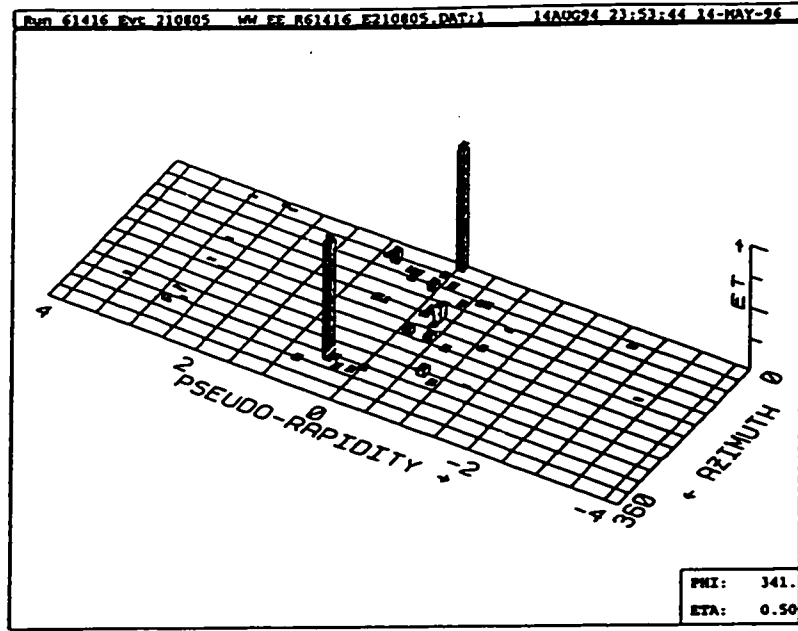


Figure 5.11: Event display for one of the W^+W^- candidates: calorimeter E_T in the η - ϕ plane (top); reconstructed CTC tracks and muon hits in the r - ϕ plane (bottom). Note that the muon only leaves a minimum ionizing energy in the calorimeters.

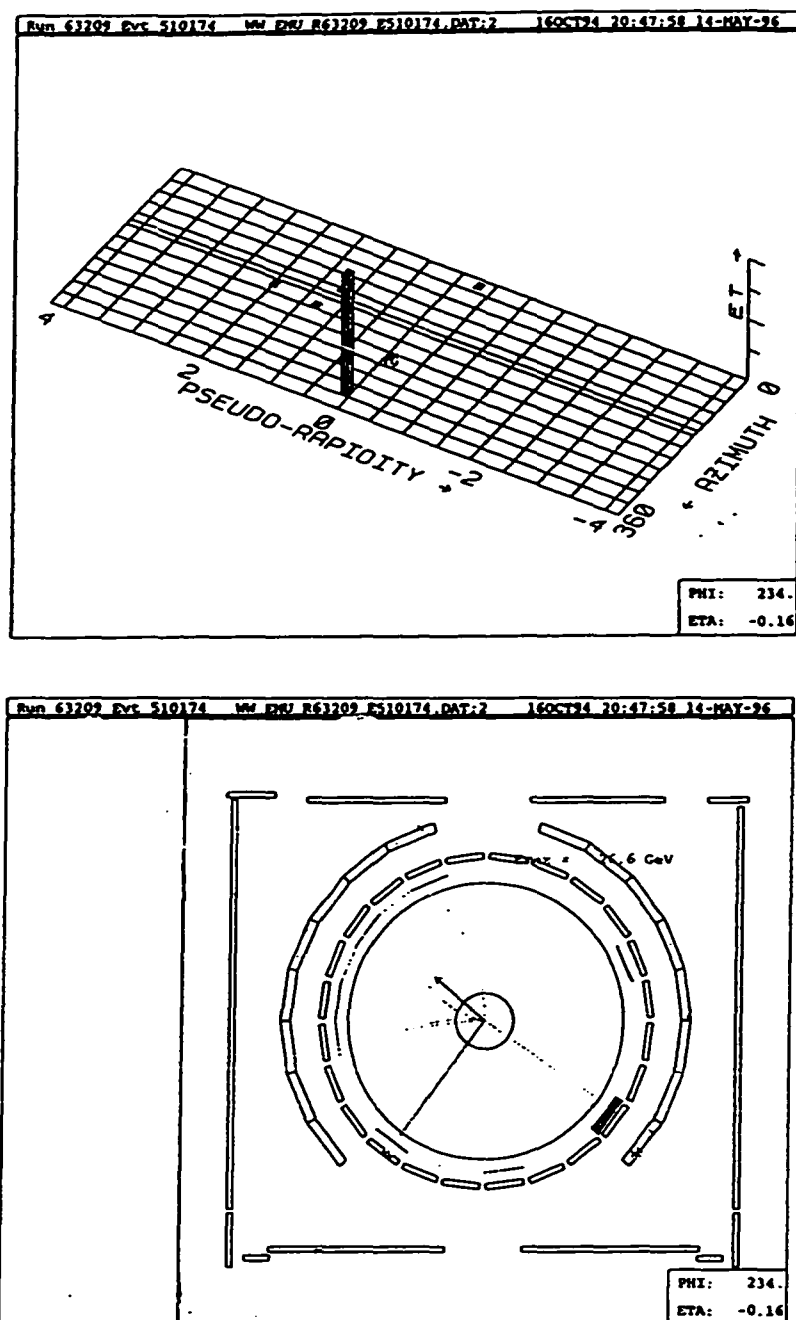


Figure 5.12: Event display for one of the W^+W^- candidates: calorimeter E_T in the η - ϕ plane (top); reconstructed CTC tracks and muon hits in the r - ϕ plane (bottom).

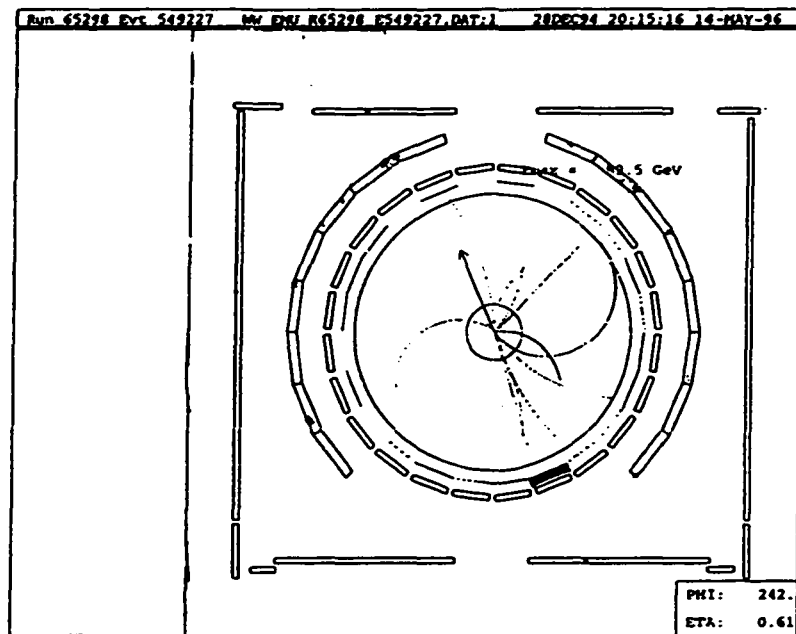
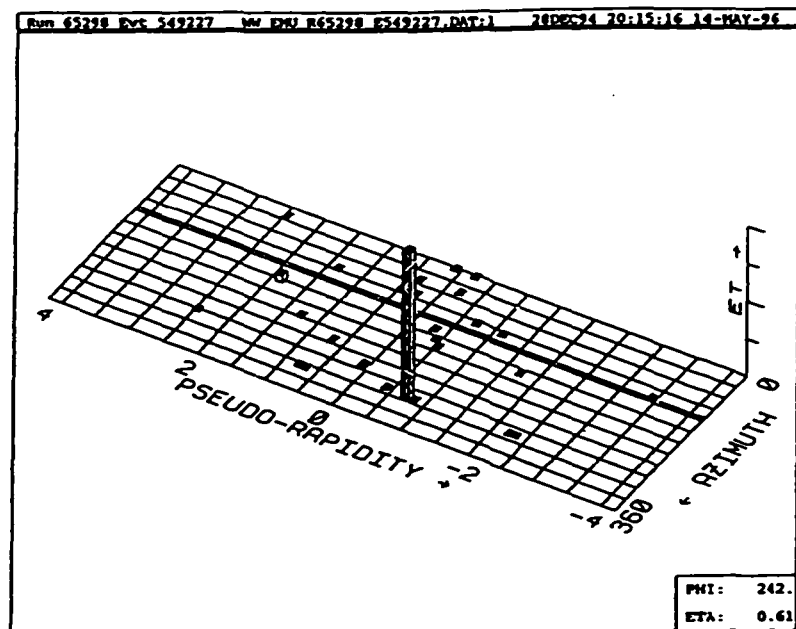


Figure 5.13: Event display for one of the W^+W^- candidates: calorimeter E_T in the η - ϕ plane (top); reconstructed CTC tracks and muon hits in the r - ϕ plane (bottom).

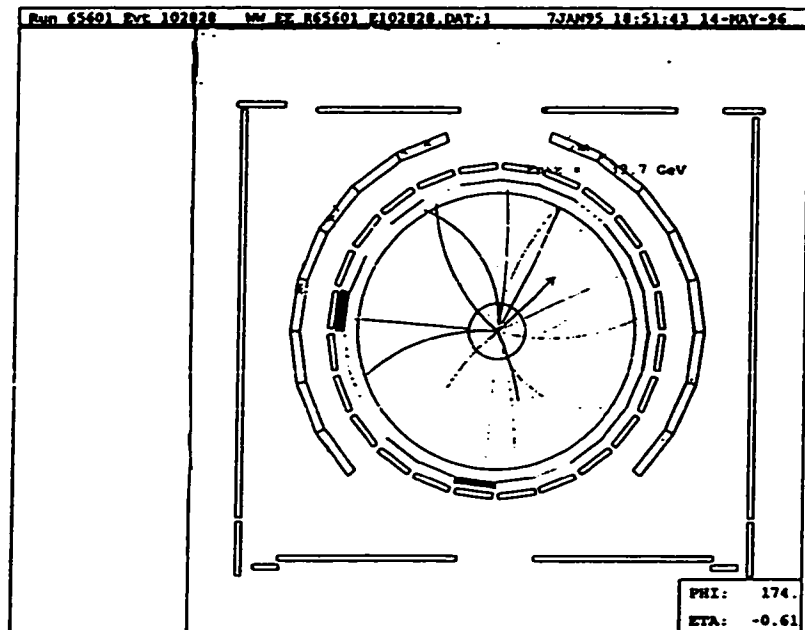
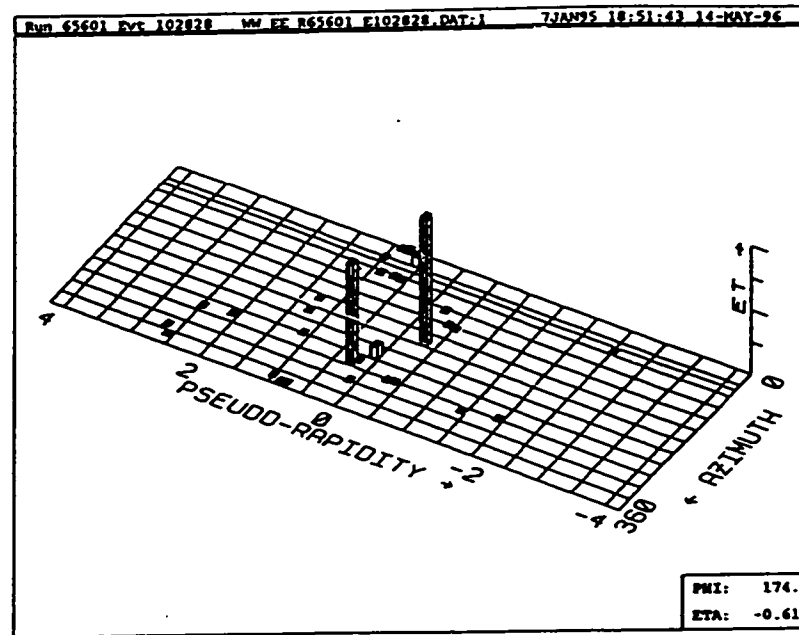


Figure 5.14: Event display for one of the W^+W^- candidates: calorimeter E_T in the η - ϕ plane (top); reconstructed CTC tracks and muon hits in the τ - ϕ plane (bottom).

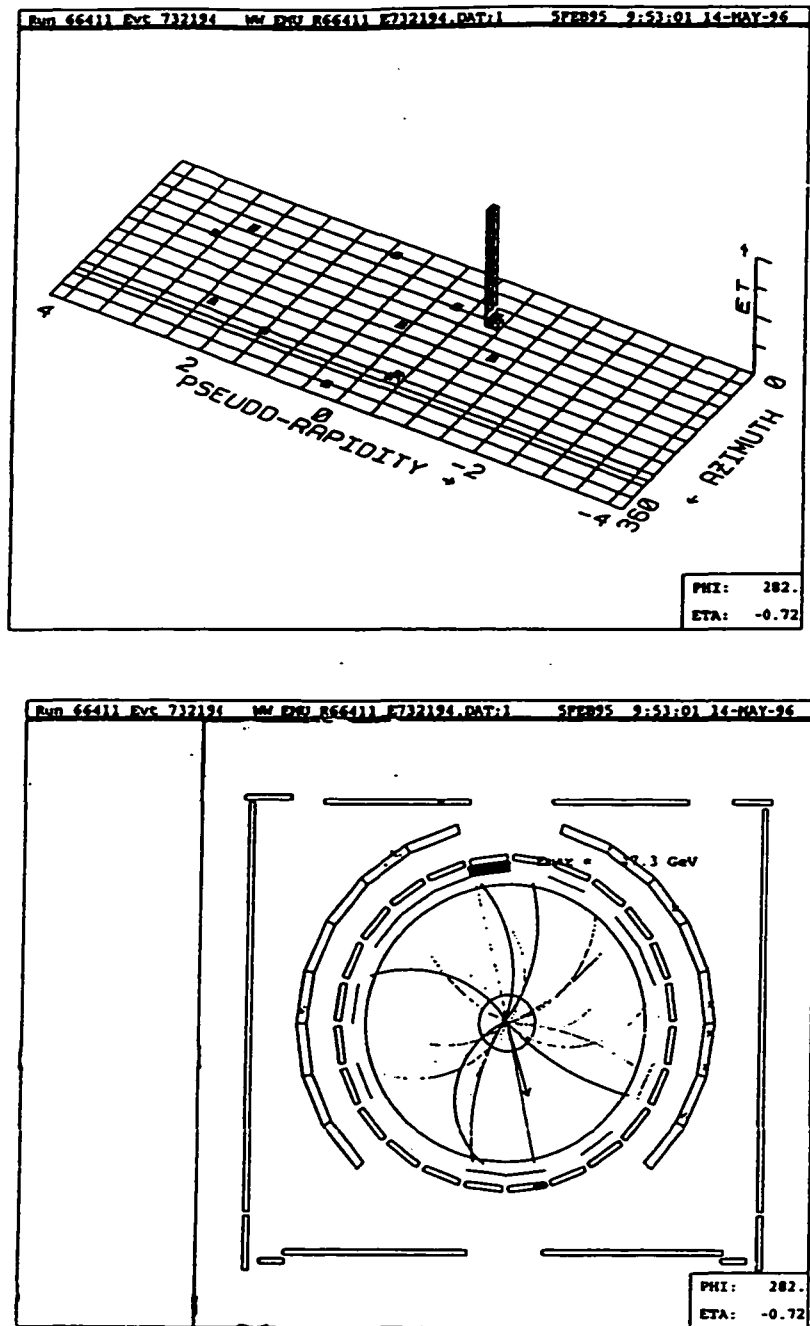


Figure 5.15: Event display for one of the W^+W^- candidates: calorimeter E_T in the η - ϕ plane (top); reconstructed CTC tracks and muon hits in the r - ϕ plane (bottom).

Run #		E_T	\cancel{E}_T	$\Delta\phi(\cancel{E}_T, l)$	Z vertex	M_{l+l^-}
Event #	Object	(GeV)	(GeV)	(degree)	(cm)	(GeV/c ²)
61416	electron	29				
210805	electron	29				
			36	127	-1.8	47
63209	electron	26				
510174	muon	78				
			73	106	-2.0	65
65298	electron	59				
549227	muon	42				
			55	109	9.6	119
65601	electron	32				
102828	electron	27				
			34	130	32.5	48
66411	electron	25				
732194	muon	109				
			62	3	57.1	107

Table 5.2: W^+W^- candidates in the 108 pb^{-1} data.

simulations and theoretical calculations, one concludes that these properties are the typical signature of W^+W^- events. In the decay $W \rightarrow l\nu$, the lepton and neutrino tend to be back-to-back due to the huge mass and small momenta of W bosons in $\bar{p}p \rightarrow W^+W^-$. So if the two neutrinos in $W^+W^- \rightarrow l^+l^-\nu\bar{\nu}$ are aligned in the same direction to form a large \cancel{E}_T , then the two leptons must be aligned together in the opposite direction, thus leading to a large $\Delta\phi(\cancel{E}_T, \text{lepton})$. By the same token, small \cancel{E}_T corresponds to small $\Delta\phi$. Monte Carlo simulations of W^+W^- production validate this simple but powerful argument, see Figure 5.16. Therefore, while the $\Delta\phi$ cut greatly reduces various backgrounds to W^+W^- production, the W^+W^- acceptance just suffers slightly from this cut. The missing transverse energy distributions for W^+W^- candidates are shown in Figures 5.17 and 5.18. The two neutrinos from $W^+W^- \rightarrow l^+l^-\nu\bar{\nu}$ give a very large \cancel{E}_T . By contrast, the background is expected to have smaller \cancel{E}_T and therefore most of it falls into the first bin in Figure 5.18.

Now we can measure the W^+W^- cross section $\sigma(\bar{p}p \rightarrow W^+W^-)$, although the statistics is very limited. Given $N_{event} = 3.79$ after background subtraction, a straightforward application of Eq. 5.1 leads to

$$\sigma(\bar{p}p \rightarrow W^+W^-) = 10.2_{-5.1}^{+6.3} \text{ (stat)} \pm 1.6 \text{ (syst) pb.}$$

Assuming number of events follows the Poisson distribution with the observed number of events as its mean, the statistical uncertainty for five events is obtained by requiring the ratio of the area covered by the upper (lower) bound to the total

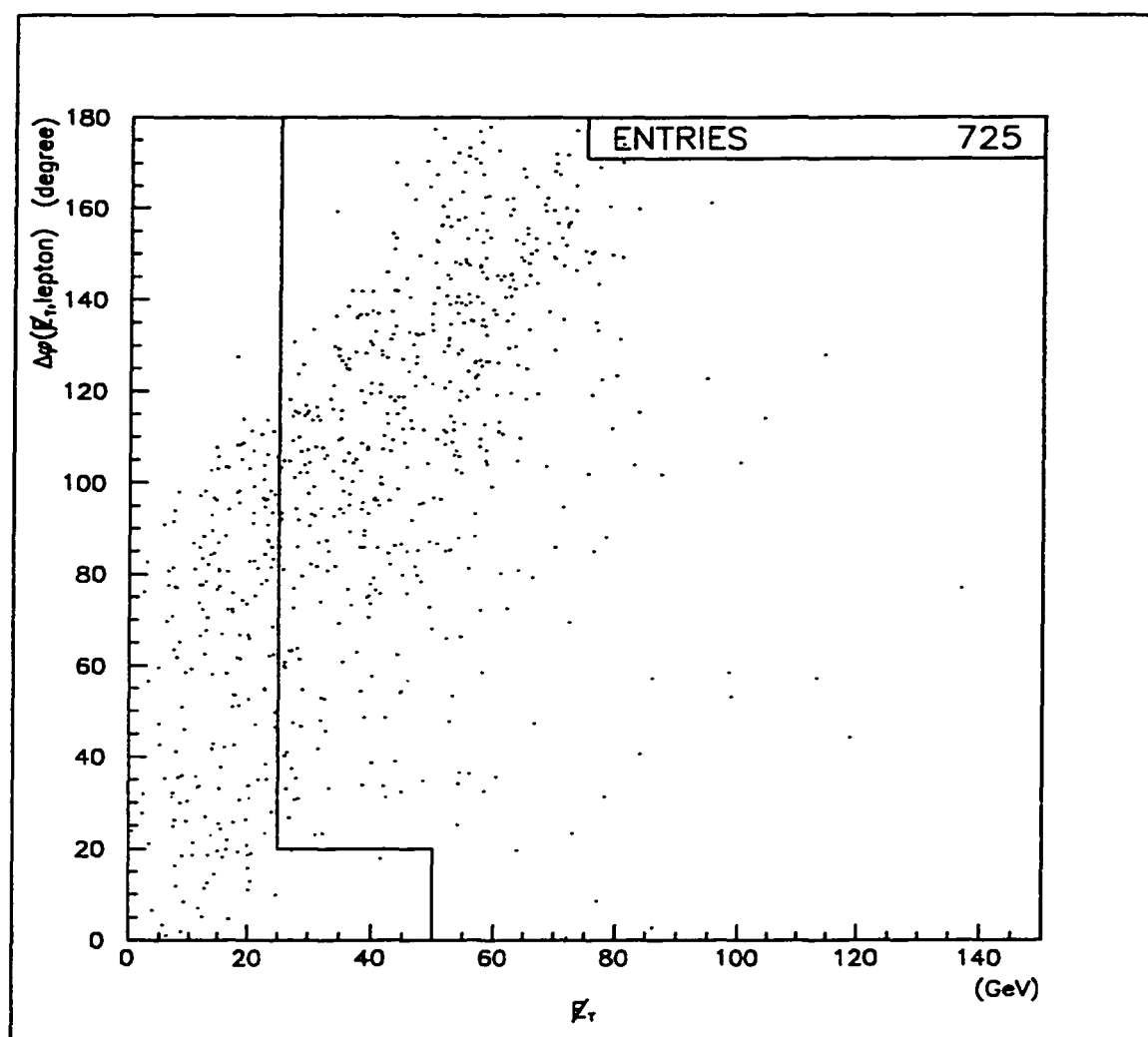


Figure 5.16: Azimuthal angle between the \cancel{E}_T direction and the closest lepton, versus \cancel{E}_T , from W^+W^- simulations.

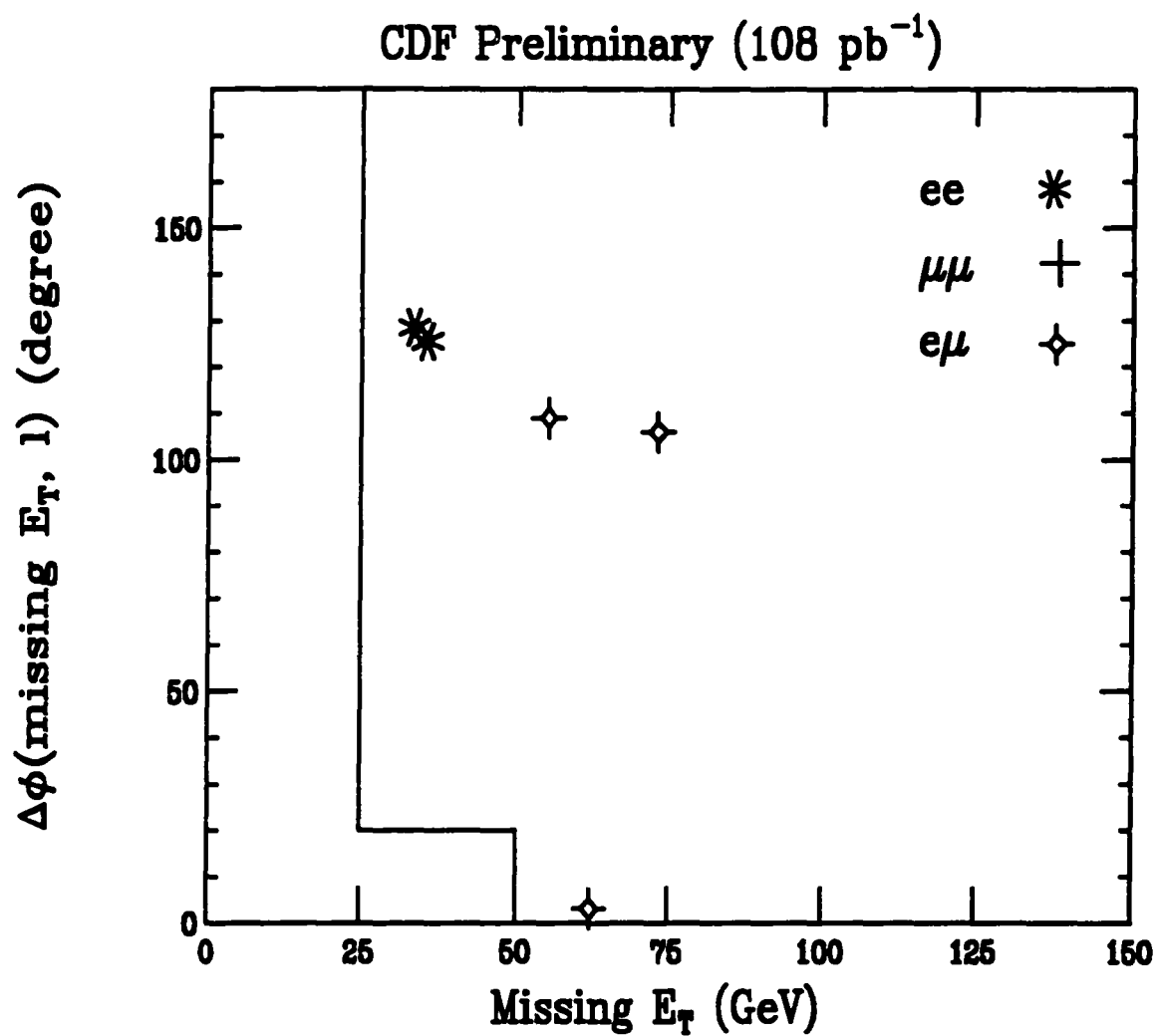


Figure 5.17: Azimuthal angle between the \cancel{E}_T direction and the closest lepton, versus \cancel{E}_T , for W^+W^- candidates.

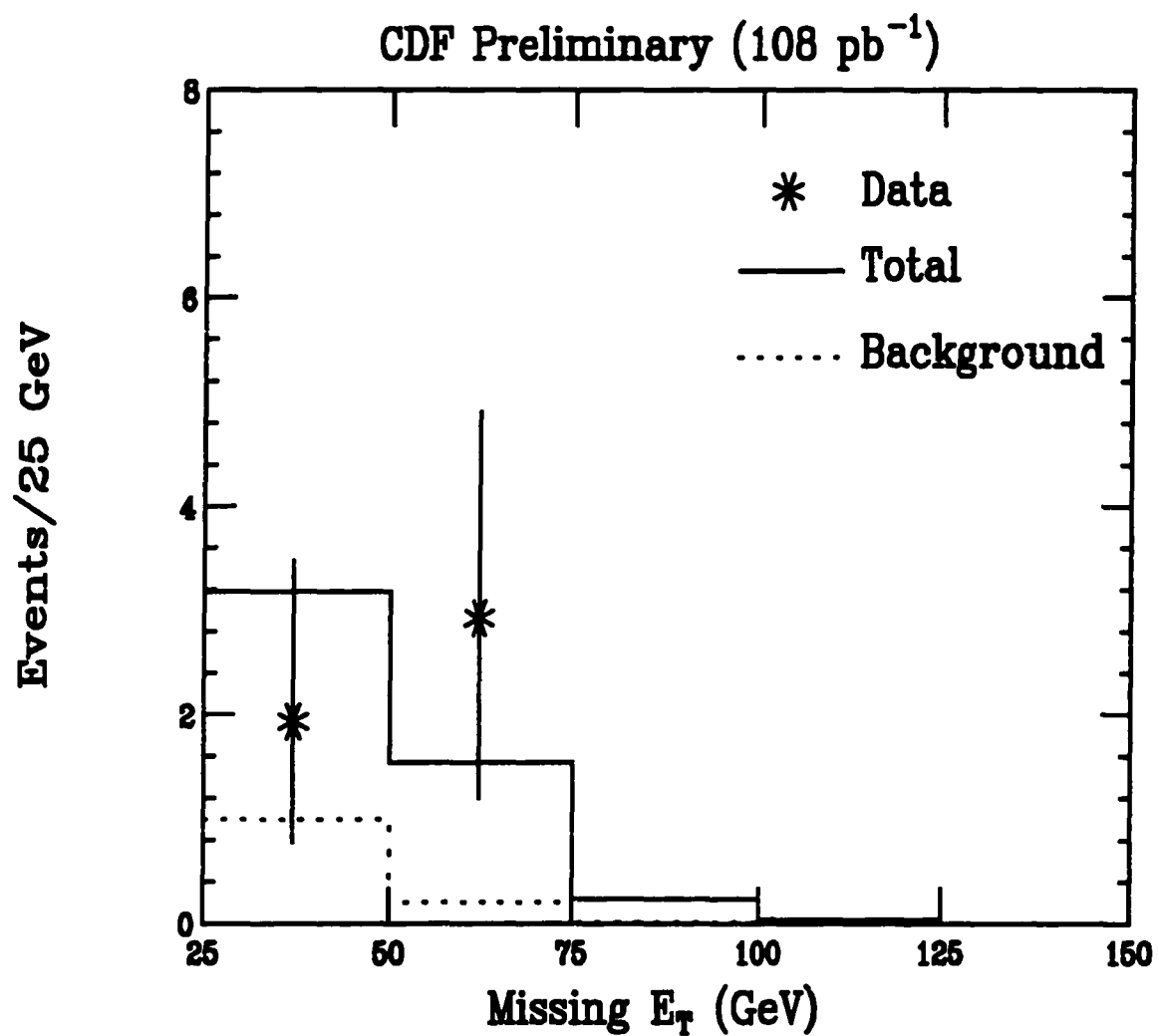


Figure 5.18: The \cancel{E}_T distribution for W^+W^- candidates. The dotted histogram is the background to W^+W^- . The total number of events (solid histogram) is normalized to the observed number of events.

area is 0.34. The systematic uncertainty takes account of all related factors from the background, detection efficiency, and integrated luminosity. The result is summarized in Figure 5.19. In this plot two theoretical results are presented: a leading order (LO) calculation from Refs. [2, 4], and a next-to-leading order (NLO) calculation from Ref. [5], as discussed in detail in Chapter 1. We conclude that the CDF measurement of $\sigma(\bar{p}p \rightarrow W^+W^-)$ is consistent with the standard model prediction.

5.2.2 Upper Limit

Let CL denote the confidence level, then $1 - \text{CL}$ can be expressed as [38, 39]

$$1 - \text{CL} = \frac{\sum \int \int G(y, N_B, N_B \chi_B) G(x, N, N \chi_S) f(n, x + y) dx dy}{\sum \int G(y, N_B, N_B \chi_B) f(n, y) dy}. \quad (5.3)$$

Here N_B is the background, and N is the upper limit for the number of observed events n_0 . The parameters χ_B and χ_S are the fractional uncertainties of background and signal, respectively. The sums are for n from 0 to n_0 . The function $f(n, x)$ is the Poisson distribution function with mean = x

$$f(n, x) = \frac{x^n}{n!} \exp(-x). \quad (5.4)$$

Here a Gaussian function $G(x, \mu, \sigma)$ is used to smear the mean of the Poisson distribution to simulate the effect of systematic uncertainties on the upper limit N . The uncertainties arising from the detection efficiency and luminosity are combined together as the signal uncertainty, assuming that they are uncorrelated.

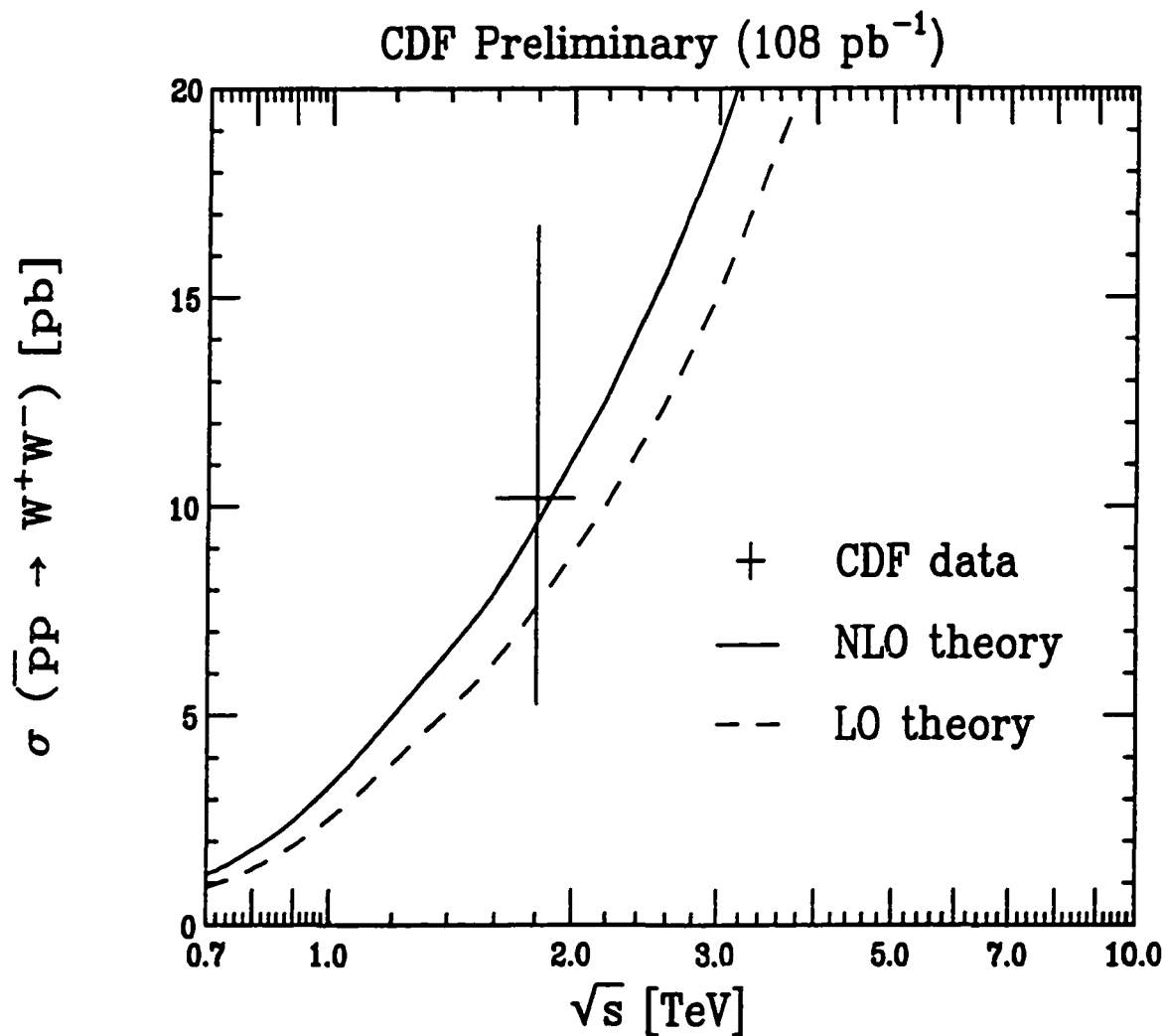


Figure 5.19: The W^+W^- production cross section $\sigma(\bar{p}p \rightarrow W^+W^-)$ measured at the CDF, compared to the theoretical results which are based on the next-to-leading order (NLO) (solid line) and leading order (LO) (dashed line) calculations. See text for detail.

The function is of the form

$$A(\mu, \sigma) \exp\left[-\frac{(x - \mu)^2}{2\sigma^2}\right],$$

where $A(\mu, \sigma)$ is the normalization factor.

Note that signal and background are correlated through the terms $(x + y)^n$ ($n = 0, 1, \dots, n_0$) in Eq. 5.3, which makes it very difficult to do the integration. However, for not very large n_0 , we can expand $(x + y)^n$ as

$$(x + y)^n = x^n + c_1 x^{n-1} y + \dots + y^n. \quad (5.5)$$

The coefficients c_i can be easily obtained for small n . Thus the two-fold integration in Eq. 5.3 is simplified to two uncorrelated integrations. The subroutine GAUS8 in the mathematics library SLATEC is used to calculate numerically these integrations.

At 95% CL, the background-subtracted upper limit is found to be 9.89 if five events are observed. This upper limit will be used later to determine limits on anomalous couplings. Upper limit on the continuum W^+W^- production cross section is given by (see Eq. 5.1)

$$\sigma^{\text{upperlimit}}(\bar{p}p \rightarrow W^+W^-) = 26.6 \text{ pb}$$

at 95 % CL.

5.3 WWV Anomalous Couplings

5.3.1 Parameters

For WWV anomalous couplings ($V = \gamma, Z$), the most general effective Lagrangian, if it is Lorentz, C, and P invariant, may be described in terms of six couplings denoted as g_1^V , κ_V , and λ_V , as discussed in Chapter 1. In the SM, $g_1^V=1$, $\kappa_V=1$, and $\lambda_V=0$. A dipole form factor of the form

$$\frac{1}{(1 + \hat{s}/\Lambda^2)^2}$$

is introduced, with the energy scale Λ .

In this analysis, a tree-level Monte Carlo generator[1] is used to generate W^+W^- events at the parton level and the output is fed to the fast detector simulation QFL. Then the fully simulated W^+W^- events are filtered through the selection procedure. Since there is no QCD correction in this generator and we are only interested in the relative derivation from the SM prediction, the expected number of W^+W^- events obtained from this generator is normalized to that from ISAJET. In this way, a possible bias from QCD effect is avoided.

5.3.2 Upper Limits

I will discuss briefly how upper limits on anomalous couplings are obtained in one scenario that assumes $\kappa_\gamma=\kappa_Z=\kappa$ and $\lambda_\gamma=\lambda_Z=\lambda$, with $\Delta\kappa=\kappa - 1$. The same procedure can be applied to other scenarios.

The expected number of events can be written as a quadratic function of anomalous couplings since helicity amplitudes are linear functions of these couplings. In this scenario, $\Delta\kappa$ and λ are independent parameters. Then the expected number of events N_{exp} can be expressed as

$$N_{exp}(\Delta\kappa, \lambda) = c_0[1 + c_1(\Delta\kappa) + c_2\lambda + c_3(\Delta\kappa)\lambda + c_4(\Delta\kappa)^2 + c_5\lambda^2]. \quad (5.6)$$

First, N_{exp} is obtained from simulations at $(\Delta\kappa, \lambda) = (0,0), (0,1), (1,0), (1,1), (0,-1), (-1,0), (-1,1), (1,-1),$ and $(-1,-1)$, a total of nine points. Then the subroutine MATIN1 from the CERN library is used to fit this equation and get the coefficients. Clearly, c_0 is the expected number of events in the standard model ($\Delta\kappa = \lambda = 0$), which is normalized to the standard model prediction obtained from ISAJET. Finally, upper limit for five events is used to find limits on $\Delta\kappa$ and λ .

Fitting results for different choices of the energy scale Λ are summarized in the following equations:

$$N_{exp} = 1.000 - 0.347(\Delta\kappa) - 0.089\lambda + 0.098(\Delta\kappa)\lambda + 1.328(\Delta\kappa)^2 + 2.300\lambda^2, \quad (5.7)$$

$$N_{exp} = 1.000 - 0.334(\Delta\kappa) - 0.116\lambda + 0.134(\Delta\kappa)\lambda + 2.034(\Delta\kappa)^2 + 3.659\lambda^2 \quad (5.8)$$

for $\Lambda = 1$ and 2 TeV, respectively. For simplicity, we normalize N_{exp} to 1 for couplings at their SM values. Table 5.3 lists limits on anomalous couplings at $\Delta\kappa = 0$ or $\lambda = 0$, with two different choices of the energy scale Λ . Contours of these limits are given in Figure 5.20, with $\Lambda = 1$ TeV (outer contour) and $\Lambda = 2$ TeV (inner contour).

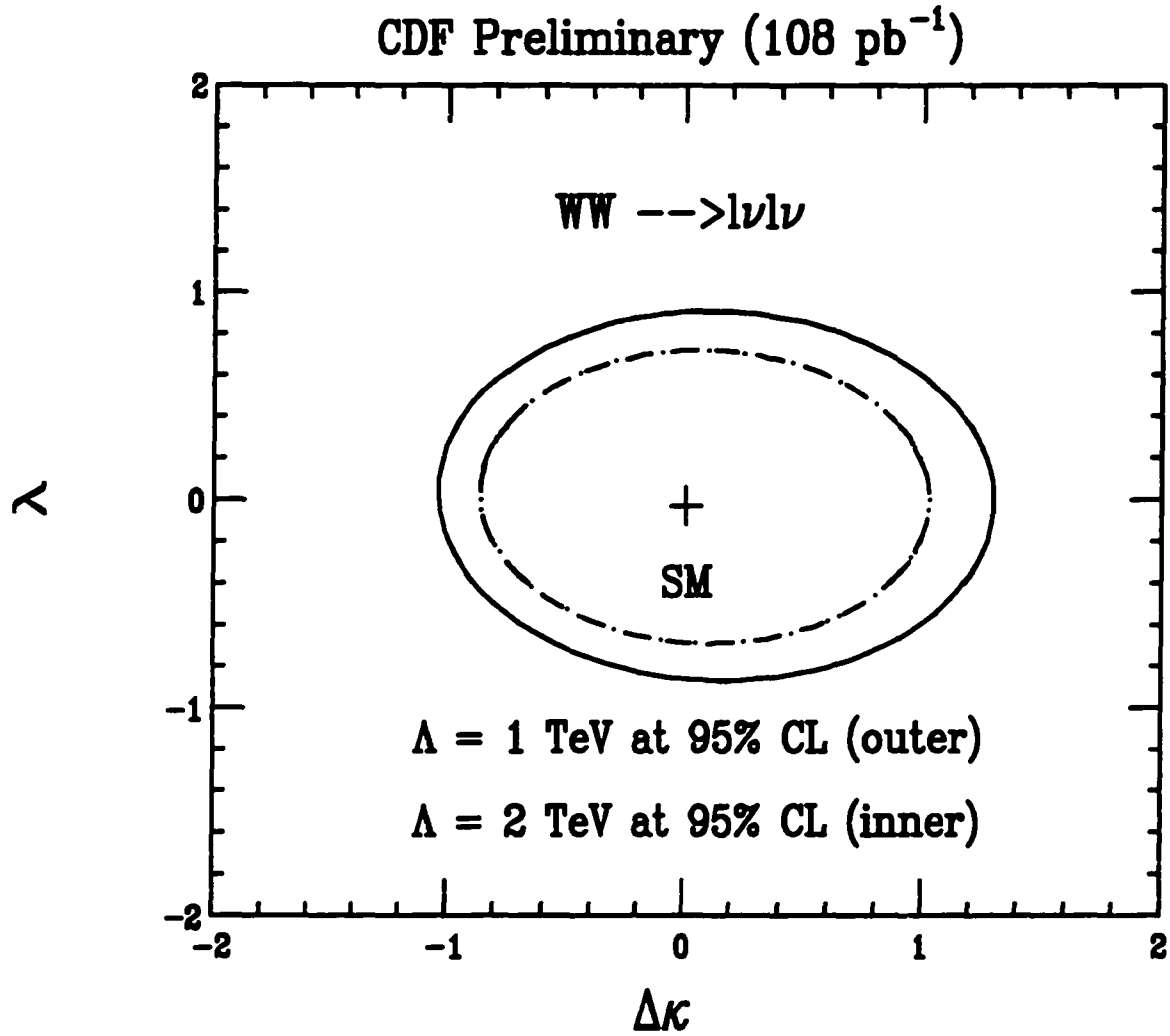


Figure 5.20: Upper limits on anomalous couplings $\Delta\kappa$ and λ , assuming $\kappa_\gamma = \kappa_Z = \kappa$ and $\lambda_\gamma = \lambda_Z = \lambda$. Here $\Delta\kappa = \kappa - 1$. The SM value is located at the center. The outer (inner) contour is 95 % CL upper limits with the energy scale $\Lambda = 1 \text{ TeV}$ (2 TeV).

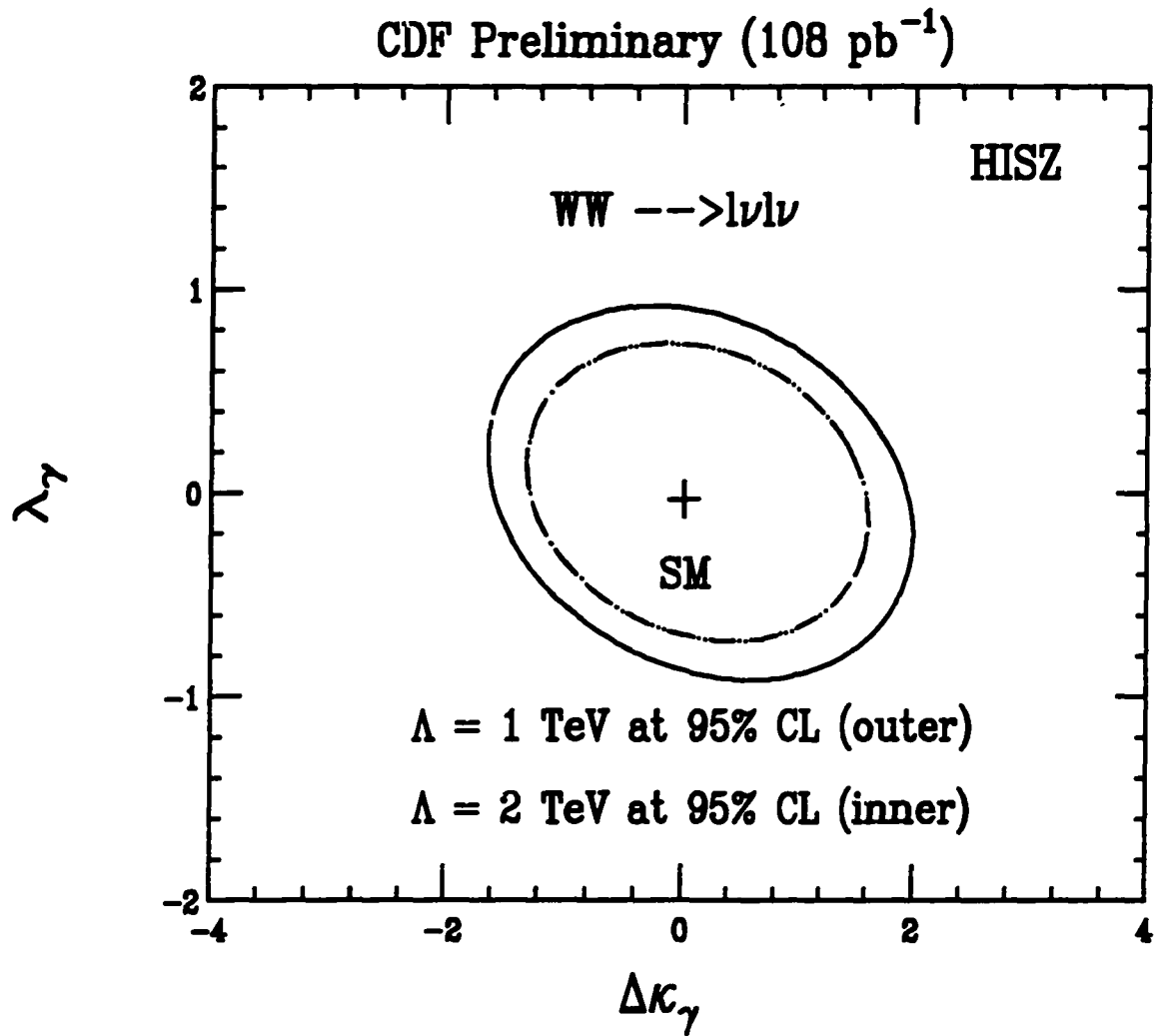


Figure 5.21: Upper limits on anomalous couplings $\Delta\kappa_\gamma$ and λ_γ in the HISZ scenario. The SM value is located at the center. The outer (inner) contour is 95 % CL upper limits with the energy scale $\Lambda = 1 \text{ TeV}$ (2 TeV).

$\Lambda=1$ TeV	$-1.02 < \Delta\kappa < 1.28$ ($\lambda=0$)
	$-0.85 < \lambda < 0.89$ ($\Delta\kappa=0$)
$\Lambda=2$ TeV	$-0.85 < \Delta\kappa < 1.01$ ($\lambda=0$)
	$-0.68 < \lambda < 0.71$ ($\Delta\kappa=0$)

Table 5.3: Upper limits on anomalous couplings at 95 % CL for two different energy scales. The vertices $WW\gamma$ and WWZ are assumed to have the same couplings constants.

Similar results are obtained in the HISZ scenario:

$$N_{exp} = 1.000 - 0.204(\Delta\kappa) - 0.088\lambda + 0.539(\Delta\kappa)\lambda + 0.586(\Delta\kappa)^2 + 2.287\lambda^2, \quad (5.9)$$

$$N_{exp} = 1.000 - 0.270(\Delta\kappa) - 0.123\lambda + 0.667(\Delta\kappa)\lambda + 0.881(\Delta\kappa)^2 + 3.496\lambda^2 \quad (5.10)$$

for $\Lambda = 1$ and 2 TeV, respectively. Figure 5.21 shows limits in this scenario, with $\Lambda = 1$ TeV (outer contour) and $\Lambda = 2$ TeV (inner contour).

5.3.3 Limits from other experiments

Limits from low energy precision measurements, briefly discussed in Chapter 1, are not presented here because data are not sufficient and ambiguities associated with these constraints are still unsolved. Here I will concentrate on results from the CDF and D0 experiments[40].

Diboson search through the channel $W\gamma \rightarrow l\nu\gamma$ has a better statistics due to the relatively larger production cross section [$\sigma B(W\gamma \rightarrow l\nu\gamma) \sim 20$ pb]. Lepton

selection cuts are similar to those used in this analysis. Photons, with $E_T^\gamma > 7$ (10) GeV at the CDF (D0), are required to be well isolated from leptons. 109 (23) $W\gamma$ candidates are observed at the CDF (D0)[40]. A log-likelihood fit of the background-corrected E_T^γ spectra sets upper limits on anomalous couplings at 95 % CL:

$$-1.8 < \Delta\kappa < 2.0 \text{ (CDF),}$$

$$-1.6 < \Delta\kappa < 1.8 \text{ (D0),}$$

$$-0.7 < \lambda < 0.6 \text{ (CDF),}$$

$$-0.6 < \lambda < 0.6 \text{ (D0),}$$

with the energy scale $\Lambda = 1.5$ TeV. Notice that $W\gamma$ search is insensitive to κ even though the number of observed $W\gamma$ events is relatively large. This will be discussed later in this section.

Diboson production through the channel $WW \rightarrow l\nu + jets$ provides another opportunity to probe boson couplings[40]. Large QCD background is suppressed by a high P_T^{jj} ($P_T^{e\nu}$) cut at the CDF (D0). Both CDF and D0 observed one candidate. Fitting the log-likelihood yields

$$-0.9 < \Delta\kappa < 1.0 \text{ (CDF),}$$

$$-0.9 < \Delta\kappa < 1.1 \text{ (D0),}$$

$$-0.6 < \lambda < 0.7 \text{ (CDF),}$$

$$-0.7 < \lambda < 0.7 \text{ (D0),}$$

with the energy scale $\Lambda = 1.5$ TeV. Since there are only few candidates, limits in this channel are very sensitive to the thresholds of P_T^{jj} and $P_T^{e\nu}$.

All these results are summarized in Figure 5.22. Compared with those obtained in other channels, limits from this analysis are very competitive. The sensitivity to κ is better in W^+W^- production than in $W\gamma$ and $Z\gamma$ productions due to the different behavior of amplitudes associated with $\Delta\kappa$ and λ [41, 42]. While λ terms in helicity amplitudes always grow with \hat{s}/M_W^2 in W^+W^- , $W\gamma$, and $Z\gamma$ productions, κ terms are quite different. In W^+W^- production, κ terms increase with \hat{s}/M_W^2 . On the other hand, κ terms increase with $\sqrt{\hat{s}}/M_W$ in $W\gamma$ and $Z\gamma$ productions. Note that $\sqrt{\hat{s}} \sim 2M_W$ in W^+W^- production and $\sqrt{\hat{s}} \sim M_W$ in $W\gamma$ and $Z\gamma$ productions. So \hat{s}/M_W^2 enhances the sensitivity to κ in W^+W^- production.

Certainly, higher luminosity will result in tighter limits on anomalous couplings. Recall that the expected number of W^+W^- events, which is proportional to integrated luminosity, can be expressed as a quadratic function of anomalous couplings. So limits on anomalous couplings scale like $(\int \mathcal{L} dt)^{-1/2}$. In addition, a better understanding of systematic uncertainties and backgrounds will also enable us to enhance the sensitivity to anomalous couplings. This can be achieved by running more reliable W^+W^- Monte Carlo programs and finding new ways to reduce the Drell-Yan and fake backgrounds. Finally, better limits could be obtained if one uses a log-likelihood fit of E_T and \cancel{E}_T spectra, which are found more sensitive to anomalous couplings than the number of events[42].

In Table 5.4, future limits on anomalous couplings are presented for various experiments around the world. For a comprehensive review on anomalous couplings, see Refs. [40, 43].

5.4 Summary

The selection criteria for $W^+W^- \rightarrow l^+l^-\nu\bar{\nu}$ candidates are quite clear: two high P_T leptons, large missing E_T , and little jet activity. However, W^+W^- search is complicated by the detector effects and theoretical uncertainties. To discriminate against a wide variety of backgrounds, a few special cuts have been applied.

Leptons from W semileptonic decays are centered at the Jacobian peak (~ 40 GeV) in the E_T spectrum. So $E_T > 20$ GeV is required for leptons from W^+W^- production. Similarly, the two neutrinos from $W^+W^- \rightarrow l^+l^-\nu\bar{\nu}$ should give a large missing transverse energy \cancel{E}_T . A minimum of 25 GeV is required for \cancel{E}_T , which also serves to reduce those backgrounds with no or very low \cancel{E}_T , such as the Drell-Yan process. Leptons and neutrinos from the background $Z \rightarrow \tau\tau$ are most likely to be back-to-back. As a result, an azimuthal angle cut is applied to ensure that leptons are not very close to the direction of \cancel{E}_T . The top background $t\bar{t} \rightarrow W^+W^-b\bar{b}$, with two high E_T jets from b quarks, is greatly reduced by removing events with jet activity, although the uncertainty arising from this cut is relatively large.

After all these selection cuts, the SM predicts 3.53 ± 1.24 W^+W^- events where

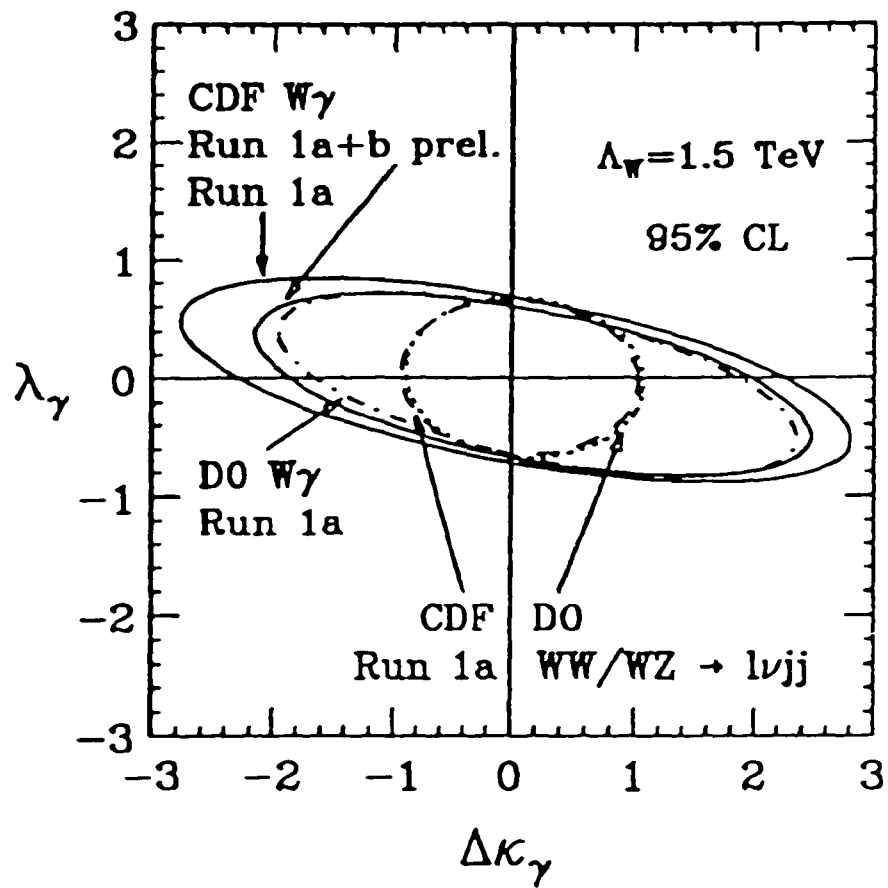


Figure 5.22: Present upper limits on anomalous couplings from $W\gamma$ and $WW/WZ \rightarrow l\nu jj$ productions.

Experiment	$\int \mathcal{L} dt$	Channel	Upper Limit
CDF	1 fb^{-1}	$W^+W^- \rightarrow l^+l^-\nu\bar{\nu}$	$-0.45 < \Delta\kappa_\gamma < 0.75$ $-0.27 < \lambda_\gamma < 0.31$
CDF	1 fb^{-1}	$W^+W^- \rightarrow l\nu jj$	$-0.31 < \Delta\kappa_\gamma < 0.41$ $-0.19 < \lambda_\gamma < 0.19$
CDF	1 fb^{-1}	$W\gamma \rightarrow l\nu\gamma$	$-0.38 < \Delta\kappa_\gamma < 0.38$ $-0.12 < \lambda_\gamma < 0.12$
LEP II	500 pb^{-1}	$W^+W^- \rightarrow l\nu jj$	$-0.16 < \Delta\kappa_\gamma < 0.18$ $-0.15 < \lambda_\gamma < 0.16$
NLC	80 fb^{-1}	$W^+W^- \rightarrow l\nu jj$	$-0.002 < \Delta\kappa_\gamma < 0.002$ $-0.002 < \lambda_\gamma < 0.002$
LHC	100 fb^{-1}	$W\gamma \rightarrow l\nu\gamma$	$-0.08 < \Delta\kappa_\gamma < 0.08$ $-0.006 < \lambda_\gamma < 0.006$

Table 5.4: Projected 95 % CL upper limits on anomalous WWV ($V = \gamma, Z$) couplings in the HISZ scenario. Only one of the independent couplings is assumed to deviate from the SM at a time.

both W bosons decay into leptons and neutrinos. Five events are observed at the CDF with 1.21 ± 0.30 events expected from the background. The W^+W^- production cross section $\sigma(\bar{p}p \rightarrow W^+W^-)$ has been measured for the first time. Experimental measurements of W^+W^- production are consistent with the standard model prediction.

From the observed yield, we set upper limits on $WW\gamma$ and WWZ anomalous couplings at 95 % confidence level. To find these upper limits, the number of expected W^+W^- events (N_{exp}) is derived as a function of anomalous couplings from Monte Carlo simulations. Then bounds on anomalous couplings are obtained by setting N_{exp} to the value of the Poisson upper limit for five observed events. Limits on anomalous couplings from this analysis are of the order of 1, slightly better than those from other channels.

In the future, an integrated luminosity of 1 fb^{-1} is anticipated by the CDF. Also the ongoing CDF upgrade project will greatly increase the W^+W^- acceptance by extending the dilepton search beyond the central region. The improvement will permit further stringent limits on $WW\gamma$ and WWZ anomalous couplings, and reduce the statistical uncertainty of the W^+W^- production cross section. This will lead to a better understanding of trilinear vector boson couplings—an important, yet still poorly tested sector of the standard model.

Appendix A

Anomalous Couplings

In the framework of the $SU(2) \times SU(1)$ gauge symmetry, there are two ways for a phenomenological model to introduce boson self-interactions: linear realization and nonlinear realization[40]. The latter is out of the scope of this analysis, so I will concentrate on the linear realization.

To develop an effective electroweak Lagrangian, a set of expanded interaction operators \mathcal{O}_i , together with a Higgs double field Φ , are introduced to induce effective interactions

$$\mathcal{L} = \mathcal{L}_{SM} + \frac{1}{\Lambda^2} \sum_i \alpha_i \mathcal{O}_i + \dots \quad (\text{A.1})$$

The operators \mathcal{O}_i are determined by the $SU(2) \times SU(1)$ gauge symmetry. All higher-order terms are suppressed by Λ —the energy scale beyond which the theory is not valid anymore. Therefore, the renormalizability of the theory is not required since this theory is no longer expected to be valid at high energy. The

interaction Lagrangian relevant to boson couplings is given by

$$\begin{aligned} \mathcal{L} = & \frac{f_B}{\Lambda^2} [(D_\mu \Phi)^\dagger \hat{B}^{\mu\nu} (D_\nu \Phi)] + \frac{f_W}{\Lambda^2} [(D_\mu \Phi)^\dagger \hat{W}^{\mu\nu} (D_\nu \Phi)] \\ & + \frac{f_{WWW}}{\Lambda^2} \text{Tr} [\hat{W}_{\mu\nu} \hat{W}^{\nu\lambda} \hat{W}_\lambda^\mu]. \end{aligned} \quad (\text{A.2})$$

Here W and B are the SU(2) and SU(1) gauge fields, respectively. Expanding these terms and comparing them with the effective Lagrangian lead to the following constraints:

$$\Delta\kappa_\gamma = (f_B + f_W) \frac{m_W^2}{2\Lambda^2}, \quad (\text{A.3})$$

$$\Delta\kappa_Z = (f_W - s^2(f_B + f_W)) \frac{m_Z^2}{2\Lambda^2}, \quad (\text{A.4})$$

$$\Delta g_1^Z = f_W \frac{m_W^2}{2\Lambda^2} = \Delta\kappa_Z + \frac{s^2}{c^2} \Delta\kappa_\gamma, \quad (\text{A.5})$$

$$\lambda_\gamma = \lambda_Z = \lambda = \frac{3m_W^2 g^2}{2\Lambda^2} f_{WWW}. \quad (\text{A.6})$$

Here $s = \sin \theta_W$, $c = \cos \theta_W$, and others are free parameters. All anomalous couplings are suppressed by a factor of $\frac{m_W^2}{\Lambda^2}$ and hence they vanish at high energy.

When discussing experimental results, for simplicity, one usually chooses two parameters as independent and the remaining ones are set to their standard model values. If $f_W = f_B$, these equations are reduced to

$$\Delta g_1^Z = \frac{1}{2\cos^2 \theta_W} \Delta\kappa_\gamma, \quad (\text{A.7})$$

$$\Delta\kappa_Z = \frac{1}{2}(1 - \tan^2 \theta_W) \Delta\kappa_\gamma, \quad (\text{A.8})$$

$$\lambda_Z = \lambda_\gamma. \quad (\text{A.9})$$

These relations lead to the familiar HISZ scenario, as discussed in Chapter 1. The other frequently used scenario is to choose $\Delta\kappa$ and λ as independent parameters, with $\Delta\kappa = \Delta\kappa_\gamma = \Delta\kappa_Z$, $\lambda = \lambda_\gamma = \lambda_Z$, and $\Delta g_1^Z = \Delta g_1^\gamma = 0$.

Appendix B

Measurement of Magnetic Field

A fixed area loop is used to measure the field integral $\int B dz$, an essential quantity for the momentum measurement. This loop is constructed by glueing two parallel 0.002 inch diameter steel wires 10 ± 0.1 cm apart on a $150 \text{ cm} \times 12 \text{ cm} \times 2 \text{ mm}$ in piece of G10. The loop is inserted into the gap at the top of each toroid to measure the field flux, or the field integral since the width of the loop is fixed. An integrator is attached to the loop as shown in Figure B.1. Its output is directly related to the field integral. After complete insertion, the voltage output is

$$V_{out} = \frac{L}{RC} \int B dz \quad (\text{B.1})$$

where $L = 10 \pm 0.1$ cm is the width of the loop. The integrator consists of a trimmed resistor of one megaohm and a capacitor of one microfarad. The resistor R and capacitor C are measured by using a DVM and a bridge circuit, with $R = 1.0037 \pm 0.0002 \text{ M}\Omega$ and $C = 0.982 \pm 0.002 \mu\text{F}$. The ratio of the integrator output

to the field flux is $1/RC = 1.015 \pm 0.002 \text{ sec}^{-1}$.

To measure the strength of the magnetic field, a piece of doped semiconductor is used as probe. Its output is proportional to the product of the control current and field strength, which is known as the Hall effect. The control current is set to be 15 mA. The proportional constant, also called product sensitivity, is given in the manufacturer's data sheet as 0.25 V/A.kG. The output voltage is connected to an amplifier circuit to get a larger readout. The operational amplifier is a simple feedback circuit as shown in Figure B.2.

The loop and probe are calibrated with a dipole magnet in the Magnet Test Facility at Fermilab. The field strength B is measured by using a pre-calibrated NMR probe. The field flux is changed by moving the loop along the dipole magnet, causing a change of the integrator output. The ratio of this output to the field flux is 1.010 ($B = 1.54 \text{ T}$) and 1.012 ($B = 0.986 \text{ T}$), respectively. They agree well with the theoretical value 1.015, as mentioned earlier. The proportional constant of the probe is found to be $1.031 \pm 0.002 \text{ (V/T)}$ for B from 1.6 T to 1.9 T. It is determined by several factors : the gain of the amplifier in the circuit (25.0); the control current (15 mA); and the product sensitivity of the Hall element (0.25 V/A.kG).

The loop measurement for 1,000 Amps current is compared with previous results[44] in Figure B.3. Good agreement is observed. The theoretical curve at the radius R (cm)

$$B(T) = 2.779 - 0.1845 \ln R \quad (\text{B.2})$$

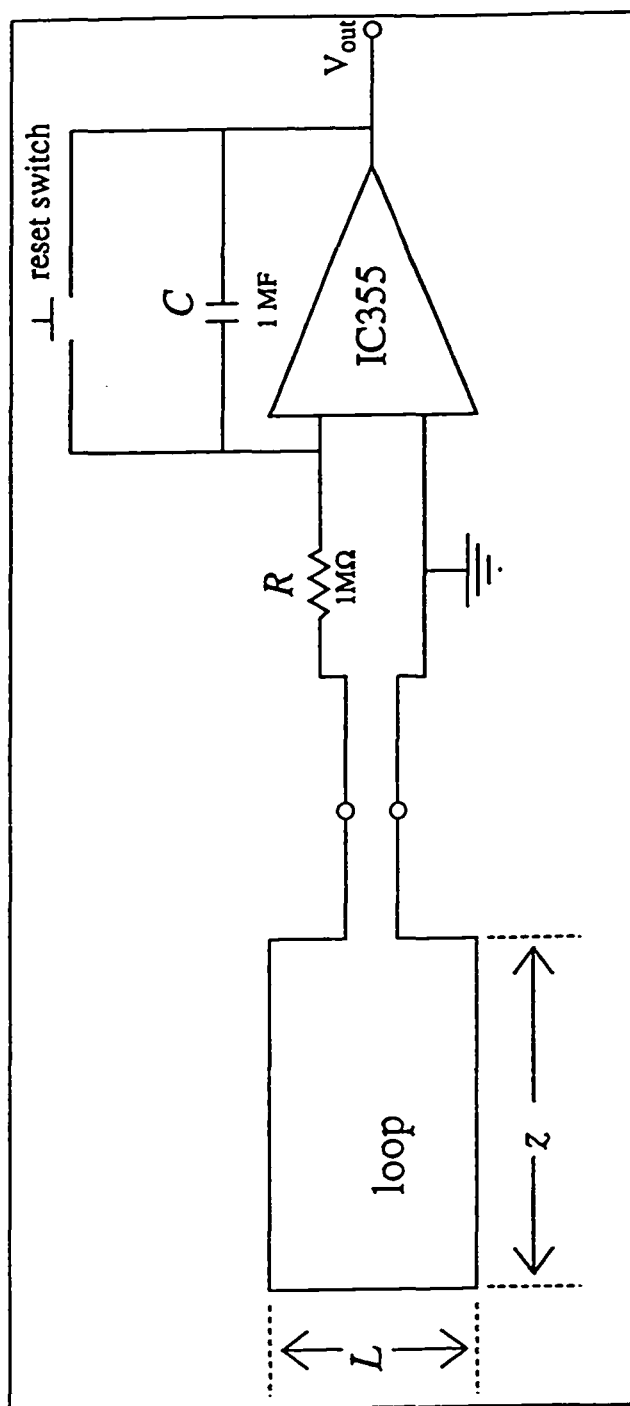


Figure B.1: Loop and integrator circuit. The loop is constructed from steel wires. Electric charges eventually reach the capacitor where they accumulate.

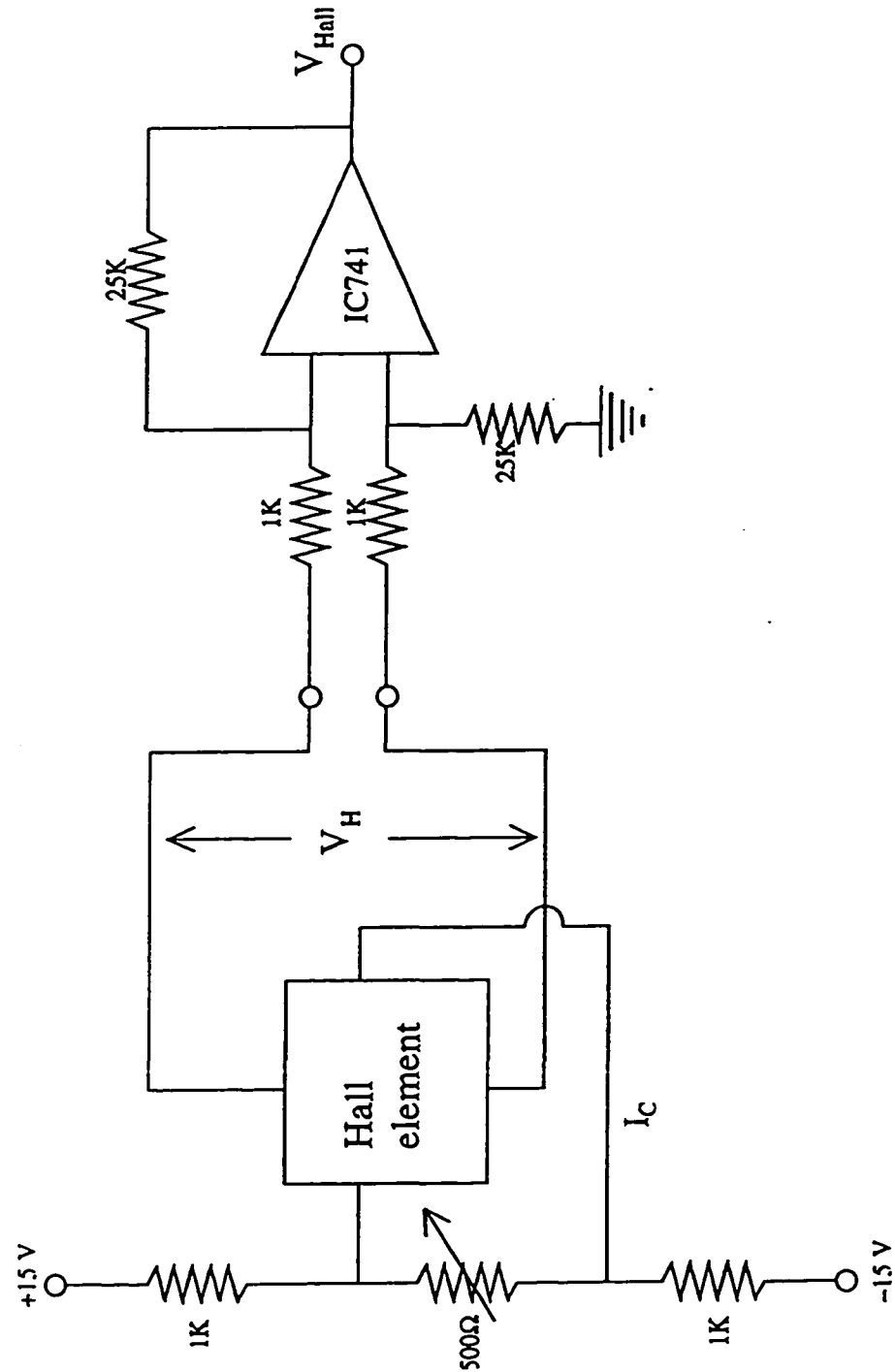


Figure B.2: Hall probe and feedback amplifier circuit. The output of the Hall element is determined by the control current I_C and the strength of magnetic field. The gain of the circuit is determined by the ratio of resistors.

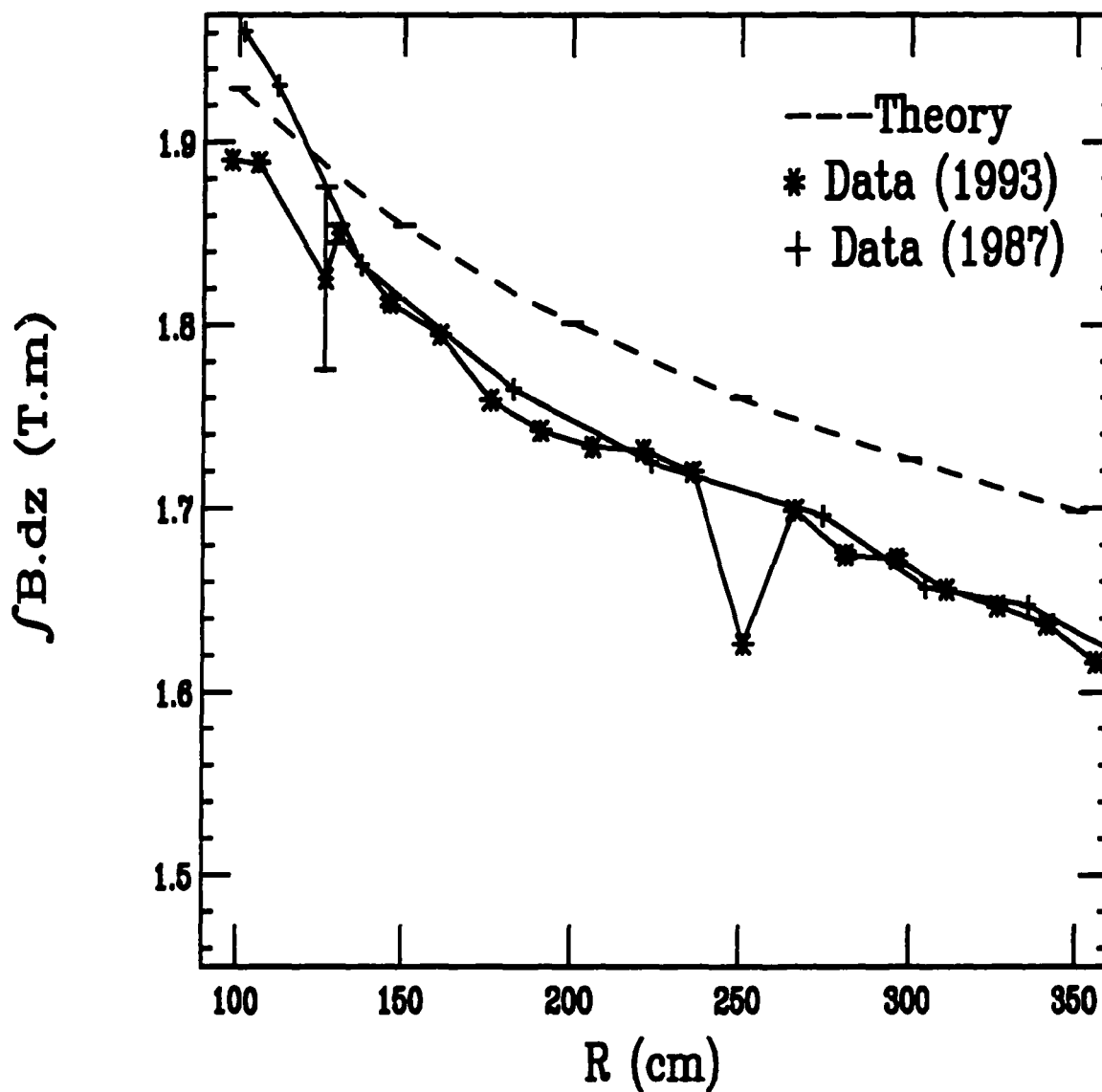


Figure B.3: Magnetic field integral for the east rear toroid with a current of 1,000 Amps. R is the distance from the beampipe in r - ϕ . The two dips are caused by the non-uniform field near seams.

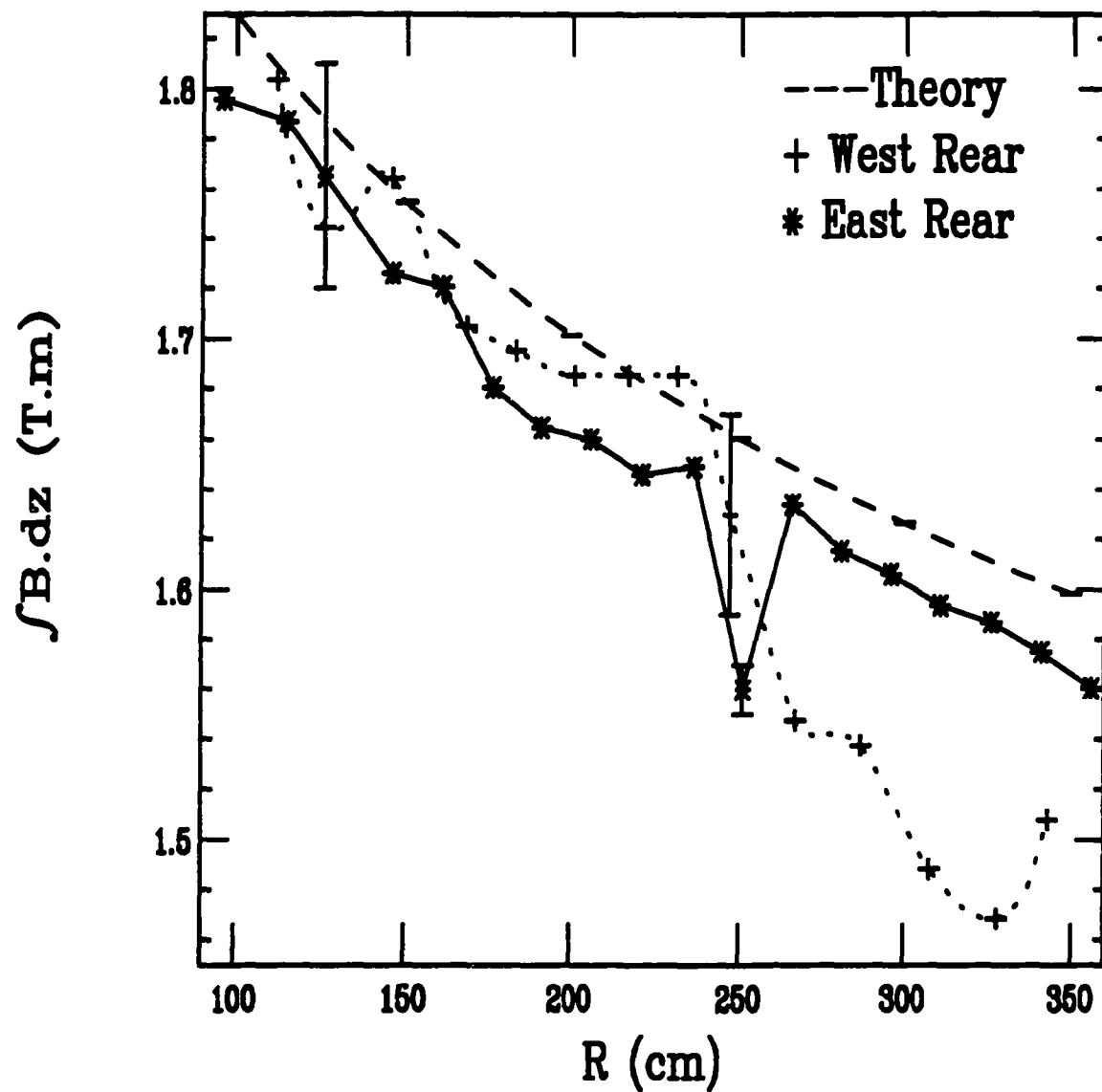


Figure B.4: Magnetic field integral for the east and west rear toroids with a current of 600 Amps.

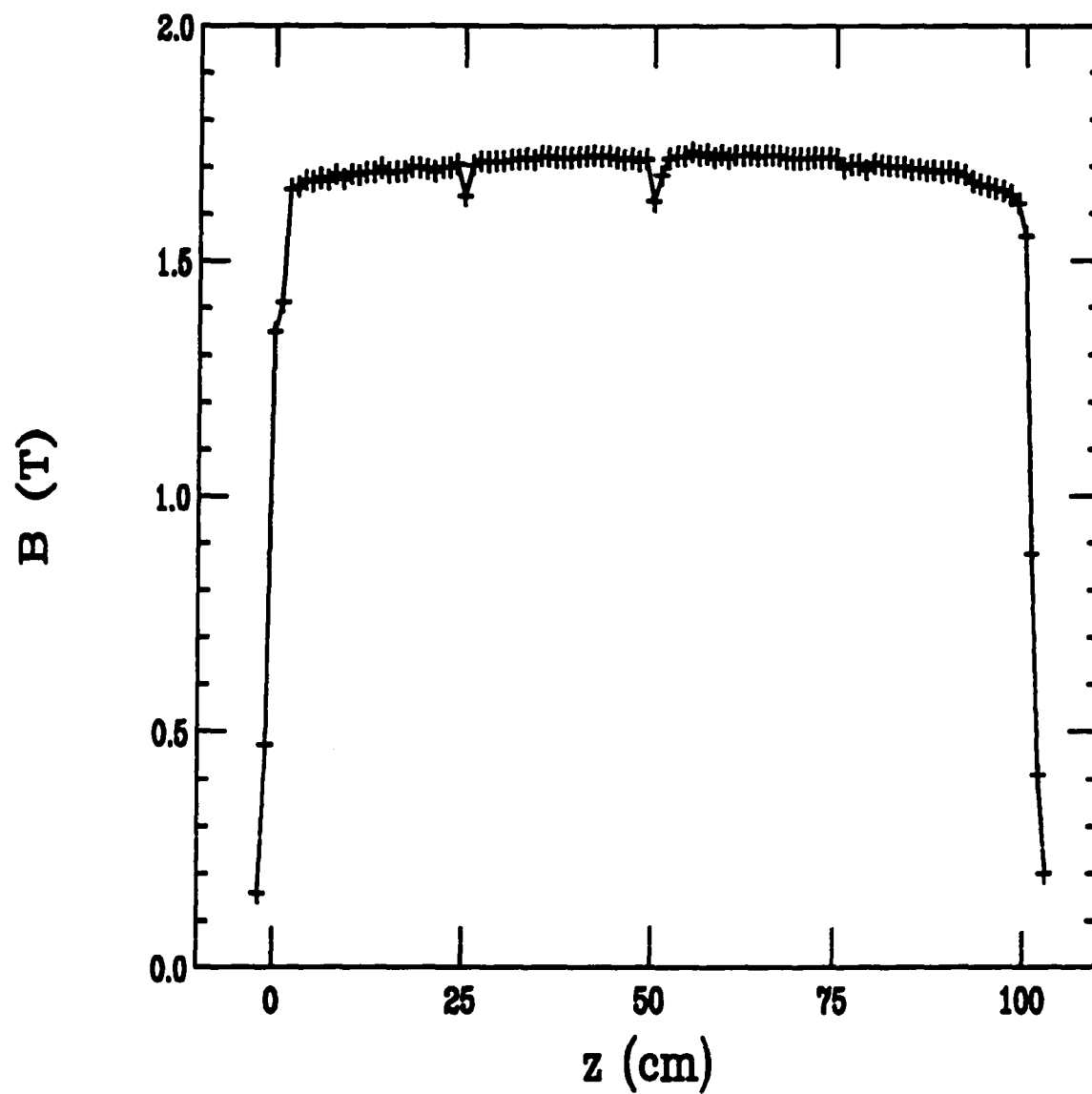


Figure B.5: West rear field profile along the z direction at a fixed distance (214 cm) from the beampipe, with a current of 600 Amps. The toroid starts at $z = 0.0$ cm and ends at $z = 100.0$ cm.

is based on the magnetization curve for SAE 1010 steel of one meter thick. The dips near $R = 125$ cm and $R = 250$ cm are caused by the nonuniform field at seams in the iron stack. The loop measurements at 600 Amps for both east and west rear toroids are given in Figure B.4. The theoretical curve

$$B(T) = 2.679 - 0.1845 \ln R \quad (\text{B.3})$$

is subtracted 0.1 T uniformly from the curve for 1,000 Amps excitation. Figure B.5 shows the field profile vs depth at a fixed radius of 214 cm for the west rear toroid, as obtained with the Hall probe. Note that the toroid is from 0.0 cm to 100.0 cm in the z direction. The field falls very quickly once outside the toroid.

Bibliography

- [1] K. Hagiwara, J. Woodside, and D. Zeppenfeld, *Phys. Rev. D* **41**, 2113 (1990).
- [2] V. Barger and R. Phillips, *Collider Physics* (Addison-Wesley, New York, 1987).
- [3] E. Eichten, I. Hinchliffe, K. Lane, and C. Quigg, *Rev. Mod. Phys.* **56**, 579 (1984); **58**, 1065(E) (1986).
- [4] V. Barger, T. Han, D. Zeppenfeld, and J. Ohnemus, *Phys. Rev. D* **41**, 2782 (1990), and references therein.
- [5] J. Ohnemus, *Phys. Rev. D* **44**, 1403 (1991).
- [6] P. Harriman, A. Martin, R. Roberts, and W. Stirling, *Phys. Rev. D* **42**, 798 (1990).
- [7] W. Alles, Ch. Boyer, and A. Buras, *Nucl. Phys. B* **119**, 125 (1977).
- [8] K. Hagiwara, S. Ishihara, R. Szalapski, and D. Zeppenfeld, *Phys. Rev. D* **48**, 2182 (1993).

- [9] S. Playfer, Proceedings of the "International Symposium on Vector Boson Self-Interactions", February 1995, Los Angeles, AIP Conference Proceedings 350, p124-135.
- [10] CDF Collaboration, F. Abe *et al.*, Nucl. Instrum. Methods A 271, 387 (1988).
- [11] J. Skarha, Ph.D. thesis, University of Wisconsin, 1989.
- [12] J. Lamoureux, Ph.D. thesis, University of Wisconsin, 1995.
- [13] CDF Dilepton group (CDF-2862-unpublished).
- [14] CDF Dilepton group (CDF-2851-unpublished).
- [15] P. de Barbaro *et al.* (CDF-2910-unpublished).
- [16] CDF FMU group (CDF-3410-unpublished).
- [17] CDF Collaboration, F. Abe *et al.*, Phys. Rev. D 45, 1448 (1992).
- [18] M. Shapiro, private communication.
- [19] T. Hessing (CDF-1247-unpublished).
- [20] S. Kim and S. Vejcik (CDF-3006-unpublished).
- [21] CDF Collaboration, F. Abe *et al.*, Phys. Rev. D 50, 2966 (1994), and references therein.

- [22] S. Behrends and A. Garfinkel (CDF-1650-unpublished).
- [23] F. Paige and S.D. Protopopescu, BNL Report No. 38034, 1986 (unpublished).
- [24] H. Bengtsson and T. Sjostrand, CERN-TH.6488/92.
- [25] Tao Han, private communication. This Monte Carlo is based on a matrix element calculation, and generates $WW + 0$ jet, $WW + 1$ jet, and $WW + 2$ jets.
- [26] S. Kopp (CDF-2391-unpublished).
- [27] J. Proudfoot (CDF-3060-unpublished).
- [28] W. Badgett (CDF-2217-unpublished).
- [29] T. LeCompte et al. (CDF-2367-unpublished).
- [30] D. Glenzinski and P. Schalbach (CDF-2954-unpublished).
- [31] M. Dickson (CDF-2174-unpublished).
- [32] A. Spadafora (CDF-3232-unpublished).
- [33] D. Cronin-Hennessy et al. (CDF-3050-unpublished).
- [34] F. A. Berends, W. T. Giele, H. Kuijf, and B. Tausk, Nucl. Phys. **B357**, 32 (1991).

- [35] A. Martin, T. Liss, and R. Roser (CDF-3117-unpublished).
- [36] J. Ohnemus, *Phys. Rev. D* **44**, 3477 (1991).
- [37] L. Song, G.P. Yeh, and Q.F. Wang (CDF-2106-unpublished).
- [38] Review of Particle Properties, *Phys. Rev. D* **45**, (1992).
- [39] CDF Dilepton Group (CDF-1975-unpublished).
- [40] S. Errede, FERMILAB-Conf-94/306-E (preprint, 1994), to appear in the
“Proceedings of the 27th International Conference of High Energy Physics”,
Glasgow, Scotland, July 1994.
- [41] U. Baur, private communication.
- [42] U. Baur, T. Han, and J. Ohnemus, UB-HET-95-03, UCD-95-21, July 1995.
To be published in *Phys. Rev. D*.
- [43] H. Aihara et al., FERMILAB-Pub-95/031 (preprint, 1995), to appear in
“Electroweak Symmetry Breaking and Beyond the Standard Model”, eds.
T. Barklow, S. Dawson, H. Haber, and J. Siegrist.
- [44] D. Carlsmith et al. (CDF-528-unpublished).